

Horizon 2020



Reduced Order Modelling, Simulation and Optimization of Coupled systems

Reports about 8 selected benchmark cases of model hierarchies

Deliverable number: D5.1

Version 0.1



Funded by the European Union's Horizon 2020 research and innovation programme under the Marie Skłodowska-Curie Grant Agreement No. 765374

Project Acronym: ROMSOC
Project Full Title: Reduced Order Modelling, Simulation and Optimization of Coupled systems
Call: H2020-MSCA-ITN-2017
Topic: Innovative Training Network
Type of Action: European Industrial Doctorates
Grant Number: 765374

Editors:	Andrés Prieto, Peregrina Quintela, ITMATI
Deliverable nature:	Report (R)
Dissemination level:	Public (PU)
Contractual Delivery Date:	01/08/2018
Actual Delivery Date	30/09/2018
Number of pages:	91
Keywords:	Benchmarks, Model hierarchies
Authors:	Naomi Auer, WIAS Berlin Patricia Barral, ITMATI-USC Jean-David Benamou, INRIA Daniel Fernández Comesaña, Microflow Technologies Michele Girfoglio, SISSA Lena Hauberg-Lotte, U-HB Michael Hintermüller, WIAS Berlin Wilbert Ijzerman, Philips Karl Knall, MathTec Peter Maass, U-HB Gianfranco Marconi, Danieli Marco Martinolli, MOX, PoliMi Pier Paolo Monticone, CorWave SA Umberto Morelli, ITMATI Ashwin Nayak, ITMATI Luc Polverelli, CorWave SA Andrés Prieto, ITMATI-UDC Peregrina Quintela, ITMATI-USC Ronny Ramlau, Industrial Mathematics Institute JKU Conte Riccardo, Danieli Gianluigi Rozza, SISSA Giorgi Rukhaia, INRIA Nirav Shah, SISSA Bernadett Stadler, Industrial Mathematics Institute JKU Christian Vergara, MOX, PoliMi
Peer review:	Andrés Prieto, ITMATI-UDC Peregrina Quintela, ITMATI-USC

Abstract

Based on the multitude of industrial applications, benchmarks for model hierarchies will be created that will form a basis for the interdisciplinary research and for the training programme. These will be equipped with publically available data and will be used for training in modelling, model testing, reduced order modelling, error estimation, efficiency optimization in algorithmic approaches, and testing of the generated MSO/MOR software. The present document includes the description about the selection of (at least) eight benchmark cases of model hierarchies.

Disclaimer & acknowledgment

This project has received funding from the European Union's Horizon 2020 research and innovation programme under the Marie Skłodowska-Curie Grant Agreement No. 765374.

This document reflects the views of the author(s) and does not necessarily reflect the views or policy of the European Commission. The REA cannot be held responsible for any use that may be made of the information this document contains.

Reproduction and translation for non-commercial purposes are authorised, provided the source is acknowledged and the publisher is given prior notice and sent a copy.

Contents

I	Benchmark for high-performance algorithms in adaptive optics control	1
1.1	Introduction	1
1.1.1	Industrial Partner	1
1.2	Physical Description of the Problem - Astronomical Adaptive Optics	1
1.2.1	Basics of Imaging	2
1.2.2	AO Components	2
1.2.3	AO Systems	4
1.2.4	Statistics of the Atmosphere	5
1.3	Mathematical Description of the Problem	6
1.3.1	Wavefront Reconstruction	6
1.3.2	Atmospheric Tomography	9
1.4	Quality Evaluation	12
1.4.1	Strehl Ratio	12
1.4.2	Full Width at Half Maximum	13
1.5	Description of Data	13
II	Benchmark cases in development of coupled models for a sound intensity probe	14
2.1	Introduction	14
2.2	Model development	15
2.3	Benchmark Cases	16
2.4	Case 1: Fluid at rest	18
2.4.1	Computational Model	18
2.4.2	Code implementation	21
2.4.3	Results	23
2.5	Conclusion	24
III	Benchmark cases in optimal transportation	25
3.1	Context	25
3.2	Mathematical Model	25
3.2.1	PDE Model	25
3.2.2	OT Model	26
3.2.3	Geometrical Model	27
3.3	Numerical Models	27
3.3.1	Kantorovich's Linear Program	27

3.3.2	Monge-Ampère Based methods	28
3.3.3	Entropic regularization	28
3.4	Numerical algorithm and Benchmark Case	29
3.4.1	Sinkhorn algorithm	29
3.4.2	First Benchmark Case	29
3.4.3	Second Benchmark Case	30
IV	Data driven model adaptations of coil sensitivities in magnetic particle imaging	32
4.1	Introduction and literature	32
4.1.1	Magnetic Particle Imaging	32
4.1.2	Deep Learning and Inverse Problems	32
4.2	Mathematical description	33
4.2.1	Magnetic Particle Imaging	33
4.2.2	Deep Learning and Inverse Problems	37
4.2.3	Applying Deep Learning to Magnetic Particle Imaging	40
4.3	Data sets	40
4.3.1	1D Cartesian Sequence	42
4.3.2	2D Lissajous Sequence	42
V	Benchmarks for the Modelling of Continuous Casting Molds	43
5.1	Introduction and Motivation	43
5.2	State of the art	44
5.2.1	Direct problem	44
5.2.2	Inverse problem	47
5.3	Benchmarks	47
5.3.1	Benchmark 1	48
5.3.2	Benchmark 2	49
5.3.3	Benchmark 3	49
5.3.4	Benchmark 4	50
5.3.5	Benchmark 5	51
5.3.6	Benchmark 6	51
5.3.7	Benchmark 7	52
5.3.8	Benchmark 8	53
VI	Benchmark case of model hierarchies: Experimental-based Validation of FSI Simulations in Blood Pumps	56
6.1	Introduction	56
6.1.1	Introduction to Blood Pumps	56
6.1.2	The Progressive Wave Pump developed in CorWave SA	57

6.2 Literature and Modern Techniques	58
6.2.1 State-of-the-art in Blood Pumps	58
6.2.2 Computational Simulations as Support for LVAD Development	61
6.3 Mathematical Modeling of the FSI problem	61
6.3.1 The Computational Domain	61
6.3.2 Formulation of the FSI Problem	63
6.4 Benchmark Plan	64
6.4.1 Description of Real Data	64
6.4.2 Validation of the FSI Model	65
VII Benchmark case in thermo-hydro-mechanical phenomena arising in blast furnaces	67
7.1 Conceptual model	67
7.2 Practical significance of the project	69
7.3 Mathematical model	70
7.4 Numerical model	73
7.5 Parametrization	74
7.6 Model order reduction	74
7.6.1 Standard Krylov subspace method	75
7.6.2 Order reduction by projection	75
7.6.3 Structure-Preserving Reduced-order Interconnect Macromodelling (SPRIM)	75
7.7 Problem characteristics and Benchmark cases	75
7.7.1 Energy equation	76
7.7.2 Momentum equation	76
7.7.3 Coupling	76
7.7.4 Condition number	76
7.8 Future work	76
VIII Benchmark Case for Optimal Shape Design of Air Ducts in Combustion Engines	77
8.1 Introduction	77
8.2 The industrial partner	77
8.3 Previous scientific literature	78
8.4 Mathematical description	78
8.5 Description of the publicly available data	83

List of Acronyms

ITMATI	Technological Institute of Industrial Mathematics
USC	University of Santiago de Compostela
UDC	University of A Coruña
JKU	Johannes Kepler University Linz
RICAM	Johann Radon Institute for Computational and Applied Mathematics
AAO	Austrian Adaptive Optics Team
AO	Adaptive Optics
SCAO	Single Conjugated AO
LTAO	Laser Tomography AO
MCAO	Multi Conjugated AO
MOAO	Multi Object AO
CuRe	Cummulative Reconstructor
CuReD	Cummulative Reconstructor with Domain Decomposition
MVM	Matrix Vector Multiplication
PSF	Point Spread Function
OTF	Optical Transfer Function
WFS	Wavefront Sensor
GS	Guided Stars
NGS	Natural Guided Stars
LGS	Laser Guided Stars
CCD	Carbonate Compensation Depth
ELT	Extremely Large Telescope
FEWHA	Finite Element Wavelet Hybrid Algorithm
FWHM	Full Width at Half Maximum
PML	Perfectly Matched Layer
FEM	Finite Element Method
SEM	Scanning Electron Microscope
FFO	FreeForm Optics
OT	Optimal Transport
OE	Optical Element
MPI	magnetic particle imaging
SPIO	superparamagnetic iron oxide nanoparticles
DL	deep learning
NN	neural networks
CT	computer tomography
MRI	magnetic resonance imaging
PET	position emission tomography
FFP	field free point
FFL	field free line
FOV	field-of-view

ADMM	alternating direction method of multipliers
LISTA	Learning Fast Approximations of Sparse Coding
CNN	convolutional neural network
LSTM	long-short-term-memory network
MDF	MPI data format
RNN	recurrent neural network
BC	Boundary Condition
CC	Continuous Casting
RANS	Reynolds Averaged Navier-Stokes equations
ROM	Reduced Order Modeling
SEN	Submerged Entry Nozzle
SISSA	Scuola Internazionale Superiore di Studi Avanzati
FEM	Finite Element Method
FSI	Fluid-Structure Interaction
LIFEV	Library of Finite Elements V
LVADs	Left Ventricular Assist Devices
NS	Navier-Stokes Equations
PDEs	Partial Differential Equations
X-FEM	Extended Finite Element Method
FEM	Finite Element Method
RANS	Reynolds-averaged Navier-Stokes

Part I.

Benchmark for high-performance algorithms in adaptive optics control

Bernadett Stadler, Ronny Ramlau

Abstract

The new generation of ground-based extremely large telescopes require highly efficient algorithms to achieve an excellent image quality in a large field of view. These systems rely on adaptive optics (AO), where one aims to compensate in real-time the rapidly changing optical distortions in the atmosphere. Due to the steady growing of telescope sizes, the computational load is increasing drastically and current algorithms become infeasible. After a brief introduction to astronomical adaptive optics we compare the frequently used reconstruction method MVM to two novel ones. The first one, called Cumulative Reconstructor with Domain Decomposition (CuReD), is an extremely fast reconstruction algorithm for wavefront sensor data. The second approach is the Finite Element Wavelet Hybrid Algorithm (FEWHA), which tackles the problem of atmospheric tomography efficiently and accurately. Finally, we describe the simulation environment OCTOPUS, which is provided by the ESO and used in our benchmark cases for quality evaluation.

Keywords: Adaptive optics, wavefront reconstruction, atmospheric tomography.

1.1. Introduction

The new generation of planned earthbound Extremely Large Telescopes (ELT) aims at excellent image quality in a large field of view. Such systems rely on Adaptive Optics (AO) systems with the task to correct optical distortions caused by atmospheric turbulences.

To achieve such a correction, the deformations of optical wavefronts, emitted by natural or artificial guided stars, are measured via wavefront sensors and, subsequently, corrected using deformable mirrors (DMs). Many of such systems require the reconstruction of the turbulence profile in the atmosphere, which is called atmospheric tomography. Mathematically, such problems are ill-posed, i.e., the recovery of the solution from noisy measurements is unstable. These underlying ill-posed problems have to be solved in real-time, as the atmospheric turbulences changes within milliseconds. The complex setup of such a system, in particular the huge amount of data that has to be processed in real-time, lead to non-trivial conditions on the used algorithms.

1.1.1. Industrial Partner

Microgate [1] is an Italian company located in Bolzano. The engineering division mainly operates in the field of astronomy. Their focus lies on the development of control systems for adaptive mirrors, real time computers for adaptive optics, adaptive optics sensors and radioastronomy. These systems have become the centre of the most innovative research worldwide in the field of astronomy and are used in some of the most important new generation telescopes, e.g., VLT (Very Large Telescope), which was built by the ESO. Furthermore, the company is involved in the ELT project, covering the tasks of control system design and simulation, electronic design and electronic manufacturing.

1.2. Physical Description of the Problem - Astronomical Adaptive Optics

Turbulent air motion in the atmosphere admits fluctuations of the refractive index. Light, that is initially traveling through the atmosphere as planar waves is distorted. The aim of an AO system is to mechanically correct this distortions through deformable mirrors.



1.2.1. Basics of Imaging

In this section the complete mapping from the object emitting light to the image of this object is defined, see, e.g., [2]. We assume an object to be a cloud of point sources of light. A perfect image is the point where light rays converge in absence of perturbations due to the law of geometric optics. The real image, including optical errors, is defined by the energy distribution over the image plane and is expressed by the so called point spread function (PSF). This setting leads to the following definition of the intensity of an object

$$I_R(x, y) = \int_{\mathbb{R}^2} \mathcal{P}(x - \xi, y - \eta) \cdot I_G(\xi, \eta) d\xi d\eta, \quad (1.1)$$

which can be written as convolution

$$I_R = \mathcal{P} * I_G. \quad (1.2)$$

Using the well-known convolution theorem yields

$$\mathcal{F}\{I_R\} = \mathcal{H} \cdot \mathcal{F}\{I_G\}, \quad (1.3)$$

with $\mathcal{H} := \mathcal{F}\{\mathcal{P}\}$ called optical transfer function (OTF).

1.2.2. AO Components

The aim of an AO system is to correct optical distortions caused by atmospheric turbulences. To achieve such a correction, the system uses natural or artificial guided stars to emit the deformation of the wavefronts. The wavefronts are measured via wavefront sensors and, subsequently, corrected using DMs. In the following subsections the main components of an AO system, i.e., the guide star, the wavefront sensor and the deformable mirror are briefly described. For more details, we refer to [2].

1.2.2.1. Guide Stars

In order to reach the goals of the AO system, i.e., to correct the distortions of the wavefront, the atmosphere needs to be sufficiently known. For that purpose, light from a bright guide star (GS) is used as a reference for the AO system. Such a GS can be either a star in the sky, near the scientific object of interest, or an artificial GS generated by a powerful laser beam called natural guided star (NGS) or laser guided star (LGS), respectively. The laser beams of the LGS stimulates the sodium layer of the atmosphere, leading to disruptions in the emitted light. Therefore, in each AO setting at least one NGS is required to overcome this drawback.

1.2.2.2. Wavefront sensor

A wavefront sensor (WFS) indirectly measures the distortions of the wavefront using the light from GS. Various WFS are used in AO, however, within the framework of this project we focus on two main pupil plane WFS called Shack-Hartmann WFS and pyramid WFS.

Shack-Hartmann WFS



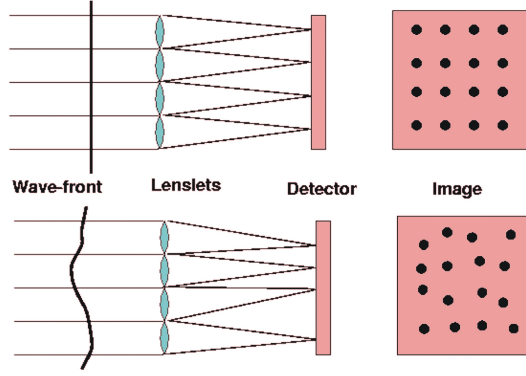


Figure 1.1: Shack-Hartman WFS [3]

A Shack-Hartmann WFS [4] consists of a quadratic array of small lenslets and a CCD photon detector lying behind that array. The quadratic subdomains of the CCD, covered by one single lenslet, are called subapertures. On each subapertures the associated lenslet focusses the light, where the x - and y -coordinates are measured. The slope of the incoming WF is related to the sensor measurements by the centre of gravity

$$S_x(x, y) = \frac{1}{|\Omega_{jk}|} \int_{\Omega_{jk}} \varphi_x(x, y) dx dy, \quad (1.4)$$

$$S_y(x, y) = \frac{1}{|\Omega_{jk}|} \int_{\Omega_{jk}} \varphi_y(x, y) dx dy, \quad (1.5)$$

where $\varphi_x := \frac{\partial \varphi}{\partial x}$ and $\varphi_y := \frac{\partial \varphi}{\partial y}$.

Pyramid WFS

The main component of the pyramid WFS [5] is a four-sided glass pyramidal prism in the focal plane of the telescope. This prism splits the incoming light into four beams. The relay lens, located behind the prism, re-images the beams leading to four different images I_1, I_2, I_3 and I_4 on the CCD camera (Figure 1.2). The two sensor measurements S_x and S_y are given by

$$S_x(x, y) = \frac{(I_1(x, y) + I_2(x, y)) - (I_3(x, y) + I_4(x, y))}{I_0}, \quad (1.6)$$

$$S_y(x, y) = \frac{(I_1(x, y) + I_4(x, y)) - (I_2(x, y) + I_3(x, y))}{I_0}, \quad (1.7)$$

where I_0 denotes the average intensity. Modulating the incoming beam dynamically allows a linearisation of the sensor and to increase its dynamic range. The modulation can be performed either by oscillating the pyramid itself or by using a static diffusive optical element. Two modulation scenarios are possible, namely circular and linear modulation.

The four-sided pyramidal prism of the sensor can be approximated via 2 orthogonally placed two-sided roof prisms. Each of the roofs creates two different images on the detector. The sensor measurements S_x and S_y are obtained by subtracting the two intensity patterns. Due to the physical decoupling of the prisms, the measurements contain information only in x - and y -direction, respectively.

1.2.2.3. Deformable Mirror

A DM consists of a thin, flexible, highly reflecting surface, which is controlled by a set of actuators that drive the mirror. There are several possibilities to drive the actuators, such as, electromechanical, electromagnetic



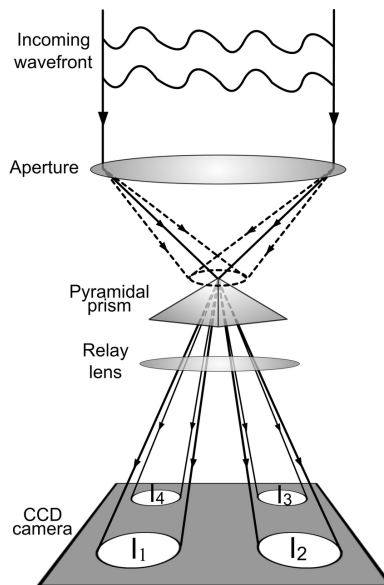


Figure 1.2: Pyramid WFS

and piezoelectric. Within the ELT, a flat adaptive mirror with approximately 5200 actuators is planned, allowing a readjusting of the surface with a very high frequency [6].

1.2.3. AO Systems

Within the framework of the benchmark cases, four AO systems were handled. These systems are briefly described in the following subsections.

1.2.3.1. Single Conjugate AO

If the object of interest, e.g., a star or a galaxy, is located near a bright NGS, the classical AO system Single Conjugate AO (SCAO) is used. In a SCAO system the wavefront is reconstructed using one WFS, that measures the data, and one DM, where the shape is chosen according to the reconstruction. The biggest problem of SCAO systems is that the further away the object of interest is from the NGS, the worse is the correction of the wavefront.

1.2.3.2. Laser Tomography AO

If no NGS is available in the vicinity of the object of interest, the usage of an SCAO system is not possible. The idea is to generate NGS to obtain a good correction. Because one NGS near the object would corrupt the image, due to the finite distance, several NGS are used in the surrounding of the field of view.

Within the framework of a laser tomography AO (LTAO) G_{LGS} and G_{NGS} are used in combination with a single mirror to reconstruct the wavefront. The correction is performed through two steps. The first step is called atmospheric tomography, where the turbulent layers are reconstructed from the sensor measurements. In the second step, the shape of the DM is chosen according to the projection of the wavefront through the reconstructed layers in the direction of interest.

1.2.3.3. Multi Object AO

In contrast to LTAO multi object AO (MOAO) corrects for multiple directions of interest, simultaneously, by using several mirrors. Each mirror corrects for a specific direction. As in the LTAO case a combination of NGS and LGS is used for reconstructing the layers.



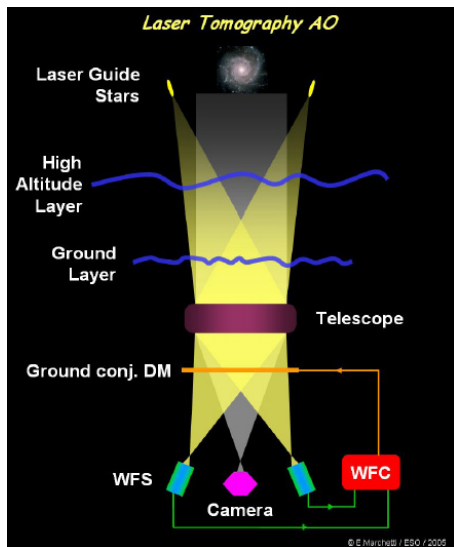


Figure 1.3: Principle of LTAO [7]

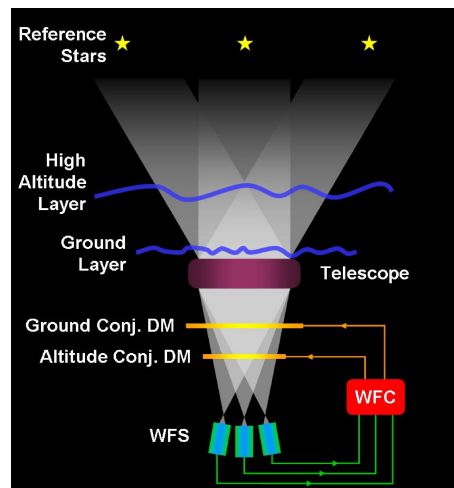


Figure 1.4: Principle of MCAO [7]

1.2.3.4. Multi Conjugate AO

As in MOAO, a Multi Conjugate AO (MCAO) system corrects for multiple directions, however, with the aim to achieve a uniformly optimal correction over the whole field of view and not into specific directions. For that purpose, several DMs are used conjugated to different heights in the atmosphere.

1.2.4. Statistics of the Atmosphere

The distortions of the wavefront are mainly caused by atmospheric turbulence which arises due to an irregular mixing of hot and cold air. The surface of the earth is heated by the sun during the day while it cools down during the night. Together with wind shears, this leads to turbulent air motions. The refractive index of the air is strongly related to the temperatures and, thus, varies due to the irregularities throughout the atmosphere. For this reason, the wavefront, which initially propagates as plane waves, is distorted. In many applications it is sufficient to use a layered model of the atmosphere, i.e., to assume that the turbulence is concentrated on $L \in \mathbb{N}$ layers at certain height.

Usually, the effects of the turbulences are not predictable and, therefore, modelled by random processes. In AO, one assumes to sufficiently know the physics of the atmosphere. There are two very important models, according to Kolmogorov and von Karman, which are briefly described in the following subsections.

1.2.4.1. Kolmogorov Turbulence Model

According to Kolmogorov [8] the behaviour of the atmosphere is modelled via an isotropic, stationary random process. The structure of this random process is based on the structure function, describing the expected difference of values at two points and the covariance function, measuring the spatial covariance. Because we are dealing with a stationary process, both functions only depend on the separation Δx and not on a specific point x .

The structure function of a stationary process f is given by

$$D_f(\Delta x) := \mathbb{E}((f(x + \Delta x) - f(x))^2), \quad (1.8)$$

and the covariance is defined by

$$C_f(\Delta x) := \mathbb{E}((f(x) - \mathbb{E}(f))(f(x + \Delta x) - \mathbb{E}(f))). \quad (1.9)$$

The power spectral density (PSD) characterizes the behaviour of the covariance function in the Fourier Domain and is defined by

$$\Phi_f(\Delta x) := \mathbb{E}((f(x) - \mathbb{E}(f))(f(x + \Delta x) - \mathbb{E}(f))). \quad (1.10)$$

Kolmogorov's theory is constricted by two quantities, namely l_0 and L_0 called inner and outer scale, respectively. The inner scale represents the size of the smallest eddy in the turbulence, whereas the outer scale corresponds to the largest size. Within this range, Kolmogorov stated that the structure function of the refractive index of the atmosphere at a certain height h is given by

$$D_f(\Delta x) := C_n^2(h)|\Delta x|^{2/3} \text{ for } l_0 < |\Delta x| < L_0. \quad (1.11)$$

The PSD of the refractive index n is then defined as

$$\Phi_n(\kappa) := 0.033C_n^2(h)|\kappa|^{-11/3} \text{ for } 2\pi L_0^{-1} < |\kappa| < 2\pi l_0^{-1}. \quad (1.12)$$

The behaviour of the PSD due to Kolmogorov's theory is only given within the so called inertial range, defined by the inner and outer scale. For a very small $|\kappa|$, i.e., turbulent eddies larger than the outer scale, Kolmogorov's model shows problems due to the singularity.

1.2.4.2. Von Karman Turbulence Model

The von Karman model [9] modifies the Kolmogorov model in order to overcome the problem with the singularity at $\kappa = 0$. This leads to the following definition of the power spectral density

$$\Phi_f(\kappa) = \frac{0.033C_n^2(h)}{(|\kappa| + \kappa_0^2)^{11/16}} \exp\left(-\frac{|\kappa|^2}{\kappa_m^2}\right), \quad (1.13)$$

with $\kappa_0 = 2\pi L_0^{-1}$ and $\kappa_m = 5.92l_0^{-1}$.

1.3. Mathematical Description of the Problem

Within the framework of this project, we are dealing with two different mathematical problems. The first one consists of the reconstruction of the incoming, distorted wavefront, either from a Shack-Hartman WFS or a Pyramid WFS. The second problem deals with atmospheric tomography, where we assume a layered model of the atmosphere, with the aim to reconstruct the turbulent layers.

1.3.1. Wavefront Reconstruction

In general, the data s , obtained from a wavefront sensor, is related in a non-linear way to the wavefront ϕ

$$s = Q\phi + \eta, \quad (1.14)$$

where Q denotes the non-linear WFS operator and η models the noise with variance σ_n^2 . The reconstruction of the wavefront from sensor data is an inverse problem and, thus, requires regularization techniques to obtain a stable solution. Beside a wavefront sensor, an AO systems requires an active control device, that corrects the wavefront, and a control algorithm, that connects the measurements s with the control commands a_i . The



whole process leads to the wavefront correction

$$\phi_{correct} = Ha = \sum_i a_i h_i, \quad (1.15)$$

where h_i is called influence function. This problem can be formulated as minimization of the corresponding noise-weighted least squares functional

$$J_c(a) = \|QHa - s\|_{C_\eta^{-1}}^2. \quad (1.16)$$

In the following subsections two common algorithms for solving the problem of wavefront reconstruction are briefly described. The first is the standard approach in AO, however, has some problems from the computational point of view while dealing with very large telescope as the ELT. The second algorithm was developed by the Austrian Adaptive Optics team (AAO) composed of JKU, RICAM and MathConsult.

1.3.1.1. Matrix-Vector Multiplication

Matrix-vector multiplication (MVM), see, e.g. [10], is the most utilized algorithm in the area of AO. Within the setting of MVM, the WFS is assumed to be linearly related to the DM via an interaction matrix P . This interaction matrix, also called control matrix, maps the DM commands to the sensor measurements. The wavefront reconstruction is then obtained via the inverse of the control matrix. In particular, regularisation is performed using the pseudo inverse P^\dagger as an approximation, since, P is ill-conditioned. The big advantage of this method is that it is highly parallelizable and pipelineable. Furthermore, it can handle the modulated as well as the non-modulated pyramid WFS. However, it is extremely time consuming and, thus, not feasible for large scale AO settings, as it is the case within the ELT.

1.3.1.2. Cumulative Reconstructor with Domain Decomposition

To overcome the run-time problem of the MVM an alternative algorithm was developed by the AAO team, called Cumulative Reconstructor (CuRe) or in the enhanced version Cumulative Reconstructor with Domain Decomposition (CuReD) [11]. Instead of $\mathcal{O}(n^2)$, which denotes the computational costs of the MVM algorithm, the CuRe can perform wavefront reconstruction in $\mathcal{O}(n)$ and is still parallelizable and pipelineable. Originally, the algorithm was developed for Shack-Hartman WFS, however, using a pre-processing step makes an extension to pyramid WFS possible.

The idea of CuRe is to utilize a modified Hudgin geometry to discretize the domain. In contrast to the Fried geometry, where sensor measurements are obtained using corner points of the subapertures, here, the Shack-Hartman sensor measurements are obtained by subtracting the center of sides

$$s_x[i, j] := \phi[i, j - \frac{1}{2}] - \phi[i - 1, j - \frac{1}{2}], \quad (1.17)$$

$$s_y[i, j] := \phi[i - \frac{1}{2}, j] - \phi[i - \frac{1}{2}, j - 1]. \quad (1.18)$$

This decouples the measurements in x - and y - direction and, thus, allows the construction of independent chains along one-dimension. The reconstruction of the wavefront is performed from averaged gradients via an integration method, using an iterative scheme

$$l_x[i + 1, j - \frac{1}{2}] := l_x[i, j - \frac{1}{2}] + s_x[i + 1, j], \quad (1.19)$$



$$l_y[i - \frac{1}{2}, j + 1] := l_y[i - \frac{1}{2}, j] + s_y[i, j + 1]. \quad (1.20)$$

The remaining step is to correct the alignment, i.e., to connect the chains, which is done by a shift operation such that the mean value is equal to zero. The construction of the trend chains is based on rectangular domains, however, telescope apertures have usually a circular domain with central obstruction, thus, an adaption is required. Instead of this general trend, the common boundary of the respective subapertures is utilized to compute the alignment of two neighbouring chains.

A drawback of the CuRe is the bad noise propagation for large WFS, as it is the case within the ELT. For that purpose, the CuRe has been extended by a domain decomposition step leading to the CuReD algorithm. The idea is to divide the aperture into smaller domains (domain decomposition) and apply the CuRe on each subdomain. The small parts are then stitched together via their boundaries, to obtain the whole reconstructed wavefront.

As mentioned in the beginning of this section, originally, the CuReD was developed only for Shack-Hartman WFS. To deal with pyramid type WFS as a first step the data preprocessing transforms the pyramid sensor measurements into Shack-Hartman data. In a second step, the CuReD is applied to the preprocessed data. This concept is then called P-CuReD algorithm [12].

For the preprocessing step, a roof approximation of the pyramid WFS is utilized, which decouples the two measurement directions, allowing to perform operation on s_x only row-wise and on s_y only column-wise. The analytical Fourier domain relation between the two sensor data is then used to map the pyramid sensor data into Shack-Hartman like data.

1.3.2. Atmospheric Tomography

Atmospheric Tomography is the fundamental problem in many AO systems, e.g., LTAO, MOAO and MCAO. Assuming a layered model of the atmosphere, the goal of the atmospheric tomography problem is to reconstruct the turbulent layer from the WFS measurements. This turbulent layers are related to the WFS measurements by

$$s_g = \mathcal{T}_g \mathcal{P}_g \phi, \quad (1.21)$$

where $\phi = (\phi_1, \dots, \phi_L)$ denotes the L turbulent layers a heights $0 \leq h_1 < \dots < h_L$. The operator \mathcal{P}_g is a geometric propagation operator towards one of the GS $g = 1, \dots, G$ and \mathcal{T}_g is the WFS operator. The vector s_g contains the WFS measurements for the GS g .

The atmospheric tomography problem is defined by

$$s = A\phi, \quad (1.22)$$

where $A = (A_1, \dots, A_G)$ with $A_g := \mathcal{T}_g \mathcal{P}_g$ for $g = 1, \dots, G$.

This problem is extremely ill-posed, due to the small angle of separation. Often, it is formulated in the Bayesian framework, since, this allows incorporating statistics of turbulence and noise into the model [13].

Fur that purpose, random variables for the measurements and the turbulent layers in combination with additive noise are used to define (1.22) in a stochastic setting

$$S = A\Phi + \eta. \quad (1.23)$$

The random variables Φ and η are modelled as Gaussians with zero mean and covariance matrices C_Φ and C_η , respectively. The layers are statistically independent, hence, the covariance matrix C_Φ has a block diagonal structure. The optimal solution to the above described setting is the maximum a-posteriori estimate (MAP)

$$\phi_{MAP} = \operatorname{argmin}_\phi \|C_\Phi^{-1/2} \phi\|^2 + \|C_\eta^{-1/2} (s - A\phi)\|^2. \quad (1.24)$$

Solving this equation is equivalent to solve the linear system of equations

$$(A^* C_\eta^{-1} A + C_\Phi^{-1}) \phi = A^* C_\eta^{-1} s. \quad (1.25)$$

The inverse of C_η has a sparse representation, however, the sparsity of C_Φ^{-1} and A depends highly on the discretization of the problem.

In the following subsections two algorithms for solving the atmospheric tomography problem are described. The first one is the MVM, which can be generalized in order to perform wavefront reconstruction and atmospheric tomography. The second approach was, as the CuReD, developed by the AAO team.

1.3.2.1. MVM

The MVM method, as described in Section 1.3.1.1, can be generalized in order to perform wavefront reconstruction and atmospheric tomography, see, e.g., [13], by applying one matrix P^\dagger to the sensor measurements. Certainly, the run-time problem gets of course more present, since we are dealing here with an even bigger amount of data and, thus, rather large matrices P and P^\dagger .

Within the Bayesian framework the control matrix is given by

$$P = (A^* C_\eta^{-1} A + C_\Phi^{-1}) A^* C_\eta^{-1}, \quad (1.26)$$



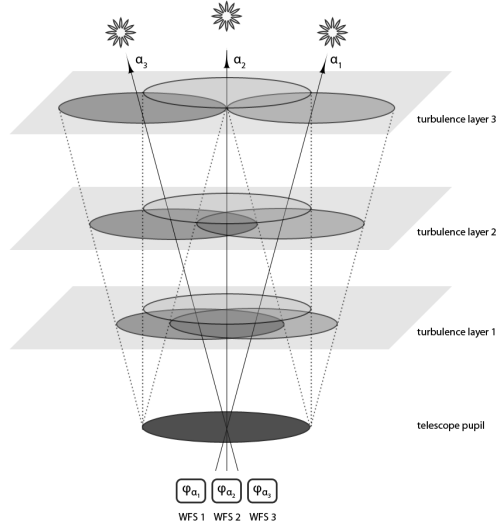


Figure 1.5: Atmospheric Tomography

and can be computed explicitly. For every specific geometry, every certain noise and turbulence parameters of the layers the inverse has to be recomputed. P is a full matrix, hence the method scales with $\mathcal{O}(n^2)$ operations. The MAP estimate is then obtained by a matrix-vector multiplication

$$\phi_{MAP} = Ps. \quad (1.27)$$

As already mentioned in Section 1.3.1.1, due to parallelization and pipelining the method is still efficient, although, for large telescopes as the ELT not feasible.

1.3.2.2. Finite Element Wavelet Hybrid Algorithm

The Finite Element Wavelet Hybrid Algorithm (FEWHA) [14] is an iterative method to compute the MAP estimate. The idea behind is to use compactly supported orthonormal wavelets for representing the turbulent layers.

In the frequency domain, these wavelet representation allows a completely diagonal approximation of the penalty term in (1.24). To achieve a sparse representation for the fitting term, discretization is applied using a piecewise bilinear basis of finite elements.

Turbulence Statistics in the Wavelet Domain

In order to obtain a diagonal approximation of the penalty term, first, we discretize the turbulence layers in the wavelet domain

$$\phi(x, y) = \sum_{j \in \mathbb{Z}} \sum_{k \in \mathbb{Z}} \sum_{t=1,2,3} \langle \phi, \psi_{jk}^t \rangle \psi_{jk}^t(x, y), \quad (1.28)$$

for $(x, y) \in \mathbb{R}^2$.

Furthermore, we assume that the spectral density of the turbulent field satisfies the von Karman model. Thus, the covariance operator of the layer ϕ at height h can be written as

$$C_\phi = c(h)\mathcal{F}^{-1}m\mathcal{F}, \quad (1.29)$$



where m is the spectral density and $c(h)$ a height dependent constant defined by

$$c(h) = \frac{0.023r_0^{-5/3}\lambda^2 C_n^2(h)}{4\pi^2}. \quad (1.30)$$

For any $f \in C_0^\infty(\mathbb{R}^2)$ the penalty term of (1.24) can be approximated by

$$\|C_\phi^{-1/2}f\|_{L^2}^2 \simeq \frac{1}{c(h)}(\kappa_0^{11/3}\|f\|_{L^2}^2 + \|(-\Delta)^{11/12}f\|_{L^2}^2). \quad (1.31)$$

Since, we are only interested in reconstructing the turbulent domain on a bounded region (region of interest), we consider the periodically extended wavelets on the domain

$$\Omega_\phi = [0, \delta(2^J - 1)^2] - \xi, \quad (1.32)$$

where J denotes the number of wavelet scales in the discretization, $\delta > 0$ is a scaling factor and $\xi \in \mathbb{R}^2$ represents the shift away from the origin.

In the discrete case, the function f in (1.31) is represented by a finite number of wavelet coefficients. Using the Bernstein-Jackson inequalities, this leads to an equivalent representation for the regularizing term by a diagonal matrix D with

$$D_{\lambda\lambda} = \frac{1}{c(h)}(\kappa_0^{11/3} + 2^{(11/3j)}), \quad (1.33)$$

where $\lambda = 0, \dots, 2^{2J-1}$ is the global wavelet index and $j = 0, \dots, J-1$ corresponds to the scale index. The described concept is extended to L turbulent layers $\mathbf{CE} = (\phi_1, \dots, \phi_L)$ at heights $0 \leq h_1 < \dots < h_L$ by introducing the square domain Ω_l and the diagonal matrix D_l . For the full problem we define the block-diagonal matrix

$$\mathbf{D} = \text{diag}(D_1, \dots, D_L). \quad (1.34)$$

Finally, the penalty term is approximated by

$$\|\mathbf{CCE}^{-1/2}\phi\|_{L^2}^2 = \sum_{l=1}^L \|C_l^{-1/2}\phi_l\|_{L^2}^2 \simeq \sum_{l=1}^L (D_l c_l, c_l)_2 = (\mathbf{Dc}, \mathbf{c}). \quad (1.35)$$

Atmospheric Tomography in the Wavelet Domain

To obtain a sparse representation of the fitting term in (1.24) the atmospheric tomography operator A is discretized in the wavelet domain. The computation of the operator can be reduced to an one-dimensional evaluation of one-dimensional wavelet functions.

The operator A has a block-component representation

$$\mathbf{A} = \begin{pmatrix} \Gamma_{11}^{LGS} & \dots & \Gamma_{1L}^{LGS} \\ \vdots & & \vdots \\ \Gamma_{G1}^{LGS} & \dots & \Gamma_{GL}^{LGS} \end{pmatrix}, \quad (1.36)$$

where Γ_{gl}^{LGS} and $\Gamma_{g'l}^{NGS}$ denote the Shack-Hartmann operators in LGS and NGS direction, respectively.

The domains, observed by a WFS in direction $\theta_g = (\theta_g^x, \theta_g^y, 1)$ of a LGS and NGS, respectively, are given by

$$\Omega_{gl}^{LGS} := (1 - \frac{h_l}{H})\Omega + (\theta_g^x, \theta_g^y)h_l \quad (1.37)$$

$$\Omega_{g'l}^{NGS} := \Omega + (\theta_{g'}^x, \theta_{g'}^y)h_l. \quad (1.38)$$



Each turbulent layer ϕ_l , defined by (1.32), is observed by all WFSs, thus, the following condition must hold,

$$\left(\bigcup_{g=1}^{G_{LGS}} \Omega_{gl}^{LGS} \right) \cup \left(\bigcup_{g'=G_{LGS}+1}^G \Omega_{g'l}^{NGS} \right) \subseteq \Omega_l. \quad (1.39)$$

The two Shack-Hartman operators Γ_{gl}^{LGS} and $\Gamma_{g'l}^{NGS}$ are defined on the domains Ω_{gl}^{LGS} and $\Omega_{g'l}^{NGS}$, respectively. The LGS operator consists of a concatenation of two components, associated to the x - and y - direction, respectively, where each component has a matrix representation. Using the fact that the scaling and wavelet functions have a multiplicative representation, the assembly of the matrices Γ_{gl}^{LGS} and $\Gamma_{g'l}^{NGS}$ can be reduced to a one-dimensional evaluation of one dimensional scaling and wavelet functions over the edges of the projected subapertures.

Finally, this concepts allows to define the discretization of equation (1.25) in the wavelet domain

$$(\tilde{A}^T C_\eta^{-1} + \tilde{A} + \alpha D)c = \tilde{A}^T C_\eta^{-1} s, \quad (1.40)$$

where \tilde{A} is the atmospheric tomography operator in the wavelet domain.

1.4. Quality Evaluation

In order to evaluate the benchmark cases, i.e. the quality performance of an AO system, a variety of measures are available. In the following subsections we briefly describe two of them. However, in further deliveries we will focus on the Strehl ratio for evaluating the quality in the numerical examples.

1.4.1. Strehl Ratio

The Strehl ratio is the rate between the real energy distribution $I(x, y)$ and the hypothetical distribution obtained in diffraction-limited imaging and is defined by

$$S := \frac{\max_{(x,y)} I(x, y)}{\max_{(x,y)} I_D(x, y)}. \quad (1.41)$$

This formula leads to a quantity between 0 and 1, that increases with quality and reaches its maximum value 1 in diffraction-limited case. It is common to state the Strehl ratio in $100 \cdot S\%$.

Marechal Criterion

If the system fulfils the Marechal criterion

$$S \geq 0.8, \quad (1.42)$$

it is called well-corrected [2]. In this case the Strehl ration can be approximated by

$$S \approx \exp\left(-\int \Delta\varphi^2 d\mathbf{x}\right). \quad (1.43)$$

This expression allows a much faster evaluation, since the Fourier transform is avoided. The problem, however, is that in practice it is often not fulfilled. Nevertheless, the approximation can be used to compare different reconstruction methods, which is the case when comparing various benchmarks. Although, it might not be a good approximation to S , it is still known that the reconstruction quality is related monotonically to it.



1.4.2. Full Width at Half Maximum

Another common quality measure is the Full Width at Half Maximum (FWHM), which is deduced from the PSF. It is defined as the width of the PSF at the point where the intensity is one half of the maximum intensity. For the optical density I it is defined by

$$FWHM(I) := \text{diam}\{\mathbf{x} \in \mathbb{R}^2 | I(\mathbf{x}) \geq \frac{1}{2} \max |I|\}. \quad (1.44)$$

1.5. Description of Data

To evaluate the quality of the algorithms, they are tested using numerical simulations. For that purpose, the official end-to-end simulation tool established by the ESO, called OCTOPUS, is used. OCTOPUS [15] simulates a complete telescope and all its components, as well as the perturbation of light travelling through the turbulent atmosphere. The simulation of the atmosphere is based on the assumption of a layered structure of perturbations.

The big advantage of OCTOPUS is that external reconstruction algorithms can be implemented in any language and started as a separate process parallel to OCTOPUS. The transfer of data between the two processes is managed via files, that have a specified syntax. In a first step, OCTOPUS writes the sensor measurements to a file and, furthermore, a signal to be finished. Then the external reconstruction algorithm, waiting for this signal, reads the sensor measurements and performs wavefront reconstruction or atmospheric tomography. The result of the algorithm are actuator commands in order to adapt the DM, which again are written to a file. The algorithm finishes, by writing a signal for which OCTOPUS is waiting. OCTOPUS then updates the DM shape and provides the new sensor measurements. This loop is continued until a predefined number of time steps.



Part II.

Benchmark cases in development of coupled models for a sound intensity probe

Ashwin Nayak, Andrés Prieto, Daniel Fernández

Abstract

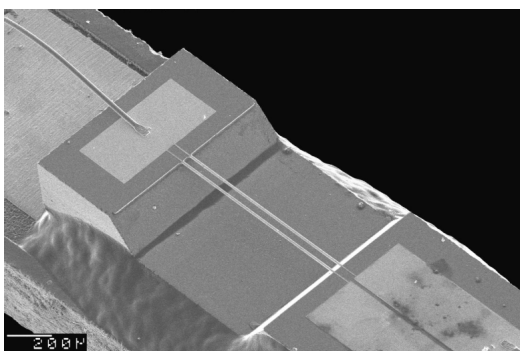
We present the progress towards the development of a mathematical model and simulation for better understanding of the physical processes behind a sound intensity PU probe. The particle velocity sensor and the sound pressure microphone are mounted on two closely spaced cylinders which are protected with a porous windscreen. We evaluate the possibilities of using different porous enclosures around the probe to improve its sensitivity and response to air flow through the means of a mathematical model. A thorough physical model can help optimize the design criteria and enhance the signal quality. This preliminary report discusses the impact of the windscreen on the sensor's outputs by simulating their physical behavior in multiple stages. Benchmark stages are identified along the development to highlight progress and initial approach is explained. The response is measured by simulating a simplified model and the gain is computed and compared.

Keywords: Scattering, aeroacoustics, porous materials.

2.1. Introduction

The Microflow PU probes are acoustical sensors distinguished by their ability to measure fluctuations in particle velocity and pressure fields simultaneously and are of considerable importance in sound measurement. They have been used to measure sound-intensity, acoustic impedance, pressure and have been adopted for a variety of applications like sound localization, acoustic quantification and noise control. In the past 24 years since its invention at University of Twente unto present, it is said to be the only sensor to measure particle velocity directly off the acoustic field.

The sensor works on the principal of differential heating. The microscopic transducer (Fig2.1a) consists of a two tiny, resistive strips of platinum which measure the acoustic particle velocity. In the presence of particle velocity, the temperature distribution around the resistors is asymmetrically altered, and a difference in temperature occurs between the two wires, as the upstream wire is cooled more than the downstream wire by the acoustic airflow. The resulting resistance difference translates into variations in a signal which captures the particle velocity of a single point of a sound field in an arbitrary direction.



(a)



(b)

Figure 2.1: (a) SEM image of the Microflown's particle velocity transducer, and (b) the PU Probe housing the particle velocity and pressure sensors

The Microflown sensor being used in different environmental conditions, is observed to be sensitive to flow

conditions. Since the transducer is mainly a thermal device, the probe wires have to be heated for proper operation. Previous models of the microflow transducers [16], [17] indicate that at large flow velocities, the metal wires, having a finite heat capacity, cool down and the signal can distort considerably or die down unexpectedly. Due to this physical limitation, the sensor is usually used with a windscreen when measurements are taken in an environment which has a significant air flow. The company offers multiple windscreens in various sizes and materials, from cylindrical porous covers to metallic meshes.

Even while the flow is sufficiently blocked, the low frequency variations in the flow may still be large enough to cause problems when amplified. Studies indicate that windscreens on the sensor may induce significant package gain and phase error in the particle velocity measurements [18],[19]. If the wind is sufficiently blocked, the low frequency variations in the flow may still be large enough to cause problems when amplified. Also at higher flow velocities, any introduction of physical obstacle may cause turbulence which effectively translates into acoustic noise. Moreover, since the self noise induced by the flow is used as reference from which the noise is measured, a dynamic calibration maybe required in such cases. Hence, different wind-screening strategies should be considered with the aim of mitigating such effects on the probe measurements.

The objective of this project is to study the effects of introducing a porous media layer over a sound intensity PU probe to prevent noise inhibitions whist a broadband frequency response. A computational model which simulates the behaviour of the sensor can highlight the physical characteristics and help optimize the design for improving the measurement. This report shows the approach towards development of such a model and preliminary results in this regard by trying to measure the impact of the windscreen of the sensor on its measurement.

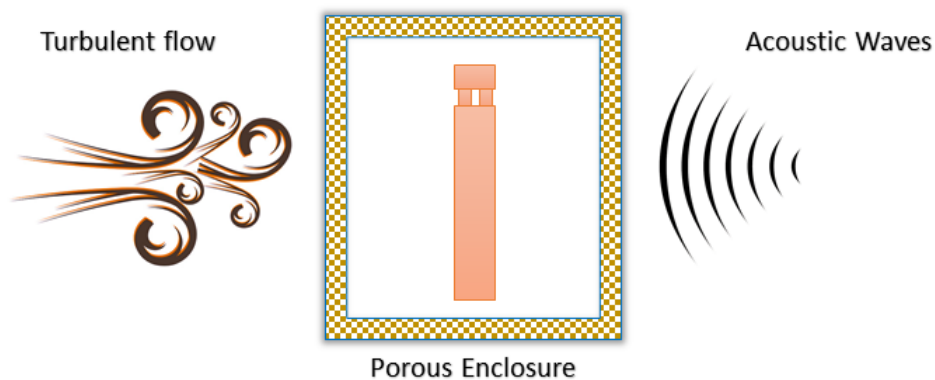


Figure 2.2: Schematic of the target coupled problem

2.2. Model development

The physical behaviour of the acoustical sensor enclosed by a porous material in flow requires an astute understanding of sound propagation over the porous structure in different flow conditions. The material properties and geometry of the porous windscreen can either dampen or accentuate either the magnitude or the phase of the measured signal. Additionally, turbulence in the acoustic fluid can give rise to noise at various frequency ranges. In order to predict these responses accurately it is necessary to model the coupling between the various physical models of flow and structure.

We consider the development of a computational model to simulate such coupled behaviour in 6 stages as shown in Fig 2.3. Each stage is represented by a schematic diagram indicating the coupling required. For simplicity, we begin the model development with a spherical geometry in free-field conditions with fluid at rest and an incident acoustic wave. The model plainly describes the effect of placing a sphere in an acoustic field. This is easily quantified by measuring the signal characteristics close to the sphere with the known analytic expression thereby giving us the gain or loss in signal. The model is further developed to incorporate the coupling with the porous material to help understand the acoustic behaviour in presence of such a windscreen.



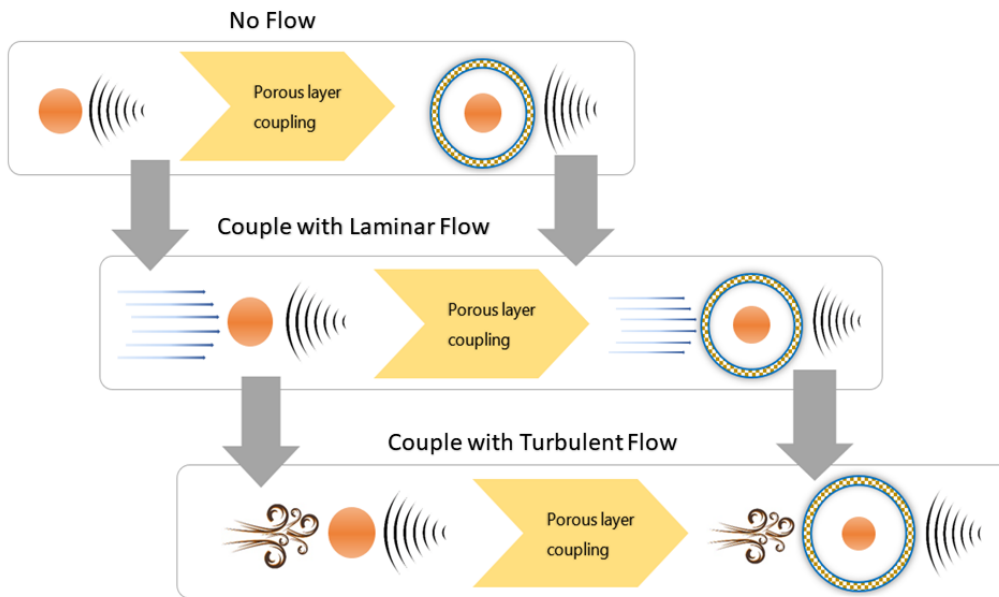


Figure 2.3: Schematic of the model development hierarchy for the different couplings. The orange blob represents a simplified geometry, acoustic waves are represented as concentric wavy arcs, porous windscreen with the checkered layer, laminar flow as straight blue arrows and turbulent flow with the swirls

To study the effects of flow on the acoustic fluid, we then start with coupling the initial model with the fluid assumed to be laminar and non-viscous. This model is also later evolved to incorporate a porous housing. Turbulent behaviour is incorporated at last after a thorough understanding of the flow characteristics in the laminar regime. Finally, including a porous windscreen within it, we arrive at the target model to study the behaviour of the all these coupling events.

2.3. Benchmark Cases

The previous section indicated the various stages of development of the mathematical model towards modeling the porous windscreen on the sound intensity PU probe. We discuss here, the application of each of the model stages on the probe which can help validate the model at the various stages. Each such application can be considered a benchmark case to assess the project development.

Each stage of the mathematical model developed can be tested and validated by comparing the numerical results obtained to experimental data obtained from the company. Table 1 lists each of the six cases along with the schematic representation. Once the mathematical model is developed for a simplified geometry in no-flow conditions, the same model may be applied to the probe housing to study the theoretical effect of its presence in the measurement. The numerical results obtained can be verified experimentally to validate the results. The model is then developed to couple with the material properties of a porous windscreen, to arrive at the predicted difference in gain of the particle velocity signal. This can again, be corroborated by reproducing the experiment in a laboratory setup.

Adding flow conditions to the initial model will require re-examining the basic conservation principles and arrive at a different mathematical model. As before, it can be used to obtain an estimate of difference gain and phase response of the signal and be validated with experiments. At each stage, details of the model, the results obtained from the model and the data obtained from experiments are enumerated and compared. We begin with the easier laminar flow models at lower Reynolds number. Once validated, we proceed to couple it with the material response of the porous windscreen of the sensor. The results are then validated with reproducing the conditions in laboratory. Subsequently, turbulent models are developed and again be verified by experiments.

The methodology is developed over the course of the project and presently, we begin by modelling the simplest case of no-flow conditions with no porous windscreen.


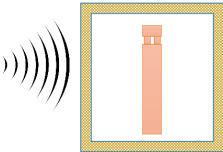
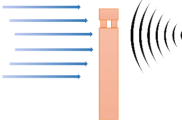
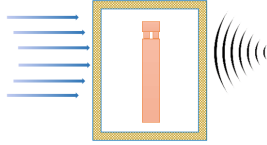
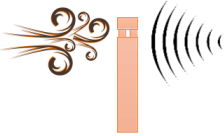
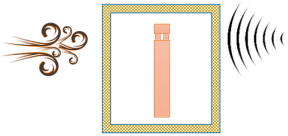
Case	Description	Schematic Representation
1	Mathematical model of acoustic fluid with fluid at rest	
2	Coupled model with porous windscreen and fluid at rest	
3	Mathematical model of acoustic field in laminar flow	
4	Coupled model with porous windscreen in laminar flow	
5	Mathematical model of acoustic field in turbulent flow	
6	Coupled model with porous windscreen in turbulent flow	

Table 1: Benchmark Cases

2.4. Case 1: Fluid at rest

2.4.1. Computational Model

To study the effects of the windscreen on the probe measurement, we study the simple scattering problem on the PU probe in free-field conditions. The acoustic fluid around the field is assumed homogeneous, non-viscous, compressible, and at isentropic regime. A plane wave is assumed to impinge on the probe from the x -direction. The pressure field of the fluid is $P(\mathbf{x}, t)$, the density field is $\rho(\mathbf{x}, t)$ and the velocity vector field is $\mathbf{U}(\mathbf{x}, t)$. With these assumptions, to obtain the equations governing the acoustic wave propagation, we consider the conservation equations of mass and momentum:

$$\frac{\partial \rho}{\partial t} + \nabla \cdot (\rho \mathbf{U}) = 0, \quad (2.1)$$

$$\rho \frac{\partial \mathbf{U}}{\partial t} + \nabla P = 0. \quad (2.2)$$

We also need constitutive assumptions which characterize the relation between state variables in the medium. With the assumption of acoustic fluid being compressible, we obtain the linear relation

$$P = c^2 \rho, \quad (2.3)$$

where the material constant c is the speed of sound in the fluid. Using (2.1), (2.2) and (2.3), we obtain the equation governing the acoustic wave propagation as,

$$\frac{1}{c^2} \frac{\partial^2 P}{\partial t^2} = \Delta P. \quad (2.4)$$

2.4.1.1. Helmholtz problem

The time-harmonic assumption suggests that a sound signal can be partitioned over the frequency bands and the pressure field for a given frequency ω may be expressed as,

$$P(\mathbf{x}, t) = p(\mathbf{x}) \exp(-i\omega t). \quad (2.5)$$

Using this, the wave equation (2.4) becomes,

$$-\Delta p - k^2 p = 0, \quad (2.6)$$

known as the *Helmholtz equation*. The constant $k = \omega/c$ is called the acoustic wave number. While this equation describes the propagation of pressure perturbations within the acoustic field, it needs to be closed by prescribing the right boundary conditions.

2.4.1.1.1. Boundary conditions In order to setup a scattering problem, it is necessary to introduce the plane wave as a boundary condition. A plane wave is a solution of the Helmholtz equation of a particular form:

$$p_{\text{inc}}(\mathbf{x}) = A \exp(-i\mathbf{k} \cdot \mathbf{x}), \quad (2.7)$$

where, \mathbf{k} represents the wave number vector. This vector has the magnitude of the wave number k and the direction along the propagation of the plane wave. It is necessary to impose this on the structure boundary as a coupling condition with the fluid. Since, the probe body is considered rigid, Neumann boundary conditions are assumed on its boundary, i.e.,



$$\frac{\partial p}{\partial \mathbf{n}} = -\frac{\partial p_{\text{inc}}}{\partial \mathbf{n}}. \quad (2.8)$$

Here, p_{inc} is the pressure of the incident plane wave which hits the structure and \mathbf{n} represents unit vectors on the surface.

Since the study is at free-field conditions, the scattering problem also requires that the acoustic field vanish at points further away from the domain of interest. This can be written as the Sommerfeld boundary condition in radial coordinates i.e.,

$$\lim_{r \rightarrow \infty} r \left(ikp - \frac{\partial p}{\partial r} \right) = 0, \quad (2.9)$$

with $r = \|\mathbf{x}\|$ being the radial distance from the origin. While this non-reflective boundary condition is theoretically suitable, it is particularly hard to implement in analytical calculations [20, 21]. In a practical scenario, the domain needs to be truncated at some finite distance and this would introduce spurious reflections off the boundary.

This necessitates that we introduce an artificial boundary around the truncated domain and prescribe 'absorbing' boundary conditions that incorporate (exactly or approximately) the far-field behaviour into the model. The Perfectly Matched Layer is one such technique in this regard which mimics free-field conditions on the fluid domain.

2.4.1.2. The PML method

The Perfectly Matched Layer (PML) method is a recently developed technique as a kind of absorbing boundary condition on an artificial boundary around the domain of interest which equivalently replaces the Sommerfeld condition. The idea, inspired from electromagnetic simulations, is specifically to introduce an exterior layer at the boundary in such a way that all plane waves are totally absorbed. This allows for an efficient approach towards utilizing the techniques for bounded-domain models of wave propagation on unbounded domains. For an arbitrary incident plane wave on the exterior layer, no reflection occurs and the transmitted waves are designed to vanish at infinity [21].

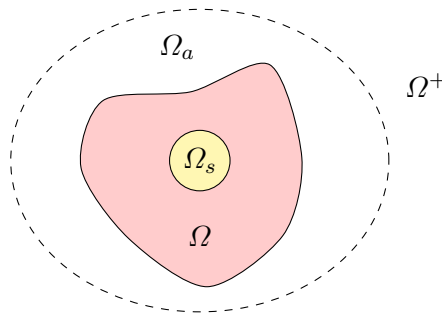


Figure 2.4: Schematic of Perfectly Matched Layers

Consider a structural domain Ω_s which is to be surrounded by seemingly, free-field conditions. Figure 2.4 shows the domain of interest, Ω^+ , truncated at some finite region and surrounded by an artificial boundary layer, Ω_a . To obtain the partial differential equations associated with the fluid in Ω_a , a formal complex-valued change of variables is introduced in the Helmholtz equation. The partial derivatives in space along each direction, i.e $\partial/\partial x_j$ are scaled by complex-valued factors $1/\gamma_j$, with,

$$\gamma_j = 1 - i \frac{\sigma_j}{\omega} \quad \text{for } j = 1, 2, 3. \quad (2.10)$$

The functions σ_j are called the absorption functions of the PML. In our case we assume them to be piecewise



constant given as,

$$\sigma_j = \begin{cases} \sigma_0 & \text{if } x_j \in \Omega_a, \\ 0 & \text{if } x_j \in \Omega. \end{cases} \quad (2.11)$$

The values σ_0 for the PML layer is hence, dependent on the frequency of the acoustic field. Hence, an optimal value needs to be arrived at for each frequency. With these change of variables, the PML governing equation can be written for the domain $\Omega \cup \Omega_a$ as follows:

$$-\nabla \cdot (C\nabla p) - k^2 M p = 0, \quad (2.12)$$

where

$$C = \text{diag}\left(\frac{\gamma_2\gamma_3}{\gamma_1}, \frac{\gamma_3\gamma_1}{\gamma_2}, \frac{\gamma_1\gamma_2}{\gamma_3}\right) \quad \text{and} \quad M = \gamma_1\gamma_2\gamma_3.$$

Note that within Ω , the equation (2.12) reduces to the Helmholtz equation. To close the problem, it is also necessary to mention the boundary condition of this PDE (2.13). The conditions on the exterior of the artificial boundary $\partial\Omega_a$ have not jump discontinuities (the jump of a quantity is denoted between brackets):

$$\begin{aligned} \frac{\partial p}{\partial n} &= g \quad \text{on } \partial\Omega_s, \\ p &= 0 \quad \text{on } \partial\Omega, \\ [p] &= 0 \quad \text{on } \partial\Omega_a, \\ \left[\left(\frac{1}{\gamma_x} \frac{\partial p}{\partial x}, \frac{1}{\gamma_y} \frac{\partial p}{\partial y}, \frac{1}{\gamma_z} \frac{\partial p}{\partial z} \right) \cdot \mathbf{n} \right] &= 0 \quad \text{on } \partial\Omega_a. \end{aligned} \quad (2.13)$$

2.4.1.3. Finite Element Method

The Finite Element Method (FEM) enables solving a problem in infinite-functional space approximately by means of a finite-dimensional discrete space. The model described below describes this method applied for acoustic problems in the unbounded domains with a perfectly matched layer (PML). First, the PDE which is to be solved in the domain is framed as a variational problem (also known as the weak formulation). For this, we multiply equation (2.12) by the complex test function φ , write all the complex terms explicitly and utilize the Green's identity to obtain,

$$\int_{\Omega \cup \Omega_a} C\nabla p \cdot \nabla \varphi dV - \int_{\Omega \cup \Omega_a} k^2 M p \varphi dV = \int_{\partial\Omega_s} g \varphi d\gamma. \quad (2.14)$$

Note that the boundary conditions appear as terms on left hand side of the above equation. This complex equation is more conveniently expressed as the following variation problem: Find $p \in V(\Omega \cup \Omega_a)$ such that $p = 0$ on $\partial\Omega_a$ and it holds

$$\mathcal{A}(p, \varphi) = \mathcal{L}(\varphi), \quad (2.15)$$

for all $\varphi \in V(\Omega \cup \Omega_a)$ with $\varphi = 0$ on $\partial\Omega_a$. In the equation written above \mathcal{A} and \mathcal{L} denote the left and right hand sides of equation (2.14), respectively. This is the general form of the variational problem with \mathcal{A} and \mathcal{L} being the sesquilinear and linear functionals. Now, we approximate the infinite dimensional functional space V , with a n -dimensional space V_h and re-write (2.15) in terms of the basis functions (ψ 's) of this space. We obtain two equations from equating the real and imaginary parts as,

$$\sum_{j=1}^n \sum_{m=1}^n \mathcal{A}(\psi_j, \psi_l) \mu_j = \mathcal{L}(\psi_l) \quad \text{for } l = 1, 2, \dots, n. \quad (2.16)$$

Equation (2.16) is solved for the linear coefficients μ_i 's to obtain the approximate solution.



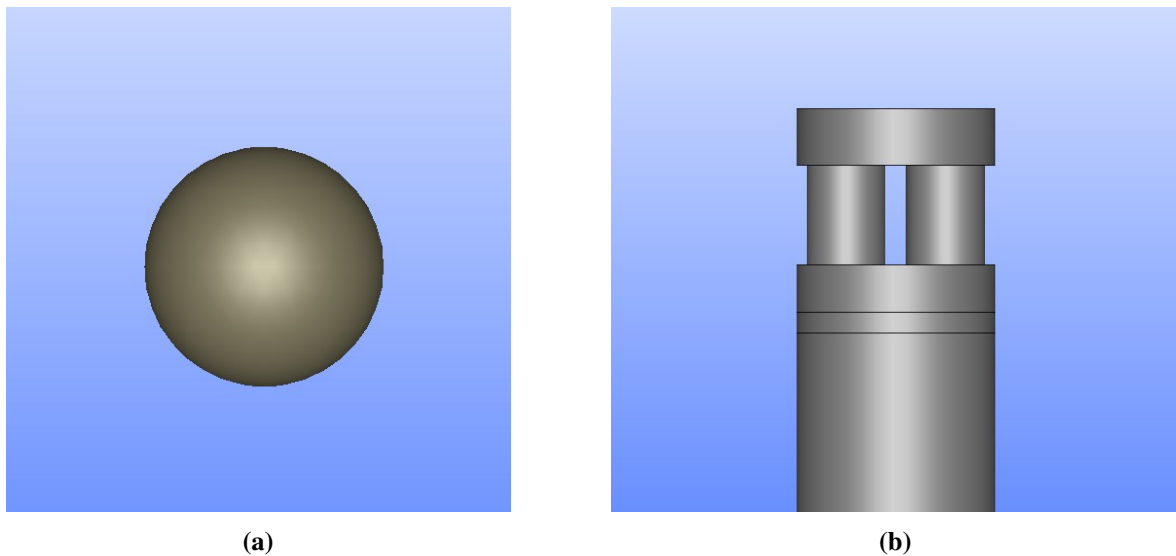


Figure 2.5: CAD models of (a) a sphere (b) simplified Microflow PU Probe. The models were created using SALOME.

2.4.2. Code implementation

2.4.2.1. CAD Model and Meshing

We start by modelling the geometry of the test subject so as to form a mesh representing the physical domain. This is achieved by using the modelling software, SALOME [22]. SALOME is an easy-to-use open-source CAD modelling and meshing software and offers interfaces to various simulation solvers. It also supports PYTHON scripts for modelling and meshing the subject geometry enabling dynamic changes if required.

A sphere of radius placed in air is utilized as our initial test subject to validate the code. The domain is modeled as a rectangle of sufficient width around it. The geometric dimensions of the PU probe are obtained from the partner company, Microflow Technologies and is utilized to make a CAD model for testing. The Microflow is initially considered in its simplified design which is considered to be sufficient for the preliminary study to compute gain of the probe. Both the models are shown modeled in SALOME in Figure 2.5. Since we are interested in solving the Helmholtz problem for the unbounded domain, we utilize the computational technique of replacing it with a truncated finite region around the probe and surround it with the PML as shown in Figure 2.7a. The geometry is then meshed using the NETGEN algorithms available in the SALOME's mesh module. Figure 2.6b and 2.7b shows the cross-section of the tetrahedral mesh color-coded to distinguish the PML layers. Each colored domain represents markers to indicate varying C and M in equation (2.12).

2.4.2.2. Finite Element Solver

Now that a mesh is constructed, we need a finite element solver to solve the equations (2.12) with boundary conditions (2.13) on this domain. The solver of choice is FEniCS [23], a popular open-source computing platform for solving partial differential equations (PDEs) using the finite element method. FEniCS offers containers and data-structures such as meshes, function spaces, finite-element assembly and mesh refinement and modules to generate finite element basis functions and expressing variational problems, to implement the solver in mathematical concepts which makes it easy to use. Moreover, it offers interfacing with various linear algebra solvers and data structures such as PETSc and supports programming in C++ and PYTHON[24].

PYTHON scripts are in development to solve the Helmholtz equation with the PML, developing over the codebase by Coral Real [25]. It utilizes the FEniCS libraries to assign boundary conditions, define Lagrange P1 basis functions at nodes, assemble the equations like (2.16) and finally solves them using the PETSc solver.



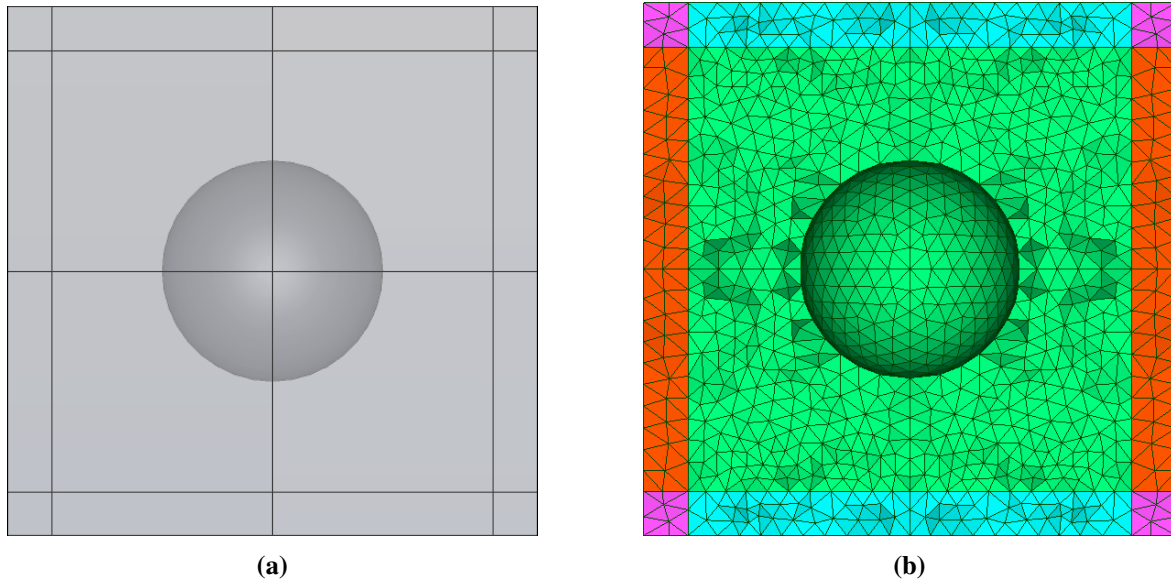


Figure 2.6: (a) CAD image of the PML around the sphere, and
(b) Cross-section of the tetrahedral mesh volumes

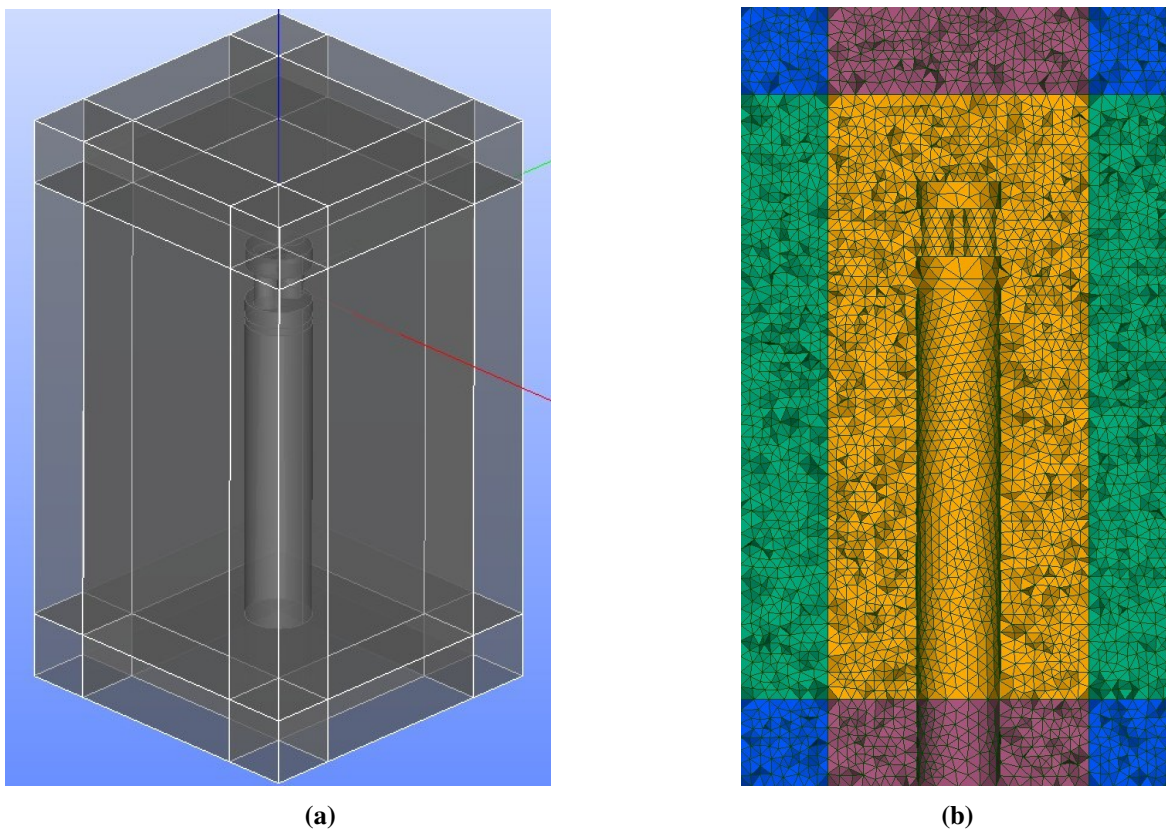


Figure 2.7: (a) CAD image of the PML around the probe geometry, and
(b) Cross-section of the tetrahedral mesh volumes

2.4.3. Results

2.4.3.1. Computing the PML absorption coefficients

The code is initially validated by considering a sphere in free-field conditions. By choosing the boundary conditions as a solution of a monopole source, an analytical solution is available to be compared. The value of the absorption function of the PML is optimized over a set of frequencies and spline interpolation is used to compute the values in between. Figure 2.8 shows the values of σ_0 obtained over a range of frequencies.

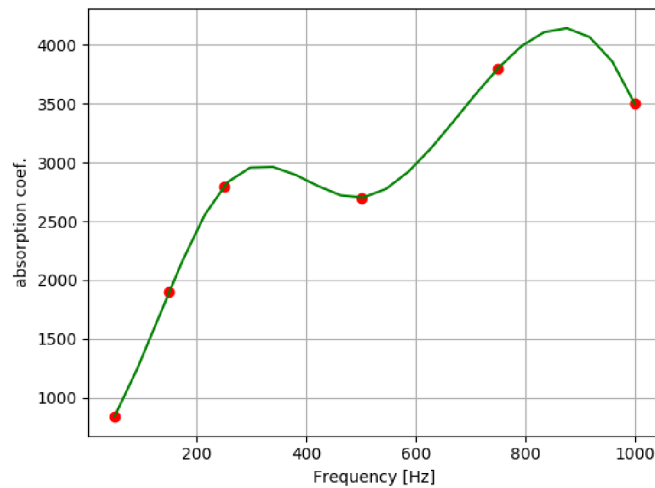


Figure 2.8: Values of PML absorption coefficient σ_0 for various frequencies

2.4.3.2. Validation

The pressure and velocity signals at the surface of sphere is then compared with the analytical solution to compute the accuracy of the implementation. Figure 2.9 shows the agreement of the analytical solution of the velocity field with the one computed by solving using the Finite Element method. The difference is mainly caused by numerical discretization and also due to the approximation with PML method. The results show good agreement with the analytical solution (within ± 2 dB) as shown in Fig 2.10. The solver is hence validated and can be utilized to study the gain of the pressure and velocity signals due to the sensor windscreen.

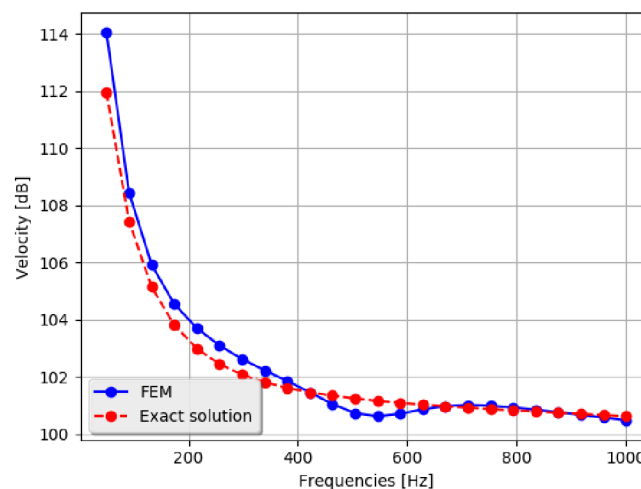


Figure 2.9: Validation of the code by comparing the velocity field at with the exact solution

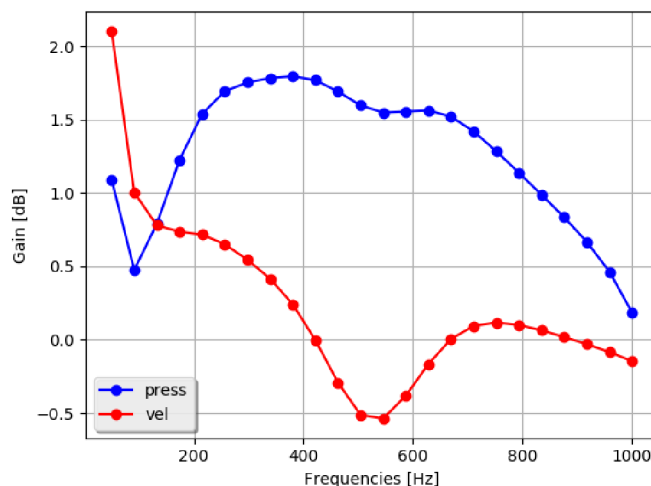


Figure 2.10: Gain in the pressure and particle velocity signals

2.5. Conclusion

In improving the sensitivity of the Microflown sensor, this project works towards exploring the use of porous material windscreen as windscreen rather than traditional rigid packaging. In this regard, it is necessary to measure the effect those windscreens can cause to an acoustic field. This project highlights the staggered development of a mathematical model to enable simulation of such effects. It highlights the various physics which needs to be coupled to obtain an accurate model. We suggest six stages to develop such a model and list six benchmark cases to validate the models at those stages with experiments. An initial study is performed on developing a mathematical model to study the loss of sensitivity due to the probe windscreen at no flow conditions. The solver to implement this model is in preliminary stages and the initial results show good agreement with analytical solution. Further development to the model, the solver and results will updated in future versions of the report.

Part III.

Benchmark cases in optimal transportation

Jean-David Benamou, Wilbert Ijzerman, Giorgi Rukhaia, INRIA

Keywords: Benchmark, freeform optics, optimal transport, reflector problem.

3.1. Context

FreeForm Optics [FFO] is the branch of Optics concerned with the design of non-conventional asymmetric refractive and reflective optical elements [OE] or systems of such elements. This research is important to improve the energy efficiency of lighting devices and reduce light pollution (for example of street lighting). A classic application of FFO (amongst many) is the irradiance tailoring problem: design an optical system transferring a given light source emittance (e.g a car headlight bulb) to a prescribed irregular target irradiance (e.g. the angular far field distribution of projected light). At the industrial level, FFO design has remained so far largely heuristic. On the academic side, two classes (collimated or point source illuminance) of idealized tailoring irradiance problems can be exactly modeled and solved using Optimal Transport [OT] theory. OT defines a unique map or a coupling between prescribed distributions representing given illuminance and irradiance. This map can then be used to construct the OE shape. Recent advances in OT numerical solvers allow to tackle systems described by millions of degrees of freedom. This offers a sound mathematical and numerical background to FFO.

3.2. Mathematical Model

3.2.1. PDE Model

One basic class of FFO problems can be described by a far field reflector model with a point source [26]. The model consists of a point source of light at the origin \mathcal{O} of \mathbf{R}^3 , a reflecting surface Γ which is a radial graph over $\Omega \subset \mathbf{S}^2$ in the northern hemisphere,

$$\Gamma = \{x\rho(x); x \in \Omega\} \quad \rho > 0 \quad (3.1)$$

and a target area which is far enough from reflector that reflected rays can be identified with their direction, i.e the domain $\Omega^* \subset \mathbf{S}^2$ represents reflected rays in terms of their reflection direction.

Assuming f is a density of light rays coming from \mathcal{O} , g a desired distribution in the domain Ω^* and that no energy is lost in the reflection, the conservation of energy gives the following constraint :

$$\int_{\Omega} f = \int_{\Omega^*} g \quad (3.2)$$

By the geometric reflection law, the direction of reflection of the ray coming from Ω to a point $z = x\rho(x)$ is calculated by

$$T(x) = T_{\rho}(x) = x - 2 \langle x, n \rangle n \quad (3.3)$$

where n is the outward normal of Γ at z . Again by the assumption of energy conservation, T is measure preserving, i.e

$$\int_{T^{-1}(E)} f = \int_E g \quad \forall \text{ Borel Set } E \subset \Omega^* \quad (3.4)$$

This relation leads to the following PDE description of the model, by noting that determinant of Jacobian of T



at x is equal to $f(x)/g(T(x))$:

$$\left(\frac{\rho^2 + |\nabla\rho|^2}{2\rho}\right)^2 \det\left(-\nabla_i\nabla_j\rho + 2\frac{\nabla_i\nabla_j\rho}{\rho} + \left(\frac{\rho^2 - |\nabla\rho|^2}{2\rho}\right)\delta_{ij}\right) = \frac{f(x)}{g(T(x))} \quad (3.5)$$

Together with a natural boundary condition:

$$T(\Omega) = \Omega^* \quad (3.6)$$

3.2.2. OT Model

Optimal Transport problem, first stated by Gaspard Monge, can be formulated in different ways and on different level of generality, but they all have following common concept behind it: Given a space X with a distribution on it μ (as a resource) and a space Y with a target distribution ν (desired allocation of resources), how to minimize the total cost of this allocation with respect to a given cost function $c(x, y)$ (the function giving the cost of transferring resources from a point $x \in X$ to $y \in Y$). There has been an abundant literature published about OT, especially during the last 20 years. This section relies mostly on [27] and [28].

Definition 1 (Monge Problem in \mathbf{R}^n). *Given two borel probability measures μ and ν , together with continuous cost function $c : \mathbf{R}^n \times \mathbf{R}^n \rightarrow \mathbf{R}$, problem is to find a map $T : \mathbf{R}^n \rightarrow \mathbf{R}^n$, which minimizes total transfer cost:*

$$C(\mu, \nu) = \min_T \int_{\mathbf{R}^n} c(x, T(x))d\mu \quad (3.7)$$

Here minimum is taken with respect to all measure preserving maps T , that is, for all measurable A , $\nu(A) = \mu(T^{-1}(A))$.

There are several examples when this problem doesn't have a solution, due to several geometrical and topological reasons, so the following relaxation was proposed by Kantorovich [REF?]

Definition 2 (Kantorovich Problem in \mathbf{R}^n). *Given two borel probability measures μ and ν , together with continuous cost function $c : \mathbf{R}^n \times \mathbf{R}^n \rightarrow \mathbf{R}$, find a measure γ on $\mathbf{R}^n \times \mathbf{R}^n$, which minimizes total transfer cost:*

$$C(\mu, \nu) = \min_{\gamma} \int_{\mathbf{R}^n \times \mathbf{R}^n} c(x, y)d\gamma \quad (3.8)$$

Here the minimum is taken with respect to all coupling measures γ , that is, the projections of γ on the first and second argument are respectively μ and ν , i.e. for all measurable A , $\gamma(A \times \mathbf{R}^n) = \mu(A)$ and $\gamma(\mathbf{R}^n \times A) = \nu(A)$.

It is now a well-known result in Optimal Transport theory that Kantorovich problem always has at least one solution, and when there exists a solution for Monge problem, there also exists a corresponding Kantorovich solution, and the minimal total cost is same. Moreover, the following theorem holds:

Theorem 1 (Kantorovich duality in \mathbf{R}^n). *Given two borel probability measures μ and ν , together with continuous cost function $c : \mathbf{R}^n \times \mathbf{R}^n \rightarrow \mathbf{R}$, such that $\int_{X \times Y} c(x, y)d\nu(x)d\mu(y) < \infty$ then following holds:*

$$C(\mu, \nu) := \min_{\gamma} \int_{\mathbf{R}^n \times \mathbf{R}^n} c(x, y)d\gamma = \max_{\phi, \psi} \left(\int_{\mathbf{R}^n} \phi(x)d\mu + \int_{\mathbf{R}^n} \psi(y)d\nu \right) \quad (3.9)$$

Where $\phi(x) + \psi(y) \leq c(x, y)$ are in $L^1(\mu)$ and $L^1(\nu)$ respectively.

In his paper [26], Wang proved that the model introduced in previous section, can be translated into optimal transport model, namely, he proved following theorem:



Theorem 2. *With the notation from previous section, suppose Ω and Ω^* are connected domains in northern and southern hemispheres respectively, f and g are densities of surface measures μ and ν , then there exists a maximizer (ϕ, ψ) of the dual Kantorovich problem with a cost function $c(x, y) = -\log(1 - \langle x, y \rangle)$. Moreover, this pair is unique up to a constant, and $\rho = e^\phi$ is a solution of (3.5).*

3.2.3. Geometrical Model

In the above model, solution is understood in a generalized sense, in terms of measure equality. That is, ρ is a generalized solution of (3.5) if $\int_E f dx = \int_{T_\rho(E)} g(x) dx$ where T_ρ is a set of points generating supporting paraboloids for ρ .

Definition 3. *For a function $p_y(x) = \frac{C}{1 - \langle x, y \rangle}$, $\Gamma_p = \{x p_y(x) | x \in \Omega\}$ is a paraboloid with focus at origin and axial direction y . Γ_p is a supporting paraboloid for ρ at a point x_0 if*

$$\rho(x_0) = p_y(x_0) \quad \text{and} \quad \rho(x) \leq p_y(x) \quad \forall x \in \Omega \quad (3.10)$$

Function ρ is called admissible if it has supporting paraboloid at each point of its graph. In this case one can define set valued mapping $T_\rho : \Omega \rightarrow \mathbf{S}^2$ with values being directions of supporting paraboloids at point x . Geometrically this means that $x\rho(x)$ can be approximated by paraboloids from above. Thereof one can see that admissible function should be semi-convex and twice differentiable almost everywhere. This implies that T_ρ is single valued almost everywhere, which means that $\int_{T_\rho(E)} g(x) dx$ is well defined. In fact it is a radon measure, as proven in [26] and references therein.

Definition 4. *An admissible function ρ is a generalized solution of (3.5) if*

$$\int_E f dx = \int_{T_\rho(E)} g(x) dx \quad (3.11)$$

If ρ also satisfies

$$\Omega^* \subset T_\rho(\Omega) \quad \text{and} \quad |\{x \in \Omega | f(x) > 0 \text{ and } T_\rho(x) - \bar{\Omega}^* = \emptyset\}| = 0 \quad (3.12)$$

Then ρ is a generalized solution of (3.5), (3.6).

For more details about generalized solutions and supporting paraboloids, see [26](section 2).

3.3. Numerical Models

There are several different approaches for finding numerical solution of Optimal Transport problems, varying in efficiency, accuracy and complexity. A general reference for this section would be [27] and [29].

3.3.1. Kantorovich's Linear Program

Kantorovich's linear program is one of the most basic tools for solving Optimal Transport problems. In this approach, measures are approximated by point clouds, that is, weighted sums of Dirac masses inside the support of original measure.

$$\mu = \sum_{i=1}^N p_i \delta_{x_i}, \quad \nu = \sum_{j=1}^M q_j \delta_{y_j}, \quad \text{where} \quad \sum_{i=1}^N p_i = \sum_{j=1}^M q_j = 1 \quad (3.13)$$

This discretisation allows one to define an approximating optimal cost in the following way:



$$L_c(p, q) = \min_{\gamma \in \Pi(p, q)} \sum_{i=1}^N \sum_{j=1}^M C_{ij} \gamma_{ij} \quad (3.14)$$

$$\Pi(p, q) = \left\{ \gamma \in \mathbf{R}_+^{N \times M} \mid \gamma \mathbf{1}_N = p, \gamma^\top \mathbf{1}_M = q \right\} \quad (3.15)$$

Where C is a matrix with $C_{ij} = c(x_i, y_j)$ and $\mathbf{1}_n$ denotes n -dimensional vector of ones. This formulation can now be rewritten into standard Linear programming form:

$$L_c(p, q) = \min_{\hat{P} \in \mathbf{R}^{NM}} \hat{C}^\top \hat{P} \quad (3.16)$$

$$A \hat{P} = \begin{bmatrix} p \\ q \end{bmatrix} \quad (3.17)$$

$$A := \begin{bmatrix} \mathbf{1}_N^\top \otimes \mathbb{I}_M \\ \mathbb{I}_N \otimes \mathbf{1}_M^\top \end{bmatrix} \quad (3.18)$$

Where \hat{C} and \hat{P} are vectors consisting of stacked columns of C and P respectively, \otimes denotes Kronecker's product and \mathbb{I}_n is n -dimensional identity matrix.

The main drawback of this method is its high dimensionality. Even for moderate N and M , one needs to solve problem in thousands of dimensions. But on the other hand, its simple structure and well known nature of Linear Programming allows one to get important theoretical regularity results.

3.3.2. Monge-Ampère Based methods

There are two classes of Monge-Ampère Methods. In the semidiscrete approach, the source density is treated as continuous, while destination density is taken to be finitely atomic. Using the special structure of the solution, one can reformulate problem in a way which allows usage of some effective methods from computational geometry. For the details and application the the reflector problem see [30]. The equation (3.5) can also be approximated, see [31].

3.3.3. Entropic regularization

Entropic regularisation approach uses same discretisation scheme as is subsection 3.1, but instead of (3.14), it minimizes following:

$$L_c^\epsilon(p, q) = \min_{\gamma \in \Pi(p, q)} \sum_{i=1}^N \sum_{j=1}^M C_{ij} \gamma_{ij} - \epsilon H(\gamma) \quad (3.19)$$

Where $H(\gamma)$ is the discrete Boltzmann entropy of a coupling matrix:

$$H(\gamma) = - \sum_{i=1}^N \sum_{j=1}^M \gamma_{ij} (\log \gamma_{ij} - 1) \quad (3.20)$$

The cost function (3.19) has several advantages. First of all, it is strongly convex, thereof it has unique minimizer. Also, this minimizer has full support, comparing to the solution of original problem (3.14), which is typically sparse. Secondly this leads to a more efficient algorithms for finding a solution.

Of course this approach is justified by the following convergence result. [27]:

Theorem 3. *The solution γ^ϵ of (3.19) converges to a solution of (3.14) with minimal entropy. That is,*

$$\gamma^\epsilon \rightarrow \operatorname{argmin} \{ -H(\gamma) \mid \gamma \text{ solves (3.14)} \} \quad (3.21)$$



3.4. Numerical algorithm and Benchmark Case

For the Benchmark case we implement Sinkhorn's algorithm for the reflector problem, which is working with Entropic regularization method.

3.4.1. Sinkhorn algorithm

In order to derive an algorithm for finding a solution to the regularized problem (3.19), it's useful to note that solution has very specific structure. In particular, following theorem holds(see for example [29] [27]):

Theorem 4. *Solution of regularized problem (3.19) has following structure: $\gamma_{ij}^\epsilon = u_i K_{ij} v_j$ where $K_{ij} = e^{-C_{ij}/\epsilon}$.*

This structure allows one to use Sinkhorn's algorithm, which is designed to transform given matrix K into a matrix with above-mentioned structure, such that it's marginals are prescribed vectors. In particular, given matrix K and vectors p, q , set

$$u^{l+1} = \frac{p}{K v^l} \quad v^{l+1} = \frac{q}{K^T u^{l+1}} \quad (3.22)$$

with $v^0 = \mathbb{1}_M$ and division understood componentwise.

Theorem 5. *For a given matrix K and vectors p, q , above-mentioned iterative procedure converges to vectors u, v , such that matrix γ defined by $\gamma_{ij} = u_i K_{ij} v_j$ has property $\gamma \mathbb{1}_N = p$, $\gamma^T \mathbb{1}_M = q$*

To sum up, sinkhorn's algorithm with regularization parameter $\epsilon = \frac{1}{k}$ for reflector problem described in the first section, works in the following way.

Given discretizations of source and target as given in **Subsection 3.1**:

$$\mu = \sum_{i=1}^N p_i \delta_{x_i}, \quad \nu = \sum_{j=1}^M q_j \delta_{y_j}, \quad \text{where} \quad \sum_{i=1}^N p_i = \sum_{j=1}^M q_j = 1 \quad (3.23)$$

Matrix K is defined by reflector cost from **Theorem 2**, i.e:

$$K_{ij} = e^{-k(-\log(1 - \langle x_i, y_j \rangle))} = (1 - \langle x_i, y_j \rangle)^k \quad (3.24)$$

And the sinkhorn sequences have following form:

$$u_i^{l+1} = \frac{p_i}{\sum_{j=1}^M (1 - \langle x_i, y_j \rangle)^k v_j} \quad v_j^{l+1} = \frac{q_j}{\sum_{i=1}^N (1 - \langle x_i, y_j \rangle)^k u_i} \quad (3.25)$$

Finally, approximation of solution of (3.5) will have a form $\rho_\epsilon(x_i) = u_i$, where u is the limit of u^l .

3.4.2. First Benchmark Case

First proposed benchmark case to validate the numerical method is to compute the reflector shape mapping a uniform density from a square projected to the sphere (by normalizing each point to norm 1) to two different points on the opposite side, using entropic regularization and some of extra techniques mentioned in [32]. In particular, the regularization parameter is chosen to be $\frac{1}{\sqrt{N}}$ where N is number of points in the discretisation of source.

Here follows computational results and corresponding errors in two different discretizations, one with standart square grid and another with quasi Monte-Carlo grid as proposed in [32] and computed in [33].

In particular, standard grid for the source is created by putting a square with side 1.4 on the plane $z' = 1$, centered at $(0, 0, 1)$, discretizing it uniformly with a step size $\frac{1}{\sqrt{N}}$ and then projecting those points to a sphere



by standard normalization $\left(\frac{x'}{\|x'\|}, \frac{y'}{\|x'\|}, \frac{z'}{\|x'\|}\right)$. At the end one receives the discretization on the sphere where for each point, $-0.5 < x' < 0.5$ and $-0.5 < y' < 0.5$. For the destination, the source grid is reflected with respect to the xy plane and then two opposite vertex of the square are chosen to have a positive mass of $\frac{1}{2}$.

Quasi Monte-Carlo grid is taken from <http://web.maths.unsw.edu.au/rsw/Sphere/EffSphDes/> with total amount of points on the sphere being 52978. Then for source density the points with $-0.5 < x' < 0.5$, $-0.5 < y' < 0.5$, $z' > 0$ are chosen. For destination, again source density is reflected with respect to xy plane and two points closest to the opposite vertex of the square are chosen to have a positive mass of $\frac{1}{2}$.

All computations are done for similar amount of points (4624 for Standart, 4648 for Monte-Carlo) with a cost function $c(x, y) = -\log(1 - \langle x, y \rangle)$ from **Theorem2**, and Sinkhorn algorithm implemented as described in **Subsection4.1**

The number of iterations(NI) represents the amount of iterations it took algorithm to achieve machine precision stationarity of the sequence u , that is, $\max_i |\log \frac{u_i^{l+1}}{u_i^l}| < 10^{-13}$, and the error is a maximal difference computed with respect to the theoretical solution of the problem, which is known to be union of two paraboloids.

More precisely, according to [26], the paraboloid which reflects light from the center in the direction of vector y_i , has a shape $x\rho(x)$ where $\rho(x) = \frac{v_i}{1 - \langle x, y_i \rangle}$. Therefore desired values for u_i would be $\min(\rho_1(x_i), \rho_2(x_i))$, where $x\rho_1(x)$ and $x\rho_2(x)$ are paraboloids reflecting light in the direction of respective points in destination density. Thereof $ME = \max_i \{u_i - \min(\rho_1(x_i), \rho_2(x_i))\}$ where y_1 and y_2 are points with positive mass concentration in the destination density. Relative error is computed with respect to the magnitude of u_i , that is, $RelativeError = \max_i \left\{ \frac{u_i - \min(\rho_1(x_i), \rho_2(x_i))}{u_i} \right\}$

Regularization parameter $\epsilon = \frac{1}{k}$ with $k = \sqrt{N} = 68$			
	NI	Maximal Error	Relative Error
Monte-Carlo Grid	248	2.386739892415740138532e-01	6.024078476566734322392e-01
Standart Grid	366	2.346179628934388361472e-01	5.921705272423998893165e-01

This case loosely corresponds to the theoretical predictions made in [32]. In particular, it was predicted that when regularization is taken to be of order $N^{\frac{1}{2}}$ and grid is taken as in [33], number of iterations should be of order $k \log(k)$ (in the above case 287), and error should be of order $k^{-1} \log(k)$ (in this case 0.06) ([32], Theorem 5.4)

Problem with the above case is that since the regularization parameter is small, the regularized problem is still not close enough to the original. To fix this and get a better approximation with the same amount of points, one could decrease the regularization parameter in a way that still would be in the margins of theoretical requirement. In the following chart there is a result for the same simulation running but with inverse regularization parameter $k = 4\sqrt{N} = 272$. In this case the theoretical bounds would be 1524 iterations and error of order 0.02.

Regularization parameter $\epsilon = \frac{1}{k}$ with $k = 4\sqrt{N} = 272$			
	NI	Maximal Error	Relative Error
Monte-Carlo Grid	791	6.194511359457566257447e-02	1.738542194339866703780e-01
Standart Grid	1385	6.888104173974551880377e-02	1.563480908495094966543e-01

3.4.3. Second Benchmark Case

Second benchmark case is computing "Identity", that is, solving problem where source and destination densities are same, in this case two copies of square projected on a sphere. Both standard and Monte-Carlo discretization and square grid selection is done as in previous case, except for initial sequence. For this case, one needs to alter initial sequence in Sinkhorn algorithm, as (3.22) initialized with $v^0 = \mathbb{1}$ would converge in one step since it is an exact solution. Thereof in this benchmark case $v_i^0 = \|x_i\|_1$ is used as initializing sequence.

Exact solution of this problem is a spherical mirror, meaning that ρ should be constant. In the following tables, Mean value of ρ is naturally arithmetical mean of all values of u_i , $mean = \sum_{i=1}^N \frac{u_i}{N}$. Mean deviation is



$\sum_{i=1}^N \frac{u_i - \text{mean}}{N}$, maximal deviation is $\max_i (u_i - \text{mean})$.

Relative values are corresponding quantities divided by mean value, i.e mean relative deviation is $\sum_{i=1}^N \frac{u_i - \text{mean}}{N * \text{mean}}$ and mean maximal deviation is $\max_i \frac{u_i - \text{mean}}{\text{mean}}$.

Regularization parameter $\epsilon = \frac{1}{k}$ with $k = \sqrt{N} = 68$		
	Standart Grid	Monte-Carlo Grid
Number of Points	4624	4648
Number of Iterations	124	77
Mean value of ρ	2.541496323168340176757e-01	2.580267658539918129712e-01
Mean deviation	9.975802192232223388618e-04	5.824680299182465308822e-04
Maximal deviation	4.088719817606722983783e-03	3.424578184603344066517e-03
Mean relative deviation	3.925168846908247237415e-03	2.257393832730688557758e-03
Maximal relative deviation	1.608784470917332121154e-02	1.327218195084920414339e-02

Again, as in previous case, results can be improved by changing regularization parameter.

Regularization parameter $\epsilon = \frac{1}{k}$ with $k = 4\sqrt{N} = 272$		
	Standart Grid	Monte-Carlo Grid
Number of Points	4624	4648
Number of Iterations	467	282
Mean value of ρ	2.965009642876027529113e-01	3.003773288592066492697e-01
Mean deviation	1.100551519579807090154e-03	1.205026718470789798797e-04
Maximal deviation	3.140404297011623047098e-03	1.041507318220002975551e-03
Mean relative deviation	3.711797437907432724302e-03	4.011709948441587766758e-04
Maximal relative deviation	1.059154834304506555276e-02	3.467329981844868326546e-03



Part IV.

Data driven model adaptations of coil sensitivities in magnetic particle imaging

Lena Hauberg-Lotte, Peter Maass

Abstract

In the first chapter we introduce the basic ideas of magnetic particle imaging (MPI), inverse problems and Deep Learning. In the second chapter we focus on the details of the modeling of the forward operator of MPI, specially we introduce the equilibrium model and outline more complex models. After that we discuss different scenarios of model and data accuracies to lay the groundwork for the following discussion of which Deep Learning approaches to inverse problems could be used for which scenarios. We make the five broad categorizations of Deep Learning approaches to inverse problems: 1. Learned Penalty Terms, 2. Plug-and-Play Prior Methods, 3. Gradient-Descent-by-Gradient-Descent type Methods, 4. Regularization by Architecture (Deep Prior), 5. Image Post-Processing via Deep Learning.

Keywords: Deep learning, neural networks, inverse problems.

4.1. Introduction and literature

4.1.1. Magnetic Particle Imaging

Magnetic particle imaging (MPI) is a relatively new non-invasive tomographic imaging technique that directly detects superparamagnetic iron oxide nanoparticles (SPIO). It combines high tracer sensitivity with submillimetre resolution and imaging is performed in milliseconds to seconds.

MPI is suitable for several medical applications: The nonlinear magnetization behaviour of nanoparticles in an applied magnetic field is employed to reconstruct a spatial distribution of the concentration of nanoparticles in the cardiovascular system. A high temporal resolution and a potentially high spatial resolution make MPI suitable for several *in-vivo* applications without the need for harmful radiation. The potential for imaging blood flow was demonstrated first in *in-vivo* experiments using a healthy mouse [34]. The usability of a circulating tracer for long-term monitoring was recently investigated [35]. The high temporal resolution of MPI is advantageous for potential flow estimation [36] and for tracking medical instruments [37]. Recently, MPI was also shown to be suitable for tracking and guiding instruments for angioplasty [38]. Further promising applications of MPI include cancer detection [39] and cancer treatment by hyperthermia [40].

The main goal of MPI is to reconstruct the spatially dependent concentration of particles and for that computationally efficient reconstruction methods are required to allow real time observations. Therefore mathematical models are advantageous for the development of such new methods.

4.1.2. Deep Learning and Inverse Problems

Inverse Problems have been a key tool in many areas of science, technology in general, and more particularly in the field of medical imaging for many years now. The key idea is to calculate causes from effects, opposed to so-called direct problems trying to predict effects from causes.

Deep Learning (DL) on the other hand is a relatively new field which studies big machine learning models. It is not clear what all the strength of DL are, but a major one is the ability to predict labels from data via



supervised learning, e.g., a label of a computer tomographic (CT) image could be cancer or no cancer. A major problem with this is the fact that one usually needs massive amounts of labeled data to train a learning model.

The success of neural networks (NN) in many computer vision tasks in the past has motivated attempts at using Deep Learning to achieve better performance in solving Inverse Problems [41]. It was proposed to apply data-driven approaches to inverse problems, using neural networks as a regularization functional. The network learns to discriminate between the distribution of ground truth images and the distribution of unregularized reconstructions and the approach was used for computer tomography reconstruction [42]. Furthermore, deep learning was used in medical applications such as tumour classification with MALDI Imaging [43], magnetic resonance imaging (MRI) [44] [45], low-dose X-ray CT [46] as well as positron emission tomography (PET) [47].

The need for massive amounts of data is also a major challenge in bringing Deep Learning and Inverse Problems together, since it creates a chicken-and-egg-problem. The problem lies therein that one can think about the "cause" in Inverse Problems as (or at least connected to) the label in Deep Learning. This means that one usually doesn't have labels for Inverse Problems which are required to train a deep model to solve the Inverse Problem. Most approaches that try to bring Deep Learning to Inverse Problems ignore this fact and only focus on problems where there is enough ground truth data for the cause already – due to some special circumstances. In fact they can simplify the practical application of already solved Inverse Problems massively, but they can usually not be applied to novel unsolved Inverse Problems. In summary: there exists some kind of "information gap" that creates a boot strap problem. We are planning on exploring ways to solve this problem, in particular for MPI.

4.2. Mathematical description

4.2.1. Magnetic Particle Imaging

To determine the distribution of nanoparticles, which is the quantity $c(x)$, the nonlinear magnetization behavior of ferromagnetic nanoparticles is exploited as follows, see also [48]: A static magnetic field (selection field), which is given by a gradient field, generates a field free point (FFP) (or alternatively a field free line (FFL) [49]). The larger the distance between nanoparticles and FFP, the more is the magnetization caused by the nanoparticles in saturation. The superposition with a spatially homogeneous but time-dependent field (drive field) moves the field free region along a predefined trajectory defining the field-of-view (FOV). An interplay between gradient strength and drive field amplitude determines the FOV size but when guaranteeing a certain resolution the FOV is strictly limited due to safety reasons. The rapid change of the applied field $\mathbf{H}(x, t)$ causes a measurable change of the magnetization $\mathbf{M}(x, t)$ of the nanoparticles.

In the first approximation the change of the magnetization can be characterized by using the Langevin function. Neglecting the interactions between multiple particles and doing the transition from microscopic to macroscopic scale (see [50]) allows the approximation of the magnetization \mathbf{M} by multiplying the particles' mean magnetic moment vector $\bar{\mathbf{m}}(x, t)$ and the particle concentration $c(x)$.

The temporal change of the particles' magnetization induces a voltage $u^P(t)$ in the receive coil units. Using a quasi-static approximation in the induction principle and the law of reciprocity (see [51]) allows for the description via a linear integral operator with respect to the particle concentration:

$$u^P(t) = -\mu_0 \int_{\Omega} \mathbf{p}^R(x) \cdot \frac{\partial}{\partial t} \mathbf{M}(x, t) dx = \int_{\Omega} c(x) \underbrace{(-\mu_0 \mathbf{p}^R(x) \cdot \frac{\partial}{\partial t} \bar{\mathbf{m}}(x, t))}_{=s(x,t)} dx. \quad (4.1)$$

Here, \mathbf{p}^R is the receive coil sensitivity, which is the magnetic field which is generated by the receive coil unit



when applying a unit current. Analogously, the applied field $\mathbf{H}(x, t)$ also induces a voltage $u^E(t)$ which is known as direct feedthrough. Since this value is several orders of magnitude larger than that of the particle signal, it must be removed prior to digitization. This is done by applying an analog filter which is described by a temporal convolution with a kernel function $a(t)$ (\tilde{a} denotes its periodic continuation). The measured signal $v(t)$ is then given by $v = (u^P + u^E) * a$. One common choice for the analog filter is a band-stop filter such that some frequency bands of the particle signal are also removed. The resulting integral kernel $\tilde{s}(x, t) = (s(x, \cdot) * a)(t)$ is primarily determined by the analog filter (receive-unit-dependent), the receive coil sensitivity (receive-unit-dependent), the behavior of the nanoparticles, the particle parameters, and the applied magnetic fields. Due to missing accurate models for the particle magnetization, the whole function \tilde{s} is commonly determined in a time-consuming calibration process limiting the FOV size as well as the resolution. As the calibration data strictly relies on the particle properties and the measurement sequence, changing tracer material or measurement sequences requires a complete recalibration. Model-based approaches including less simplified behavior of the particles' magnetic moments in the applied fields are highly desirable to reduce the calibration costs and to enable more sophisticated measurement sequences.

4.2.1.1. Scenarios in MPI

The main problem in MPI is given by the forward operator

$$F : X(\Omega) \rightarrow Y(0, T)^L$$

$$c \mapsto (A_k c + a_k * u_k^E)_{k=1, \dots, L},$$

for $L \in \mathbb{N}$ receive coil units with suitable function spaces $X(\Omega)$ and $Y(0, T)$ (assumed to be Hilbert spaces in the following). $A_k : X(\Omega) \rightarrow Y(0, T)$, $c \mapsto \int_{\Omega} \tilde{s}_k(x, t) c(x) dx$, $k = 1, \dots, L$, is the forward operator mapping to the analog filtered particle signal for individual receive coil units. The operator F describes the actual measurement process. In MPI we are mainly aiming for solving problems given by the linear operator

$$A : X(\Omega) \rightarrow Y(0, T)^L$$

$$c \mapsto (A_k c)_{k=1, \dots, L}.$$

We thus need to get rid of the direct feedthrough u_k^E . In an ideal situation it holds $A = F$ as one assumes $a_k * u_k^E = 0$ but in general this not the case. We can now distinguish two cases in MPI regarding a formal description of the forward operator, the *data-based* case where a full calibration of the linear forward operator is performed and the *model-based* case where a suitable model for the mean magnetic moment $\bar{\mathbf{m}}$ is formulated. Due to the fact that finding a suitable model for the particles' magnetization is still an unsolved problem and the full system matrix calibration is still state of the art in MPI, we distinguish these two cases in the following. As it is possible to specify physical models which might not include relevant aspects, hybrid approaches combining best of both are also desirable. In MPI possible problem setups are as follows (to improve reading convenience, we formulate the scenarios for one coil unit only, i.e., $L = 1$):

- *Data-based* case: Let $\Gamma \subset \mathbb{R}^3$ be a reference volume placed at the origin. The data-based approach uses single measurements of a small sample at predefined positions $\{x^{(i)}\}_{i=1, \dots, N} \in \Omega^N$. The concentration phantoms are given by $c^{(i)} = c_0 \chi_{x^{(i)} + \Gamma}$ for some reference concentration $c_0 > 0$. Typical choices for Γ are small cubes ($\sim 1 \text{ mm} \times 1 \text{ mm} \times 1 \text{ mm}$). The measurements $v^{(i)} = \frac{1}{c_0} F c^{(i)}$, $i = 1, \dots, N$, are then used to characterize the data-based forward operator.

Background subtraction case (D1): Let $v^{(0)} = F0$. Assuming the calibration positions are chosen such that $x^{(i)} + \Gamma$ are pairwise disjoint and $\Omega = \cup_{i=1}^N x^{(i)} + \Gamma$, the specific discretised problem of the model-based approach corresponds to the data-based approach (solving $Ac = v - v^{(0)}$) with $S\tilde{c} = v - v^{(0)}$ with $S = [v^{(1)} - v^{(0)} | \dots | v^{(N)} - v^{(0)}]$ and where $c = \sum_{i=1}^N \tilde{c}_i \chi_{x^{(i)} + \Gamma}$. The full discrete setup is obtained by a finite dimensional approximation in $Y_M \subset Y(0, T)$, i.e., assume $v = \sum_{i=1}^M \langle \phi_i, v \rangle \phi_i$ where $\{\phi_j\}_{j \in \mathbb{N}}$



is an ONB of $Y(0, T)$. It then reads: Find $\tilde{c} \in \mathbb{R}^N$ for given measurement $\tilde{v} \in \mathbb{K}^M$, $\mathbb{K} \in \{\mathbb{R}, \mathbb{C}\}$, ($v \in Y(0, T)$ obtained from an evaluation of F) such that

$$\tilde{S}_{D1}\tilde{c} = \tilde{v} - \tilde{v}^{(0)}, \quad \tilde{S}_{D1} = [\tilde{v}^{(1)} - \tilde{v}^{(0)} | \dots | \tilde{v}^{(N)} - \tilde{v}^{(0)}] \quad (4.2)$$

where $\tilde{v} = (\langle \phi_i, v \rangle)_{i=1, \dots, M}$ ($\tilde{v}^{(k)}$ obtained analogously).

Partial temporal information case (D2): Alternative strategies to remove the influence of the background signal $v^{(0)}$ (due to the structure of $v^{(0)}$ in a certain basis) is to restrict the problem to partial data. The discretisation of $Y(0, T)$ is again obtained via the ONB $\{\phi_i\}_{i=1, \dots, M}$. Let $\{\psi_j\}_{j \in \mathbb{N}}$ be another ONB of $Y(0, T)$ (can also be equal to $\{\phi_i\}_{i=1, \dots, M}$). We further assume $v^{(0)}$ is sparse in $\{\psi_j\}_{j \in \mathbb{N}}$, i.e. $|\langle v^{(0)}, \psi_j \rangle| \neq 0$, $j \in J$, $|J| < \infty$. We thus formulate the reduced data problem within the data-based case: It then reads finding $\tilde{c} \in \mathbb{R}^N$ for given measurement $\tilde{v} \in \mathbb{K}^M$, $\mathbb{K} \in \{\mathbb{R}, \mathbb{C}\}$, ($v \in Y(0, T)$ obtained from an evaluation of F) such that

$$\langle S\tilde{c}, \psi_j \rangle = \langle v - v^{(0)}, \psi_j \rangle, \quad j \in \mathbb{N} \setminus J, \quad S = [v^{(1)} - v^{(0)} | \dots | v^{(N)} - v^{(0)}] \quad (4.3)$$

Exploiting the sparsity assumption on $v^{(0)}$ and using the finite-dimensional approximation in Y_M yields the final problem

$$\begin{aligned} \langle \tilde{S}_{D2}\tilde{c}, (\langle \phi_i, \psi_j \rangle)_{i=1, \dots, M} \rangle &= \langle \tilde{v}, (\langle \phi_i, \psi_j \rangle)_{i=1, \dots, M} \rangle, \quad j \in \mathbb{N} \setminus J, \\ \tilde{S}_{D2} &= [\tilde{v}^{(1)} | \dots | \tilde{v}^{(N)}] \end{aligned} \quad (4.4)$$

The crucial part is to obtain the correct index set J . In the literature this is commonly done by an SNR-threshold technique with respect to $\{\psi_j\}_{j \in \mathbb{N}}$ being the Fourier basis for T -periodic signals. If the index set is determined incorrectly, one inverts an affine linear system assuming it is linear causing additional artifacts in the reconstruction (i.e., in a noise-free case the reconstruction c^* of a true c^\dagger is obtained via $c^* = A^{-1}Fc^\dagger = c^\dagger + A^{-1}v^{(0)}$).

- *Model-based case:* The challenging part in the model-based case is formulating the correct model for the mean magnetic moment $\bar{\mathbf{m}}$.

Equilibrium model (monodisperse / polydisperse) (M1): One of the most extensively studied models in MPI is based on the Langevin function. This model is motivated by the assumptions that the applied magnetic field is static and the particles are in equilibrium. Under these assumptions, we assume that the mean magnetic moment vector of the nanoparticles immediately follows the magnetic field, i.e.:

$$\bar{\mathbf{m}}(x, t) = m_0 \mathcal{L}_\beta(|\mathbf{H}(x, t)|) \frac{\mathbf{H}(x, t)}{|\mathbf{H}(x, t)|} \quad (4.5)$$

where $\mathcal{L}_\beta : \mathbb{R} \rightarrow \mathbb{R}$ is given in terms of the Langevin function by the following:

$$\mathcal{L}_\beta(z) = \left(\coth(\beta z) - \frac{1}{\beta z} \right) \quad (4.6)$$

for $m_0, \beta > 0$. The final problem with respect to the Langevin function is to obtain the concentration c from the following system of equations:

$$\begin{cases} v(t) = - \int_0^T \int_\Omega c(x) \tilde{a}_k(t-t') s_k(x, t') dx dt' \\ s = \mu_0 m_0 (\mathbf{p}^R)^T \frac{\partial}{\partial t} \left(\mathcal{L}_\beta(|\mathbf{H}|) \frac{\mathbf{H}}{|\mathbf{H}|} \right) \end{cases} \quad (4.7)$$



$I_3 \in \mathbb{R}^{3 \times 3}$ being the identity matrix. The *equilibrium model* in (4.7) can be extended to polydisperse tracers by adapting the function defining the length of the mean magnetic moment vector in (4.6). The tracer material is then modeled by a distribution of particles with different diameters $D > 0$. Assuming that the particle's diameter distribution is given by the density function $\rho : \mathbb{R}^+ \rightarrow \mathbb{R}^+ \cup \{0\}$ with $\|\rho\|_{L^1(\mathbb{R}^+)} = 1$, we obtain the extended problems by the following:

$$\begin{cases} v(t) = - \int_0^T \int_{\Omega} c(x) \tilde{a}(t-t') s(x, t') dx dt' \\ s = \mu_0 (\mathbf{p}^R)^T \frac{\partial}{\partial t} \left(L_{\rho}(|\mathbf{H}|) \frac{\mathbf{H}}{|\mathbf{H}|} \right) \end{cases} \quad (4.8)$$

where $L_{\rho} : \mathbb{R} \rightarrow \mathbb{R}$ is given in terms of the Langevin function by

$$L_{\rho}(z) = \int_{\mathbb{R}^+} \rho(D) m_0(D) \mathcal{L}_{\beta(D)}(z) dD \quad (4.9)$$

with $m_0, \beta : \mathbb{R}^+ \rightarrow \mathbb{R}^+$ describing the influence of the particle diameter on the volume of the core, respectively the magnetic moment.

Imperfect models suitable for lower quality image reconstruction (M2): This category includes a rather large number of possible model approaches. Generally spoken, this comprises models which approximate the behavior of the system matrix (commonly fitting some model parameters to real data) but cannot reach the reconstruction quality of the data-based case. For example, one can treat the analog filter a as one unknown parameter and fit the model in (M1) to real data.

Suitable model for magnetization dynamics (M3): The operator is properly described by a mathematical model including a sufficient model for the magnetization behavior of the tracer. This requires considering (or approximating) Brownian and Néel rotation mechanisms in the magnetic moment rotation of the nanoparticles. The important difference to (M2) is that here we assume that this model is qualitatively an alternative to the data-based case. This is still an unsolved problem but it is added to the list of possible cases to emphasize the opportunities in the context of Deep Learning approaches.

Using the previously formulated standard setups in MPI we can formulate different problem scenarios (S) which are discussed in the context of Deep Learning in the remainder of this article:

- **Scenario (S1):**
Given information (D1): measured and background-corrected system matrix (\tilde{S}_{D1}), background measurements $\tilde{v}^{(0)}$, a phantom measurement \tilde{v} .
Possible targets: (i) reduce number of calibration scans (larger delta sample and/or missing regions), (ii) obtain fast and improved concentration reconstructions, (iii) obtain memory-efficient representation, (iv) obtain cleaned particle signal
- **Scenario (S2):**
Given information (D2): measured system matrix (\tilde{S}_{D2}), background measurements $\tilde{v}^{(0)}$ (optional), a phantom measurement \tilde{v} .
Possible targets: (i) reduce number of calibration scans (larger delta sample and/or missing regions), (ii) obtain fast and improved concentration reconstructions, (iii) obtain memory-efficient representation, (iv) obtain correct index set J , (iv) obtain completed particle signal
- **Scenario (S3):**
Given information (D1 or D2, M1): measured system matrix (\tilde{S}_{D1} or \tilde{S}_{D2}), background measurements $\tilde{v}^{(0)}$ (in (D2) optional), a phantom measurement \tilde{v} , similar but oversimplified model for $\tilde{\mathbf{m}}$ (see M1).
Possible targets: (i) reduce number of calibration scans (larger delta sample and/or missing regions), (ii) obtain fast and improved concentration reconstructions, (iii) obtain memory-efficient representation, (iv)



obtain correct index set J (in (D2)), (iv) obtain completed particle signal, (v) measured signal correction (background), completion, and mapping to range of oversimplified model (reconstruction is than obtained via oversimplified model).

- **Scenario (S4):**

Given information (M1): background measurements $\tilde{v}^{(0)}$, a phantom measurement \tilde{v} , similar but oversimplified model for $\bar{\mathbf{m}}$ (see M1).

Possible targets: (i) obtain fast and improved concentration reconstructions, (ii) obtain improved operator, (iii) obtain cleaned particle signal from measured phantom data.

- **Scenario (S5):**

Given information (M2): background measurements $\tilde{v}^{(0)}$, a phantom measurement \tilde{v} , imperfect model for $\bar{\mathbf{m}}$ which allows reasonable reconstruction (see M2).

Possible targets: (i) obtain fast and improved concentration reconstructions, (ii) obtain improved operator, (iii) obtain cleaned particle signal from measured phantom data.

- **Scenario (S6):**

Given information (D1 or D2, M2): measured system matrix (\tilde{S}_{D1} or \tilde{S}_{D2}), background measurements $\tilde{v}^{(0)}$ (in (D2) optional), a phantom measurement \tilde{v} , imperfect model for $\bar{\mathbf{m}}$ which allows reasonable reconstruction (see M2).

Possible targets: (i) reduce number of calibration scans (larger delta sample and/or missing regions), (ii) obtain fast and improved concentration reconstructions (e.g., post-processed reconstruction of lower quality), (iii) obtain memory-efficient representation, (iv) obtain correct index set J (in (D2)), (v) obtain completed particle signal, (vi) measured signal correction (background), completion, and optional mapping to range of imperfect model (reconstruction is than obtained via oversimplified model).

- **Scenario (S7) (hypothetical):**

Given information (M3): background measurements $\tilde{v}^{(0)}$, a phantom measurement \tilde{v} , suitable model for $\bar{\mathbf{m}}$ (see M3).

Possible targets: (i) obtain fast and improved concentration reconstructions, (ii) obtain cleaned particle signal from measured phantom data.

4.2.2. Deep Learning and Inverse Problems

In the following subsections we will present the basic ideas behind scenarios of applying Deep Learning to Inverse Problems and briefly introduce explicit methods to deploy them.

We use the following naming conventions:

- The forward operator:

$$A : X \rightarrow Y,$$

where X (a Banach space) the reconstruction space and Y (a Banach space) the signal space.

- $p_X : X \rightarrow \mathbb{R}_{\geq 0}$ the probability density function of the elements/images/concentrations that we want to reconstruct.
- $p_Y : Y \rightarrow \mathbb{R}_{\geq 0}$ the probability density function of the elements/signals/voltages that we are measuring.
- $p_{XY} : X \times Y \rightarrow \mathbb{R}_{\geq 0}$ the joint probability density function.

4.2.2.1. A: Learned Penalty Terms

In variational approaches to Inverse Problems one usually incorporates a so-called penalty function

$$\phi : X \rightarrow \mathbb{R}_{\geq 0}$$



to favor good reconstructions, via minimizing a Tikhonov-type functional

$$\min_x \|Ax - y\|_2^2 + \phi(x)$$

(or similar). This penalty function is usually handcrafted and at best a very rough approximation of what one would want to have as a penalty term. Given enough data to be representative of p_X , one can use neural networks to learn the “ideal” penalty function. This approach has been explored in [52] [53].

Like for the Plug-and-Play Prior Methods, (B), these methods only require knowledge about p_X . This can be provided via handcrafted parts, via known ground truth data or via surrogate, which represents p_X good enough.

- **What do we learn:**

The parametrization θ of a penalty function $\phi_\theta : X \rightarrow \mathbb{R}_{\geq 0}$ (for example represented by a neural network).

- **Intrinsically required knowledge:**

Ground truth data about p_X e. g. in the form of many samples.

4.2.2.2. B: Plug-and-Play Prior Methods

This approach is in some sense (w. r. t. proximal operators) dual to approach A.

Plug-and-Play Prior where introduced in [54], outside the Deep Learning context. The authors pointed out that the alternating direction method of multipliers (ADMM) algorithm used for reconstruction in Inverse Problems could easily be adapted to incorporate any type of denoising method (or more general, any type of algorithm) as a prior during reconstruction. The prior is incorporated by replacing the proximal-operator, $\text{prox}_\phi : X \rightarrow X$, of some penalty function, ϕ (within the reconstruction algorithm e.g. ADMM) with some other operator. It is worth noting, that this operator does not have to be a proximal operator of some penalty function anymore. With the rise of Deep Learning methods people started to learn these proximal-operator which are replaced by neural networks.

It was also possible to extend the basic idea to other algorithms like proximal descent or primal dual hybrid gradient, not just ADMM, see for example [55, 56].

- **What do we learn:**

The parametrization θ of an operator $p_\theta : X \rightarrow X$ that – incorporated in some reconstruction algorithm, in which it replaces the proximal operator of some penalty function – improves the reconstruction.

- **Intrinsically required knowledge:**

Ground truth data about p_X , e. g., in the form of many samples.

4.2.2.3. C: Gradient-Descent-by-Gradient-Descent type Methods

A major field of research in Inverse Problems and Deep Learning is to learn an iterative method from data. This field makes implicit use of the Plug-and-Play prior idea but goes way further. Two very prominent papers in this field are the “Learning Fast Approximations of Sparse Coding” (LISTA) paper [57] and the “Learning to learn by gradient descent by gradient descent” paper [58]. Despite the fact that the paper [58] is not explicitly solving an Inverse Problem their method can be seen as the most data driven form of this type of method. Other authors applied the ideas from [58] directly to solve Inverse Problems [59].

The basic idea of this method has been extended in multiple ways to incorporate prior knowledge e.g. by unrolling existing iteration methods up until a fixed number of iterations and replacing different parts of them by neural networks [60, 61, 62, 63, 64, 65].



One tries to learn parameters θ of a function $f_\theta : Y \rightarrow X$, such that it produces “nice” reconstructions via

$$\min_{\theta} \mathbb{E}_{p_{XY}}[d(f_\theta(y), x)],$$

where d is some measure of distance.

- **What do we learn:**
The parametrization θ of an operator $f_\theta : Y \rightarrow X$ that directly produces “nice” reconstructions.
- **Intrinsically required knowledge:**
Ground truth data about p_{XY} e. g. in the form of many samples.

4.2.2.4. D: Regularization by Architecture

From an abstract point most (if not all) of machine learning methods – and therefore all methods above – can be seen as parameter identification problems. Despite this being the case for all of the above mentioned types this one is the closest to the original notion of parameter identification problems, since no training data is required; one solely fits the parameters θ of a function

$$F_\theta : G \rightarrow \mathbb{R}_{\geq 0}$$

for (usually) a single point of data, $g \in G$ via

$$\min_{\theta} F_\theta(g).$$

These methods are very new, there is only some internal work by us and one very recent paper by a group from the University of Texas [66]. Both works are inspired by a recent paper [67] that noticed, that the inherent structure of so-called convolutional neural networks (CNN) is a good prior for images (even without training). This inspired the authors in [67] to solve Inverse Problems with the prior that the reconstructed image has to lie in the range of a CNN-architecture (non-specific to a given parameterization of the network).

- Deep Image Prior:

$$F_\theta(u) = \|u - Ac(\theta)\|_2^2,$$

where u is the measured signal, A the MPI operator and c (the output of an untrained neural network parameterized by θ whose input is a constant) the concentration.

- Our “Deep Operator Priors” are all of the form:

$$F_\theta(A) = \sum_{i=1}^N w_i \|A_i - f_\theta(c_i)\|_2^2 + \phi(f_\theta, c_i),$$

where f_θ is a neural network representing and enforcing the form of the forward operator in its architecture, A_i usually the columns of a measured operator corresponding to sample concentrations c_i and ϕ a penalty function enforcing structures on weights in the internal representations of f_θ . The w_i are weights to incorporate SNR and similar knowledge. Possible architectures are mixtures of CNN for the spatial structure and RNN (recurrent neural network) for the temporal (frequency) structure.

It is also a still open question whether the $\|\cdot\|_2$ -loss is really the best way to enforce the regression, we are also thinking about using the Wasserstein loss [62].

We see huge potential in these methods, since they allow one to incorporate abstract structural knowledge about the object one ones to regularize. The main difference to “classic” parameter identification is, that one uses deep models as structures (instead of e. g. differential equations). This allows one to incorporate more abstract and less precise knowledge about some underlying structure of a given point of data These methods



relate to traditional parameter identification problems, like Deep Learning relates to machine learning.

We not only want to use these type of methods via the one described in [66], but also via own approaches. We see massive potential in applying these types of ideas to the forward operator via casting abstract knowledge about it into the architectural design of a neural network that in-turn is fitted to a measured (noisy and error prone, maybe incomplete) version of the forward operator.

These methods are especially interesting for Magnetic Particle Imaging, since they do not rely on ground truth data. This is crucial, since for MPI – as well as for nearly any other novel Inverse Problem – one can not expect to have sufficient ground truth data, see chicken-and-egg-problem.

- **What do we learn:**
A regularized version of some data point (e. g. an image or even an operator itself).
- **Intrinsically required knowledge:**
Any kind of abstract knowledge about the data point could potentially be incorporated.

4.2.2.5. E: Image Post-Processing via Deep Learning

Of course, all kinds of image post-processing techniques can be applied to improve MPI reconstructions: inpainting, denoising, deblurring, etc. The leading methods in this field are mostly Deep Learning based nowadays. The amount of literature is expanding rapidly, see for examples [68, 69, 70, 71, 72, 73, 74].

4.2.3. Applying Deep Learning to Magnetic Particle Imaging

In MPI we have to deal with the full extend of the chicken-and-egg problem described earlier. Therefore many of the methods described above that rely on ground truth data (and which in general do not solve new Inverse Problems) are not applicable. This makes MPI an example par excellence for bringing Inverse Problems and Deep Learning together in solving previously unsolved Inverse Problems.

Possible approaches to tackle this union:

- Use surrogate data sets.
- Regularization via Architecture.

Using surrogate data sets means to use data that is presumably similar to MPI data, like MRI data, to boot strap a Deep Learning approach. Approaches that lean to that are especially approaches of the kind, where one learns a penalty term, since these methods are intrinsically from the Inverse Problem itself.

Using architecture as a regularization is a very new field. Obviously Deep Image Prior should be implemented for MPI, but there are a myriad of other opportunities to evaluate. For example one could use the structure provided by a recurrent neural network, like a long-short-term-memory network (LSTM) combined with a convolutional neural network to do inpainting/deblurring on the measured operator to reconstruct measurements with bad signal-to-noise ratios. This could be done via one big optimization in which one optimizes the structure of an extremely deep LSTM that reaches over all frequency-(or time) measurements of an operator at the same time. The goal of the optimization is to fit the output of the network to the measured operator (learning its structure) weighted by the signal-to-noise ratio of the measurements.

4.3. Data sets

On GitHub (<https://magneticparticleimaging.github.io/OpenMPIData.jl/latest/index.html>) an open magnetic particle imaging data set is available in the MPI data format (MDF) that can be read from any programming language like Matlab, Python, Julia and C. MDF provides a common data format for the storage of MPI raw data, calibration data and reconstruction data. The data set is available under the creative commons license and therefore for everyone free to use, to share and to adapt the data by citing the project and the MDF publication (<https://arxiv.org/abs/1602.06072v6>).

DL scenario	MPI scenario	S1	S2	S3	S4	S5	S6	S7
	A	0.10	0.10	0.15	0.05	0.75	0.85	0.90
B	0.10	0.10	0.15	0.05	0.75	0.85	0.90	
C	0.10	0.10	0.15	0.00	0.80	0.90	1.00	
D	0.70	0.70	0.75	0.00	0.00	0.80	0.85	
E	**	**	**	**	**	**	**	

Table 2: The bigger the number the more potential we see for improving image quality via Deep Learning Methods. For the methods (A), (B) and (C) we always assume the existence of good surrogate data to model p_X , e. g. MRI data or MPI X-space data. ** denotes the cases that require further investigation.

DL scenario	MPI scenario	S1	S2	S3	S4	S5	S6	S7
	A				[52]		[52]	[52]
B				[56]		[56]	[56]	
C				[63]		[63]	[63]	
D		[75],*	[75],*	[75],*			[75],*	
E		**	**	**	**	**	**	**

Table 3: Relevant short- and mid-term projects are marked with citations for papers which should be adapted to MPI. All scenarios associated with S7 are long-term projects. * denotes ideas approached in the near future. (E) needs some work to identify most promising approaches to be adapted to MPI. ** denotes the cases that require further investigation.

The MPI data set has been measured with a Bruker PreclinicalMPI Scanner (Bruker Biospin, Ettlingen, Germany) and the dextran based magnetic nano-particles perimag (micromod, Partikeltechnologie GmbH, Rostock, Germany) have been used as tracers for the experiments. For the MPI measurements phantoms printed with the stereolithography 3D printing technique were used. All phantoms share the same robot mount defining the coordinate system. The robot mount is fixed in positive X direction. The flat side marks the positive Z direction. The positive Y direction is then defined by right hand rule.

To resemble a well-known **shape phantom** a cone defined by a 1 mm radius tip and an apex angle of 10 deg and a height of 22 mm. The total volume is 683.9 μl . As tracer perimag in a concentration of 50 mmol per l were used. The phantom can be rendered in 3D resembling the cone or can be cut in layer view to see either a circle (YZ plane) or a triangle with flattened tip (XZ or XY plane).

The **resolution phantom** consists of five tubes filled with perimag featuring a concentration of 50 mmol. The five tubes have a common origin on one side of the phantom. From there they extend in different angles from this origin within the XY and YZ plane are chosen smaller (10 and 15 deg) than in XY direction (20 and 30 deg). By choosing different planes, one can determine the capable resolution due to different distances of the tubes.

The **concentration phantom** consists of eight cubes 2 mm length resulting in 8 μl volume each. The distance of the cubes are 12 mm between centres within the XY plane and 6 mm between centres within Z direction. The concentrations in the eight sample chambers are different, ranging from 5.85 to 44.4 mmol per l.

Several MPI sequences have been used for data acquisition.

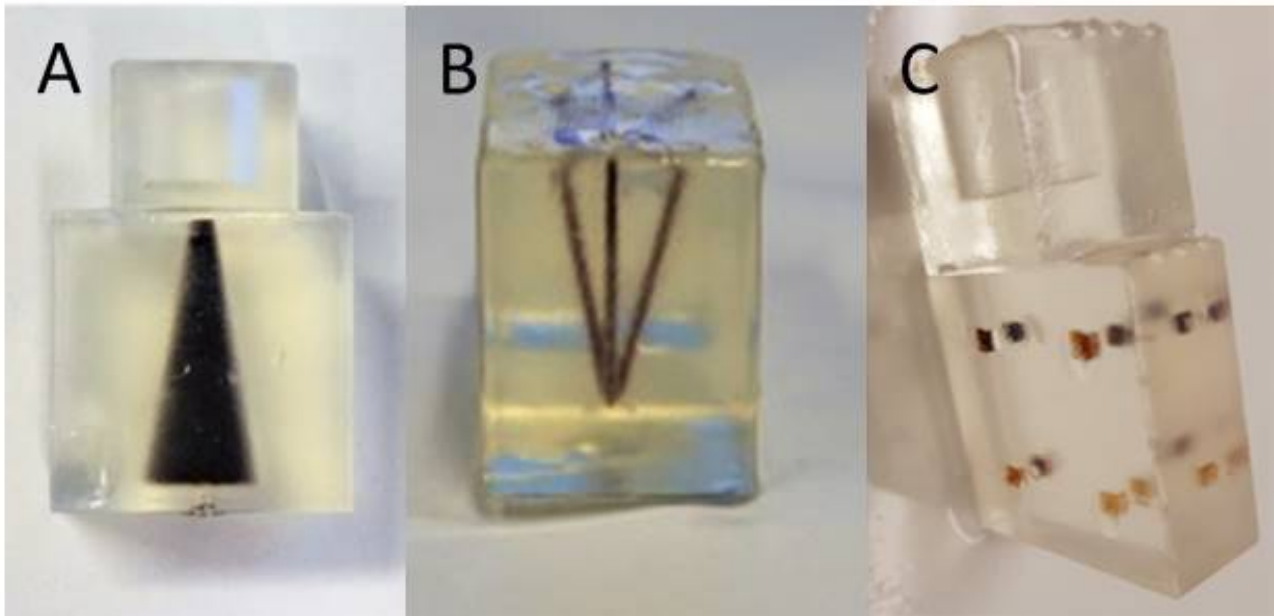


Figure 4.1: Visualization of phantoms used for MPI measurements. A: shape phantom, B: resolution phantom and C: concentration phantom

4.3.1. 1D Cartesian Sequence

During the measurement of the 1D sequence the phantom has been moved step-wise in the z-dimension and afterwards in the y-dimension with the robot. Each patch represents one robot position, in total $19 \times 19 = 361$ 1D patches per position.

4.3.2. 2D Lissajous Sequence

During the measurement of the 2D sequence the phantom has been moved step-wise in z-dimension with the robot. Each patch represents one robot position, in total 19 2D patches per position.

Part V.

Benchmarks for the Modelling of Continuous Casting Molds

Umberto Morelli, Peregrina Quintela, Patricia Barral, Gianluigi Rozza, Michele Girfoglio, Gianfranco Marconi, Conte Riccardo

Abstract

The objective of the present research project is the development of a control algorithm for a continuous casting mold equipped with thermocouples. The algorithm will have to solve in real time the inverse and direct heat transfer problem in a water cooled copper mold providing the instantaneous heat flux at the mold inner boundary and the temperature gradients within the mold. This document provides a description of the process and a hierarchy of the mathematical models used for the simulation of continuous casting molds. Moreover, different benchmarks are presented for the validation and analysis of the algorithms which will be developed in the present research.

Keywords: Continuous casting, mold, heat transfer, reduce order modeling, inverse heat transfer problem.

5.1. Introduction and Motivation

The continuous casting (CC) of steel is presently the most used process to produce steel worldwide. In 2017, 96% of the steel was produced using CC [76]. This process has been used for decades and during this time it has undergone improvements based mainly on experience with the commercial operation, aided by physical water modeling to understand the fluid flow behavior and more recently by numerical simulations [77]. In this section an overview of the CC process, illustrated in Figure 5.1, is provided. Finally at the end of the section, the motivation and objectives of the present research are presented.

In continuous casting the metal is first heated until it liquefies. The molten metal is then tapped into the ladle. When it is at the correct temperature, the metal goes into the tundish. The tundish plays the role of a reservoir while one ladle is empty and it is substituted by another. In the tundish the metal flow is regulated and smoothed. Through the Submerged Entry Nozzle (SEN), the metal is drained into an open-base copper mold. The mold is water cooled to start the solidification of the metal (primary cooling). The SEN drains the metal below a layer of mold powder which is floating at the top of the molten metal in the mold as in Figure 5.2. Part of the powder in contact with the steel melts down creating a liquid layer. This layer fills the gap between the steel and the mold. Due to the heat extraction at the mold face, a portion of the liquid resolidifies in contact with the mold creating a solid layer. Finally, due to the strand shrinkage, an air gap can occur in the lower part of the mold especially at the strand corners. This air gap reduces the heat extraction from the steel to the mold. Consequently, the molds are generally tapered to reduce this air gap.

The steel solidification starts at the mold and continues all the way down the secondary cooling section. In this region, the strand is supported by a series of cooled rollers and sprayed with water. The complete solidification of the strand is achieved at the end of this section.

The mold design and working conditions directly influence the final product quality and the production capacity of a continuous caster as well as the mold life time. The present investigation arises from the need of the industrial partner of the project, Danieli & C. Officine Meccaniche S.p.A. [79], to have a robust and versatile control system for their continuous casting molds. To analyze and control the behavior of a casting mold, it is essential to know the instantaneous temperature field and heat fluxes in it. The molds are equipped with thermocouples installed within the copper plates of the mold. These thermocouples provide temperature measurements at different locations of the mold. To control the mold, the instantaneous heat fluxes at the mold face in contact with the strand have to be computed based on the thermocouples measurements (inverse problem).



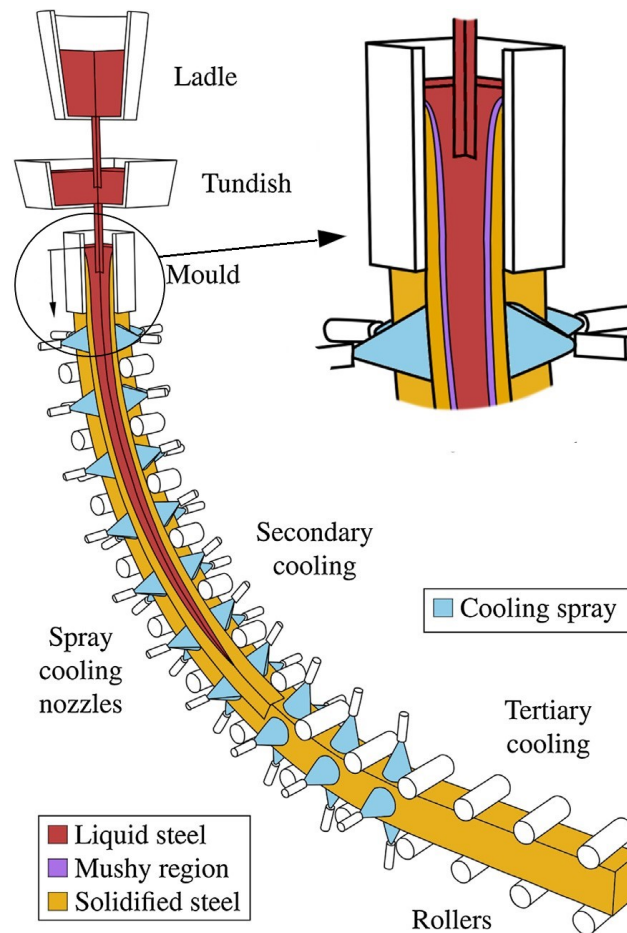


Figure 5.1: Schematic overview of the continuous casting process [78]. The molten steel is tapped from the ladle to the tundish. Then, the SEN injects it into the mold where the steel begins its solidification. Starting from the mold, the steel slab is cooled and it reaches complete solidification in the secondary cooling region.

Then, knowing the heat fluxes at the boundary, the temperature gradients in the mold can be computed (direct problem) allowing the control of the machine and the adjustment of the casting parameters to optimize the process. The main goal of the present investigation is the development of a control algorithm for the CC mold which can achieve the aforementioned computations in real time within the machine control system. To achieve this goal, Reduced Order Modeling (ROM) techniques will play a fundamental role in the investigation. Consequently, benchmarks are required to validate, study and compare the obtained results, and to compare the performance of different algorithms.

5.2. State of the art

An extensive literature on the modeling of continuous casting direct simulation and the aforementioned inverse problem is available. In this section a brief overview is provided and discussed.

5.2.1. Direct problem

The direct simulation of continuous casting is a very complex problem. Many interacting phenomena occur in the mold region including heat transfer, solidification, multiphase turbulent flow, clogging, complex interfacial behavior, thermo-mechanical distortion, stresses, cracks, segregation and microstructure formation. These phenomena are generally transient, three-dimensional, and operate over wide length and time scales. Consequently, several models have been developed ranging from fast and simple models for implementation in online control



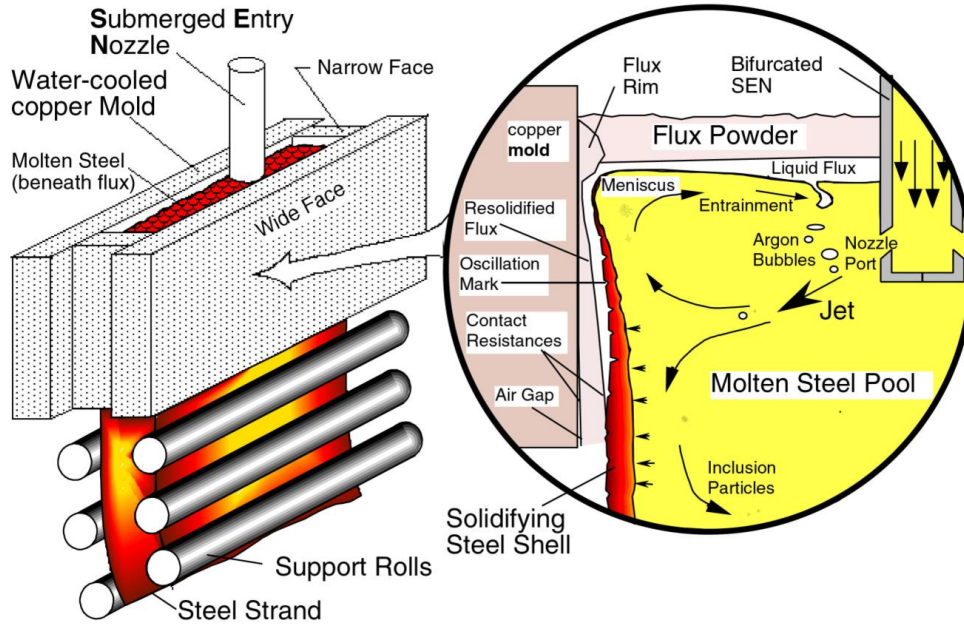


Figure 5.2: Schematic of a vertical section of the mold region [80]. On the left, the main phenomena occurring within the mold are illustrated. In particular, the figure shows the gap which forms between the steel and the mold. This gap is filled by the flux powder which liquefies in contact with the hot steel and resolidifies close to the mold face. In the lower part of the mold an air gap can occur due to the slab shrinkage. Molds are generally tapered to reduce this air gap.

systems to sophisticated multiphysics simulations that take into account many coupled phenomena (an updated review on this subject by Thomas [77] is available).

The complexity of the model depends on the physical phenomena considered and the domain used. In this section an overview of the mold models available in the literature is presented. Because the present investigation regards the mold and its cooling system, models related to the steel flow in the slab and its solidification are not discussed here.

A models hierarchy is illustrated in Figure 5.3. In this section, the mathematical models found in the literature are described from the simplest to the more complex.

Considering only the mold copper region, the transient three-dimensional heat equation is [81]

$$\rho_c C_{pc} \frac{\partial T_c}{\partial t} = \nabla \cdot (k_c \nabla T_c), \quad (5.1)$$

where $T_c = T_c(\mathbf{x}, t)$ is the copper temperature, ρ_c its density, $k_c(T_c)$ the thermal conductivity, and C_{pc} the specific heat capacity. Assuming a steady-state process and constant properties [82, 83], the heat equation can be simplified as

$$\Delta T_c = 0. \quad (5.2)$$

In any case boundary conditions (BC) are provided. At the portion of the boundary in contact with the slab or with the air if the slab shrinkage creates a gap (so called "hot" face) Γ_{hot} , the empirical heat flux proposed by Savage and Pritchard [84] is commonly imposed

$$-k_c \frac{\partial T_c}{\partial n} \Big|_{\Gamma_{hot}} = q(v_c, z) = A_0 + B_0 \sqrt{t_{dwell}(v_c, z)}, \quad (5.3)$$

where A_0 and B_0 are coefficients dependent on the casted steel, and $t_{dwell} = z/v_c$ is the slab dwell time which



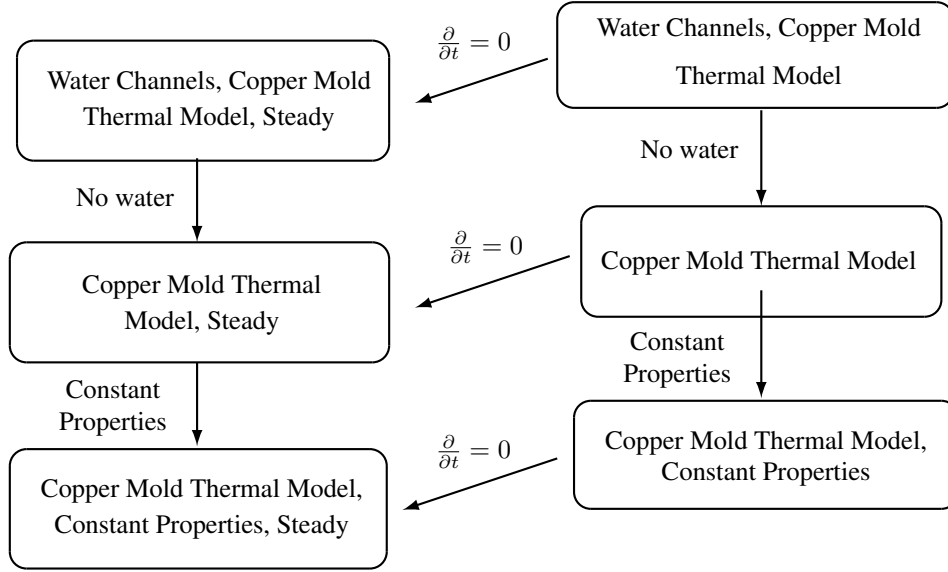


Figure 5.3: Models hierarchy for the direct simulation of continuous casting molds.

is a function of the cast velocity v_c and of the axial coordinate along the mold z .

Alternatively, the heat flux at this boundary can be computed solving the inverse problem (discussed in the next section). The computed heat flux can then be applied as a boundary condition in the direct problem [85].

At the portion of the boundary in contact with the cooling water Γ_w , a convection boundary condition is applied

$$-k_c \frac{\partial T_c}{\partial n} \Big|_{\Gamma_w} = h_w (T_c - T_w), \quad (5.4)$$

where T_w is the local water temperature. In the literature when this model has been used, T_w is assumed to increase linearly along the water channel from the inlet temperature [86].

The water channel heat transfer coefficient h_w can be calculated using the Sleicher Rouse equation [87]

$$h_w = (5 + 0.15 Re^{C1} Pr^{C2}) \frac{K}{D} \quad (5.5)$$

where

$$\begin{aligned} C1 &= 0.88 - \frac{0.24}{4 + Pr}, \\ C2 &= 0.333 + 0.5e^{-0.6Pr}, \\ K &= 0.59 + 0.001(T_w [K] - 273), \\ D &= 4A/P \end{aligned} \quad (5.6)$$

where Re and Pr are the Reynolds and Prandtl numbers, A the cross sectional area of the water channel and D the perimeter.

Commonly, the heat flux at the portions of the boundary in contact with "cold" air (i.e. upper Γ_{up} and lower Γ_{low} faces of the mold, and the outer part of the mold not in contact with cooling water Γ_{out}) is neglected [88, 82, 89, 86]

$$-k_c \frac{\partial T_c}{\partial n} \Big|_{\Gamma_{up}} = -k_c \frac{\partial T_c}{\partial n} \Big|_{\Gamma_{low}} = -k_c \frac{\partial T_c}{\partial n} \Big|_{\Gamma_{out}} = 0. \quad (5.7)$$

Consequently, in these models the heat flows into the mold from its hot face and flows out from the water



channels.

The complexity of the model can be increased including in the domain the water flowing in the cooling system [90]. This improvement of the model is especially required when the cooling system geometry is complex and it is not possible to assume a temperature profile.

Modeling water as a Newtonian fluid, its flow can be modeled using RANS and a turbulence model (i.e. $k - \epsilon$). Assuming steady flow, the water model includes continuity equation

$$\nabla(\rho_w(T_w)\mathbf{u}) = 0, \quad (5.8)$$

momentum conservation equation

$$\nabla \cdot (\rho_w(T_w)\mathbf{u} \otimes \mathbf{u}) = -\nabla p_w + \nabla \cdot [\mu_{eff}(T_w)(\nabla\mathbf{u} + \nabla\mathbf{u}^T)] + \rho_w(T_w)\mathbf{g}, \quad (5.9)$$

and the energy equation

$$\frac{k_w}{\rho_w C_{p_w}} \Delta T_w = \mathbf{u} \nabla T_w. \quad (5.10)$$

In these equations, T_w is the water temperature, $\rho_w(T_w)$ the density, \mathbf{u} the Reynolds averaged water velocity vector, and $\mu_{eff} = \mu + \mu_t$ the effective viscosity composed of the dynamic viscosity $\mu(T_w)$ and the turbulence viscosity μ_t . In a general case, the water properties are calculated as a function of the water temperature.

The heat transfer between water and copper is again expressed by Eq. 5.4. With T_w being the computed water temperature at the boundary while h_w is computed based on local flow-field conditions.

5.2.2. Inverse problem

The mold is equipped with a number of thermocouples that measure the temperature at different locations in the copper mold. Moreover, the cooling water flow is measured as well as the water averaged temperature at the inlet and outlet of the cooling system. As previously mentioned, an inverse problem has to be solved for the computation of instantaneous heat fluxes at the mold hot face.

This is a well known problem in the literature and several inverse problem solution techniques have been used. Such as conjugate gradient method, genetic algorithm, Nelder-Mead algorithm, least square method. Even the use of neural networks has been explored [91].

In the literature, the validation of the inverse problem model has been conducted in two ways: (i) using real mold thermocouples measurements and comparing them to the temperatures computed at the thermocouples positions using the BC of the inverse model [92, 91, 93] or (ii) creating a numerical test case of which the BC are known and validating the inverse problem model by its ability to reconstruct this boundary condition [94, 95].

Being the objective of the present investigation the development of a real time control algorithm, different inverse problem solution techniques will be studied in order to select the most computationally efficient. More importantly, the implementation of ROM in the inverse problem will be investigated as a possible solution to achieve real time solution performances.

5.3. Benchmarks

In the literature it is possible to identify notable test cases which geometry and thermal state is publicly available. These test cases have been identified and are proposed here as benchmarks for the validation and analysis of the algorithms which will be developed in the present research. Moreover, the design of a new valuable test case is proposed in partnership with the industrial partner.

The selected benchmarks can be divided into analytical solutions, experiments and numerical simulations. These test cases have been used in the literature in different ways but mainly for validation of direct simulations, validation of inverse problem solvers, research on mold design and/or optimization of the measurement



system [95].

Table 4: Benchmarks selected for the present investigation.

Type	1D	2D	3D
Analytical solutions	Benchmark 1 [96] Benchmark 2 [97]		
Experiments			Benchmark 6 [90] Benchmark 3 [88] Benchmark 5 [98] Benchmark 8
Numerical simulations		Benchmark 3 [95] Benchmark 4 [94] Benchmark 5 [85]	Benchmark 6 [90] Benchmark 7 [90] Benchmark 8

5.3.1. Benchmark 1

Analytical solutions are available for an infinite plate in different conditions. Two cases will be considered [96]:(i) a infinite uniform plate with applied heat flux on one side and heat convection on the other in steady condition, and (ii) a infinite uniform plate with uniform temperature at time t_0 and convection on both sides.

Assuming constant properties, the solution of the one-dimensional problem (i), shown in Figure 5.4 is:

$$T(x) = q_{in} \left(\frac{L-x}{k} + \frac{1}{h} \right) + T_{\infty} \quad (5.11)$$

where q_{in} is the heat flux on the left side of the plate, L the plate thickness, k the thermal conductivity on the plate, h the convection heat transfer coefficient on the right side, and T_{∞} the surrounding temperature.

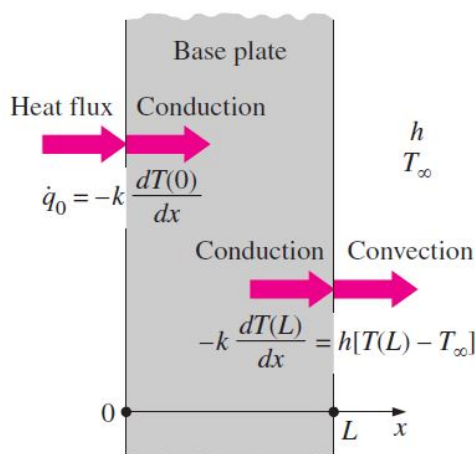


Figure 5.4: Schematic of the infinite uniform plate in steady condition with applied heat flux on one side and heat convection on the other one (Benchmark 1.i) [96].

Assuming constant properties, the solution of the one-dimensional problem (ii) for the dimensionless time $\tau = \frac{\alpha t}{k} > 0.2$ can be approximated as [96]:

$$\theta(x, t) = \frac{T(x, t) - T_{\infty}}{T_i - T_{\infty}} = A_1 e^{-\lambda_1^2 \tau} \cos(\lambda_1 x/L), \quad \tau > 0.2 \quad (5.12)$$



where A_1 and λ_1 are dependent on the Biot number $Bi = \frac{hL}{k}$ only and T_i is the temperature at t_0 .

5.3.2. Benchmark 2

The classical steady state conjugated problem in Figure 5.5 (Luikov problem) has been selected as a benchmark because it involves convection on one face of the plate as in a simplified mold model.

For thin plates, the solution of the problem is [97]

$$\theta_T(\tau) = \frac{T_b - T(x)}{T_b - T_\infty} = \sum_{i=1}^{\infty} c_i Br_x^i \quad (5.13)$$

where $Br_x = \frac{k_f b}{k_s x} Re_x^m Pr^n$ is the Brun number and the constants c_i are obtained from

$$c_1 = \frac{-1}{a_0 + a_1},$$

$$c_{i+1} = \left(\sum_{j=1}^{i+1} \frac{\Gamma(i+2)}{\Gamma(i+2-j)} a_j \right)^{-1} c_i, \quad i = 1, 2, 3, \dots \quad (5.14)$$

where Γ is the Gamma function and

$$a_j = -\frac{\Gamma(\beta)\Gamma(\frac{1}{\gamma})}{C\gamma} \sum_{i=j}^{\infty} \sum_{r=0}^j \binom{-\beta}{i} \binom{i}{r} \frac{(-1)^r \prod_{p=-i+1}^0 \left(\frac{j-r}{\gamma} (m-1) + p \right)}{\Gamma(\frac{1}{\gamma} + \beta + i)\Gamma(j+1)} \quad (5.15)$$

where C , γ , m , and β are constants dependent on the condition of the flow (turbulent or laminar).

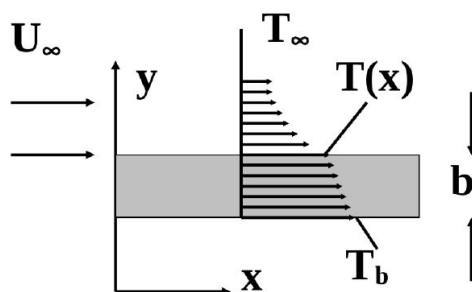


Figure 5.5: Plate with uniform temperature T_b at lower surface and convectively cooled at upper surface (Luikov problem). [97].

5.3.3. Benchmark 3

Udayraj et al. [95] developed a benchmark case based on the experimental results by Samarasekera and Brimacombe [88]. The mold considered has a total height $H + H_1 = 700 \text{ mm}$ and a width $L = 96 \text{ mm}$. The domain considered is a rectangular two dimensional vertical slice of the mold. The mold is made up of copper with thermal conductivity $k_c = 390 \text{ W/mK}$. The meniscus is located at $y = H = 617.6 \text{ mm}$ and the water enters in the channel from the bottom ($y = 0$) at a speed $U_w = 7 \text{ m/s}$ and with temperature $T_{w_{in}} = 303.15 \text{ K}$. Water properties are summarized in Table 5. The casting speed is $v_c = 0.0375 \text{ m/s}$.

Table 5: Water properties of Benchmark 3 [95].

Density, ρ_w	999.97 kg/m^3
Specific heat, c_{p_w}	4180 J/kgK
Dynamic viscosity, μ_w	$79.77 \cdot 10^{-5} \text{ Ns/m}^2$
Thermal conductivity, k_w	0.6 W/mK
Heat transfer coefficient, h_w	$22500 \text{ W/m}^2\text{K}$

The Savage and Pritchard [84] heat flux is applied at the hot face

$$q_s(y) = 2680 - 335 \sqrt{\frac{H-y}{v_c}} \left[\frac{\text{kW}}{\text{m}^2} \right]. \quad (5.16)$$

For this test case, measured and simulated temperature distributions on hot and cold face are publicly available.

5.3.4. Benchmark 4

Zhang et al. [94], developed the 2D test problem shown in Figure 5.6. The test problem is a rectangular area ABEF with $H = 21 \text{ mm}$ and $W = 12 \text{ mm}$, starting at 288 K . The AF and BE boundaries are insulated. The EF boundary is cooled off by water with convection heat transfer coefficient $h_w = 1 \cdot 10^4 \text{ W/m}^2\text{K}$ and temperature $T_w = 288 \text{ K}$. The heat flux $q(\partial\Omega_2, t)$ is applied to boundary AB, where $\partial\Omega_2 = \{(x, y) : x = 0 \text{ mm} \leq y \leq 21 \text{ mm}\}$ and $0 \text{ s} \leq t \leq 25 \text{ s}$. The heat flux $q(\partial\Omega_2, t)$ profile is decreasing linearly in the y-axis and varies triangularly in time,

$$q(\partial\Omega_2, t) = \begin{cases} 1 \cdot 10^6, & 0 \text{ s} \leq t \leq 5 \text{ s} \\ 1 \cdot 10^6 \left(1 - \frac{y[\text{mm}]}{21 \text{ mm}} \right) \frac{t[\text{s}]}{5 \text{ s}} + 1 \cdot 10^6, & 5 \text{ s} \leq t \leq 10 \text{ s} \\ 1 \cdot 10^6 \left(1 - \frac{y[\text{mm}]}{21 \text{ mm}} \right) \frac{20 \text{ s} - t[\text{s}]}{5 \text{ s}} + 1 \cdot 10^6, & 10 \text{ s} \leq t \leq 15 \text{ s} \\ 1 \cdot 10^6. & 15 \text{ s} \leq t \leq 20 \text{ s} \end{cases} \quad (5.17)$$

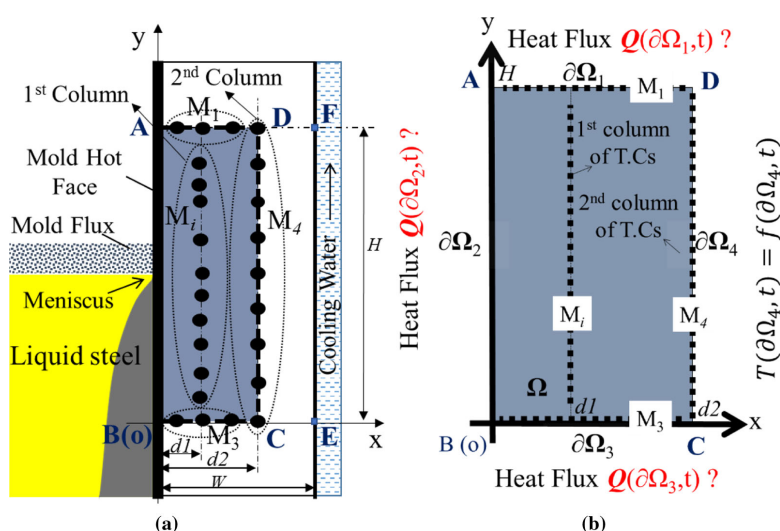


Figure 5.6: Scheme of the benchmark developed by Zhang et al. [94]: (a) the locations of thermocouples in the copper mold, where the dots represent thermocouples, and (b) the inverse problem computational domain and the boundary conditions.

In the test problem calculation, eight virtual response thermocouples of 1st column are spaced 3 mm apart in



y-axis and located 3 mm away from the AB boundary to provide the temperature for minimizing the objective function of inverse calculation. The other eight virtual thermocouples of the 2nd column spaced 3 mm apart in y-axis and located 8 mm away from the AB boundary to provide the boundary condition as show in Figure 5.6(b). The direct problem on this test domain is then solved with a 0.2 mm x 0.2 mm grid size and 0.01 s time-step. The temperature is stored every 0.1 s. Subsequently, the measured simulated temperatures are given as input of the inverse model for the estimation of the heat flux on $\partial\Omega_2$.

Using this benchmark case, Zhang et al. tested the robustness of the inverse problem model. A Gaussian noise signal $\omega\sigma$ was added to the simulated temperature to mimic the measurement error, where the standard deviation of noise σ is set as 0, 0.1 and 0.2, and $-2.576 \leq \omega \leq 2.576$ is a random variable.

5.3.5. Benchmark 5

A three-dimensional test case have been developed by Du et al. [85, 98] to validate their 2D model. They experimentally measured the temperature at different locations of the curved caster of Figure 5.7. The caster has a curvature radius of 10.75 m and metallurgical length of 28.8 m with a casting speed $v_c = 0.65$ m/min. The copper mold is coated with 1 mm of nickel on the hot face. The thermophysical properties of the materials are summarized in Table 6. Other geometry and process parameters are summarized in Table 7. A detail of the water slots at the outside radius is illustrated in Figure 5.8.

Table 6: Thermophysical properties of materials used in Benchmark 5 [95].

Material	Specific heat [J/kgK]	Thermal conductivity [W/mK]	Density [kg/m ³]
Copper	390	340	8900
Nickel	460	80	8910
Water	4200	0.5	998

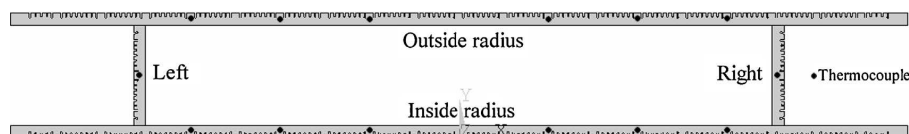


Figure 5.7: Horizontal section of the mold used in Benchmark 5 [98].

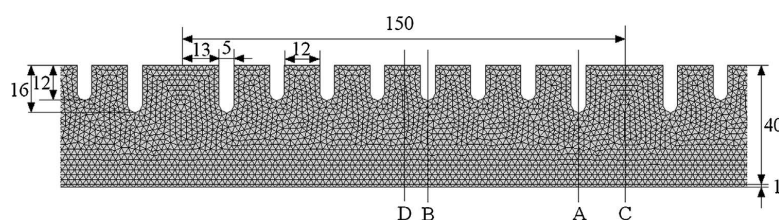


Figure 5.8: Detail of the water slots at the outside radius of the mold of Benchmark 5 [98].

In Figure 5.9 the measured temperatures are compared with the temperature profile along the width direction at the buried sections of the thermocouples. As shown in the figure, three rows of thermocouples were buried in the mold 210 mm, 325 mm and 445 mm from the mold top.

5.3.6. Benchmark 6

Meng and Thomas [89] developed a benchmark case for the validation of their COND1D model which was used later on by other investigations in the literature. The benchmark is based on measurements presented in previous research.



Table 7: Geometry and process parameters of Benchmark 5 [95].

Item	Value
Mold height	900 mm
Copper plate thickness	40 mm
Slab width	2100 mm
Slab thickness	320 mm
Water slot width	5 mm
<i>Water slots depth</i>	
Inside radius	16 mm, 20 mm
Outside radius	12 mm, 16 mm
Narrow face	12 mm, 16 mm
Casting speed	0.65 m/min
Meniscus level	100 mm
<i>Water temperature</i>	
Inlet	304.8 K
Outlet for inside radius	308.9 K
Outlet for outside radius	310.5 K
Outlet for narrow faces	310.4 K
<i>Water flow</i>	
Inside radius	0.097 m ³ /s
Outside radius	0.074 m ³ /s
Narrow faces	0.0108 m ³ /s
<i>Thermocouples distance from hot face</i>	
Inside radius	14 mm
Outside radius	28 mm

The water channels and copper plate domain dimensions and spacing are shown in Figure 5.10(a) and Figure 5.11. Water properties are all calculated as function of temperature. The thermophysical properties of the copper used in this test case are summarized in Table 8. The temperatures measured at the wall illustrated in Figure 5.11 and the thermocouples position are shown in Figure 5.10(b). The inlet water temperature is 303.15 K and the velocity 7.8 m/s. The averaged water temperature rise is 7.1 K.

Table 8: Thermophysical properties of copper used in Benchmark 6 [90].

Material	Specific heat [J/kgK]	Thermal conductivity [W/mK]	Density [kg/m ³]
Copper	410	335 at 298 K	8940
		315 at 393 K	
		310 at 623 K	

5.3.7. Benchmark 7

This benchmark is based on numerical simulations conducted by Xie and Chen [90]. A section of the studied mold is shown in Figure 5.12. The geometric and process parameters are summarized in Table 9. The temper-



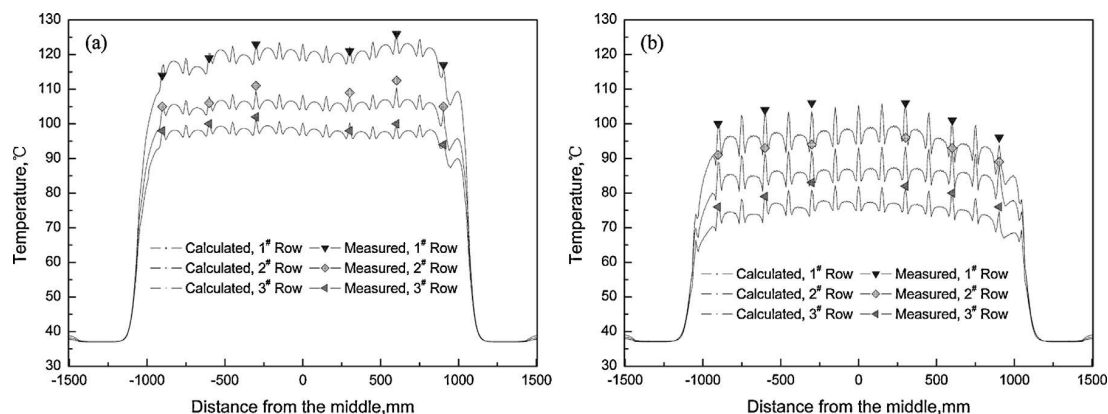


Figure 5.9: Measured temperature of Benchmark 5. In the figure these measurements are compared with the temperature profiles computed by Du et al. [98]. The measurement are the averaged temperatures over an interval of 20 min. (a) Inside radius; (b) outside radius.

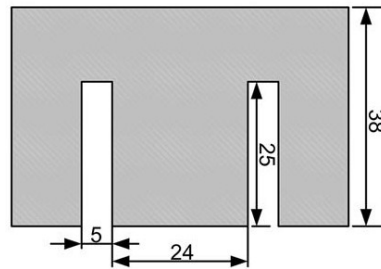
ature profile applied at the hot face of the mold as a first kind of boundary condition is shown in Figure 5.13. The thermophysical properties of copper are the same as in Table 8. For this benchmark case, the temperature distribution computed by Xie and Chen is available for the copper mold and water channels at different sections of the mold.

Table 9: Geometry and process parameters of Benchmark 7 [90].

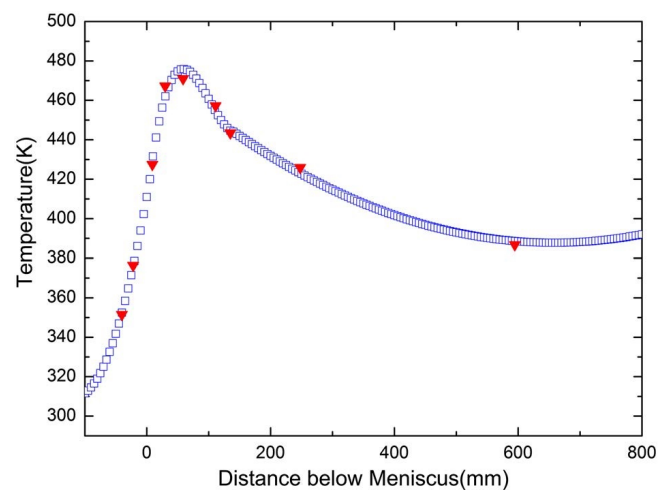
Item	Value
Slab cross-section	250x2000 mm ²
Mold height	900 mm
Mold working length	800 mm
Casting speed	1.15 m/min
<i>Water flow</i>	
Wide plate	5009 L/min
Narrow plate	515 L/min
<i>Water inlet velocity</i>	
Wide plate	8.382 m/s
Narrow plate	8.086 m/s
Water inlet pressure	1 MPa

5.3.8. Benchmark 8

A benchmark case will be designed base on data provided by Danieli. The idea is to design a three dimensional test case in which the water channels have three-dimensional geometry as in Danieli's mold. In this case is not possible to assume the water temperature along the channels. Consequently, they would have to be included in the domain of the simulation and properly simulated.



(a) Water channel geometry and thermocouples plane position.



(b) Temperature measurements (triangles) and temperature profile used for validation (squares).

Figure 5.10: Geometry of Benchmark 6 [90]

(a) and relative temperature profile (b). In (b) the temperature measured by the thermocouples are indicated as red triangles while the temperature profile was computed by Xie and Chen [90] fitting the measurements, to validate their model.

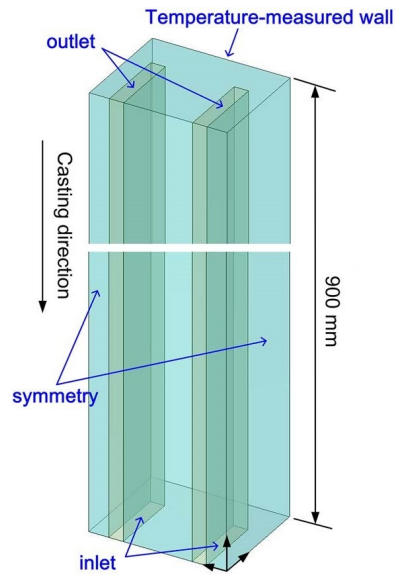


Figure 5.11: Domain of Benchmark 6 [90]. The lateral faces are plane of symmetry, the other walls were adiabatic.

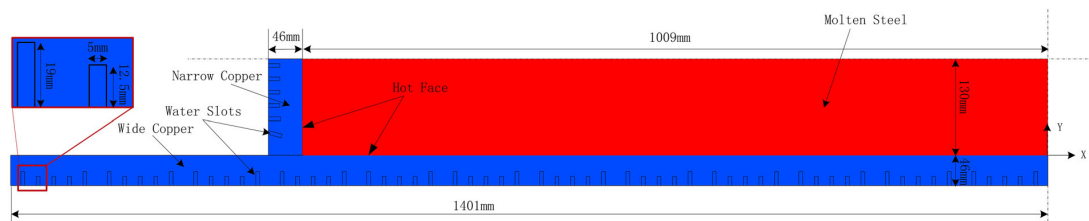


Figure 5.12: Cross section of the mold of Benchmark 7 [90]. Only a quarter of the mold is shown because of the symmetry.

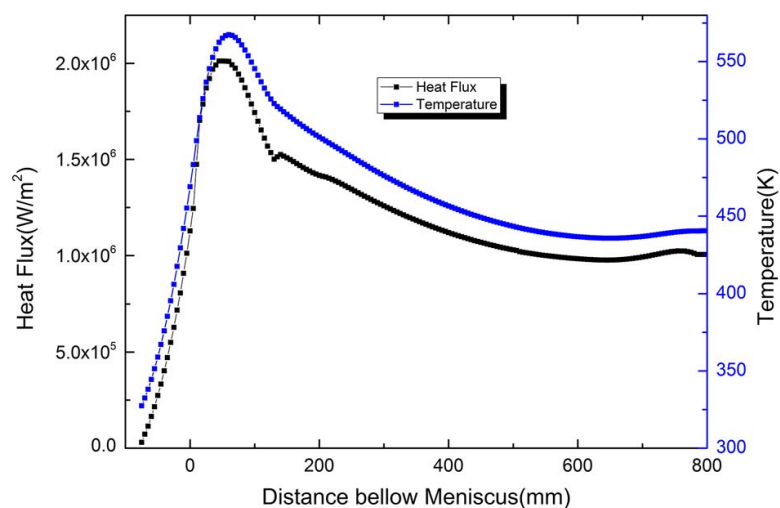


Figure 5.13: Temperature profile applied as boundary condition at the hot face of the mold in Benchmark 7 [90] and related heat flux.

Part VI.

Benchmark case of model hierarchies: Experimental-based Validation of FSI Simulations in Blood Pumps

Marco Martinolli, Christian Vergara, Pier Paolo Monticone, Luc Polverelli

Abstract

Unlike the rotary blood pumps currently available in the VAD market, the progressive wave pump developed in CorWave SA has the ability to provide true pulsatile blood flow, exerting low shear stress on red cells and thus reducing the risks associated with blood trauma and internal bleeding. The innovative pumping technology of the device relies on the mutual interaction between the blood flow and an oscillating polymer membrane, that is mathematically described by a Fluid-Structure Interaction hierarchical model. The benchmark consists of the validation of such model against experimental real data provided by CorWave, related to blood flow, pressure, membrane displacement and force. In particular, the validation approach will focus on a comparative analysis of the results obtained via simulations and via experiments, by looking at the pump characteristic PQ curves and at the recorded membrane position in time.

Keywords: Fluid-structure interaction, blood pumps, model validation.

6.1. Introduction

6.1.1. Introduction to Blood Pumps

Blood pumps are medical devices that are implanted in the chest of patients who have gone through episodes of heart failure or cardiac surgery. Belonging to the class of Left Ventricular Assist Devices (LVADs), their function is to take over the blood pumping capability of the heart by pumping mechanically part of the blood from the left ventricle into the ascending aorta. Specifically, the device is surgically implanted below the heart and connected to the apex of the left ventricle (i.e. its bottom part) to collect the blood from the ventricular chamber; then the blood enters in the pump and it is automatically ejected into the aorta via a flexible woven cannula. The blood pump is powered by external batteries via an electrical cable that passes through the patient's skin and transmits the input current to the pump engine. In addition, the motor functioning and the internal blood dynamics are controlled from the outside by means of inner sensors. The overall structure of an implantable blood pump is shown in Figure 6.1.



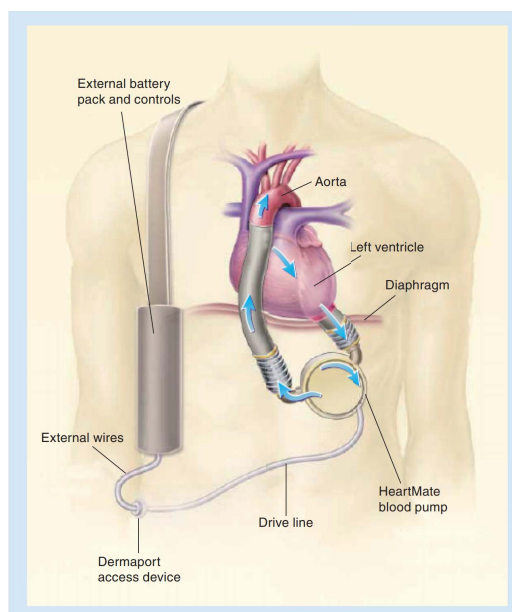


Figure 6.1: General components of an intracorporeal left ventricular assist device, specifically the HeartMate model. Figure taken from reference paper [99].

Blood pumps help to suppress the symptoms of heart failure and recover regular blood flow and they are able to maintain patients alive for several years (in the best cases for up to ten years). They can be used in a wide spectrum of treatments, depending on the health state of the patient (age, hypertension, smoking, cancer, etc.) and on the severity of the heart disease. In fact, blood pump treatments can be employed either on patients whose regular heart function may be recovered (bridge to recovery), patients that are eligible for transplant (bridge to transplantation), or for patients who are not transplant candidates (destination therapy). However, current rotary pumps available on the market involve also high risks of blood trauma, gastro-intestinal bleeding and consequent re-hospitalizations, because the high inertia of the continuous flow exposes the blood to high levels of shear stress and to red cell damage. Patient selection and implantation time are the most crucial factors that determine the success of LVAD therapy.

6.1.2. The Progressive Wave Pump developed in CorWave SA

CorWave SA is a biotech start-up founded in 2011 in Paris and that nowadays counts more than 50 employees, coming from bioengineering, electronic engineering, technical sciences and marketing. Its industrial activity consists in the development of new technologies for cardiac support for patients who suffered from heart failure. In particular, the core project concerns the development of a new generation of implantable blood pumps, named progressive wave pumps, which employ a new pumping mechanism based on the interaction of the blood flow with an undulating elastic membrane (Figure 6.2). The relevance of this technology is that the membrane oscillations can be tuned in order to generate an output flow with the same pulsation of the native heart. Compared to the continuous flow rotary pumps currently available on the market, the progressive wave pump presents lower scales of inner velocity and shear stress and consequently should lead to a reduced risk of blood trauma, clotting and internal bleeding. As a result, the blood pump developed in CorWave is a promising product, because it presents important advantages in terms of performance, size and costs, with respect to the competitors active in the fast-growing market of acute cardiac assist devices.

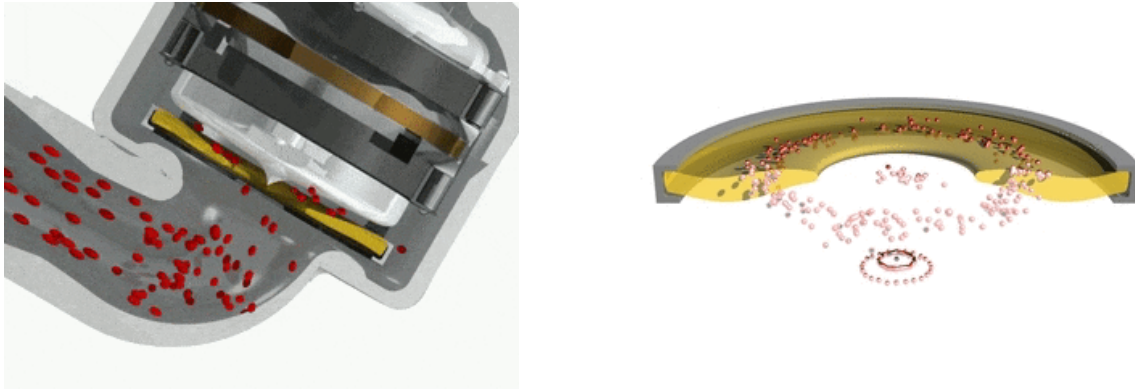


Figure 6.2: Left: Progressive wave blood pump developed in CorWave SA. Right: Detail of the blood cells gently pushed towards the inner orifice of the yellow undulating membrane. Figures included under permission of CorWave SA.

6.2. Literature and Modern Techniques

6.2.1. State-of-the-art in Blood Pumps

Heart disease is the major cause of death in the Western world and recent statistics highlighted that specifically in Europe the 47% of deaths is due to cardiovascular diseases [100]. In case of acute heart failure, heart transplantation remains the most successful long-term treatment, showing a post-transplant survival rate of 68% at the first year and a half-life of 12 years conditional on surviving at least one year [101]. However, the limited availability of healthy transplantable hearts and the uneligibility of certain patients to enter in the waiting list have required an alternative to heart transplantation. Hence, in the last decade, mechanical circulatory support systems have become a life-saving option for many patients, being a valid treatment option as bridge to transplantation or destination therapy. In addition, blood pumps proved to bring important short-term benefits as bridge to recovery, when applied on patients who suffered from reversible cases of heart disease.

Being a such promising field of application, in the last decades there has been a continuously increasing interest in research on VAD development, that has brought to several achievements in terms of size of the device (and whether it is implantable or not), its hydraulic efficiency and the risk of adverse events. In particular, Alba and Delgado [99] identified three generations or types of blood pumps:

1. Pulsatile volume displacement pumps, like pneumatic and implantable Thoratec pVAD and iVAD (Thoratec Laboratories Corp., CA, USA), HeartMate XVE (Thoratec Corp.) or LionHeart LVD2000 (Arrow International, PA, USA), which are equipped with inflow and outflow valves that allow to direct the blood dynamics inside the pump chamber in order to obtain a pulsatile output flow (see Figure 6.3, left). Even though they achieve a volume flow rate of up to 10 L/min, most of these pumps are rarely used due to the high internal inertia and the lower pulsation of the one of the native heart. In addition, these pumps are generally characterized by large volume - that makes implantation difficult and increase the risk of infections -, high incidence of malfunction and high working noise.
2. Axial continuous flow rotary pumps, like HeartMate II (Thoratec Inc.) and Jarvik 2000 (Jarvik Heart, Inc., NY, USA), which have an internal impeller suspended in the blood flow path by contact bearings, that imparts tangential velocity and kinetic energy to the blood. With respect to the pulsatile displacement pumps, they do not include inner valves and they eject blood flow in a continuous regime. Furthermore, they are characterized by smaller size, lower energy requirements and higher durability (Figure 6.3, right). On the other side, this second type of devices presents important limitations in hemolysis and thrombosis (due to the high gradients of velocity of the rotors), ventricular suction and pump stoppage. Thrombus formation can be prevented via anticoagulation, but increasing the risk of gastro-intestinal bleeding.

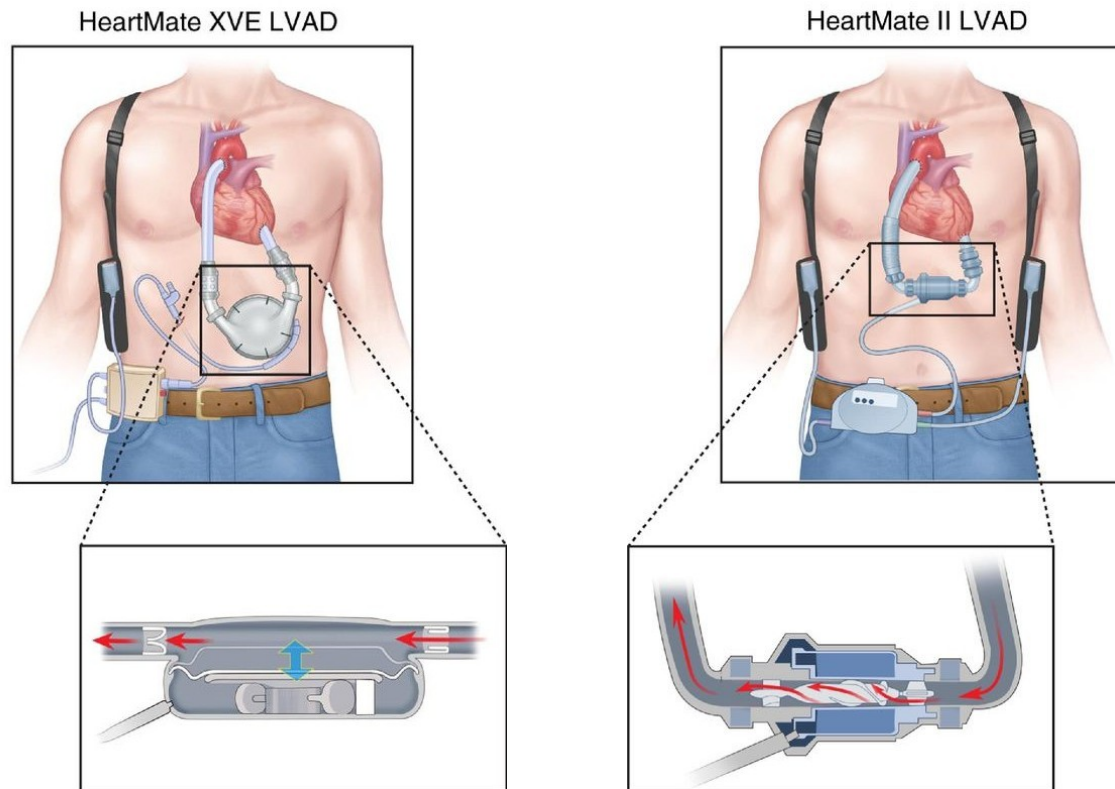


Figure 6.3: Direct comparison of the size and the mechanisms of action of a volume displacement (HeartMate XVE LVAD, left) and an axial flow rotary pump (HeartMate II LVAD, right). The displacement pump employs an electromagnetic pusher plate to cyclically change the volume of the pump chamber. The axial-flow pump uses a spinning impeller to continuously push the blood along a central shaft. Figure comes from Wilson et al., in the Journal of the American College of Cardiology [102].

- Centrifugal continuous flow rotary pumps, which differ from the axial ones because they accelerate blood circumferentially and the rotor is suspended in the blood flow path with non-contact bearing design (Figure 6.4), using either hydrodynamic levitation like VentrAssist (Ventricor Ltd., Sydney, Australia), or magnetic levitation, like DuraHeart (Terumo, Inc., MI, USA) or an hybrid system, like HVAD (HeartWare Corp., FL, USA). Thus, by avoiding any mechanical contact, they reduce energy losses by friction or heat generation, improving the durability and the reliability of the device. Nonetheless, centrifugal pumps have larger size than axial ones (especially in case of magnetically levitated impeller) and they maintain the risk of ventricular suction, blood trauma and bleeding complications because of the high speed of the rotor.

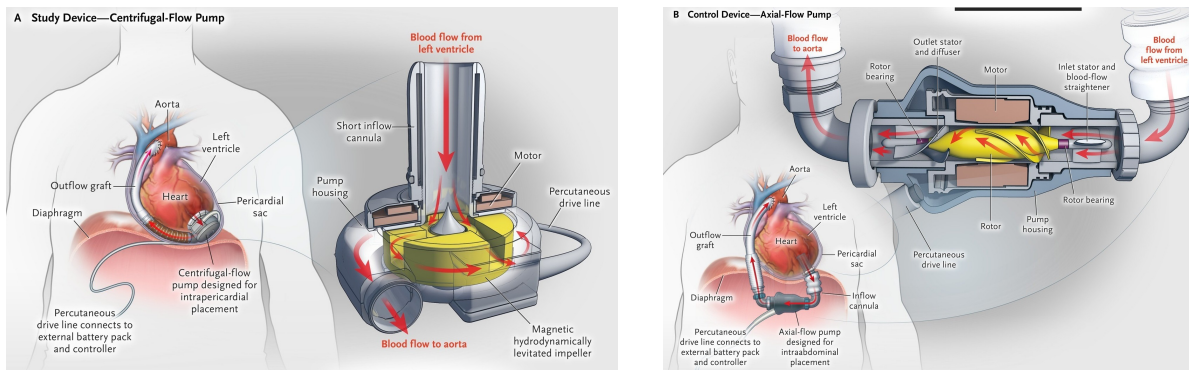


Figure 6.4: Comparison of the structure and the mechanics inside centrifugal-flow (A) and axial-flow (B) rotary pumps. The centrifugal pump pushes blood circumferentially (see red lines) using a magnetically and hydrodynamically levitated impeller; while the axial pump employs a spinning rotor mechanically sustained by contact bearing that moves the blood in axial direction. The images are taken from Rogers et al., in *The New England Journal of Medicine* [102].

Therefore, displacement blood pumps have a disadvantageous size, while rotary pumps expose the patient to high risks of hemolysis because of their rotor speed. Thus, in the last years, a new prototype of pulsatile blood pump has been projected with the intention to overcome the drawbacks of previous LVAD models by providing physiological pulsatile blood flow with a minimum risk of blood trauma. This new generation of LVADs, currently under development in CorWave SA, employs an innovative pumping mechanism that relies on the interaction between blood and an elastic polymer membrane placed between two housing walls (or flanges). Specifically, this type of pumps works as follows: a magnetic or mechanical actuator excites the deformable membrane so that it starts oscillating with a given amplitude and frequency and the resulting undulations generate progressive waves in the fluid-structure coupled system that produce an effective pulsatile pumping action. Hence, such pumps are called progressive wave pumps.

Compared with other LVAD models, progressive wave pumps are thought to provoke less trauma on the blood cells because there are no contact bearings or critical mechanical parts like rotors or valves. Furthermore, the imposed oscillations can be optimized to easily realize a pulse-modulated form with similar pulsation of the one of the native heart.

Progressive wave pumps can be realized with two different designs: discoidal wave pump and tubular wave pump. In the former case, the actuator imparts transversal oscillations on the external circumference of the membrane disc, so that the generated waving motion pushes gently the blood cells from the periphery into the inner orifice of the membrane. This is the design of the wave pump developed in CorWave. In the latter case, the overall functioning is analogous, but the membrane has a tubular shape and the direction of excitation is not radial (Figure 6.5). Although tubular wave pumps have not yet been realized, they are thought to be potentially better than discoidal ones, because of their axial pumping action and their limited space consumption [103].

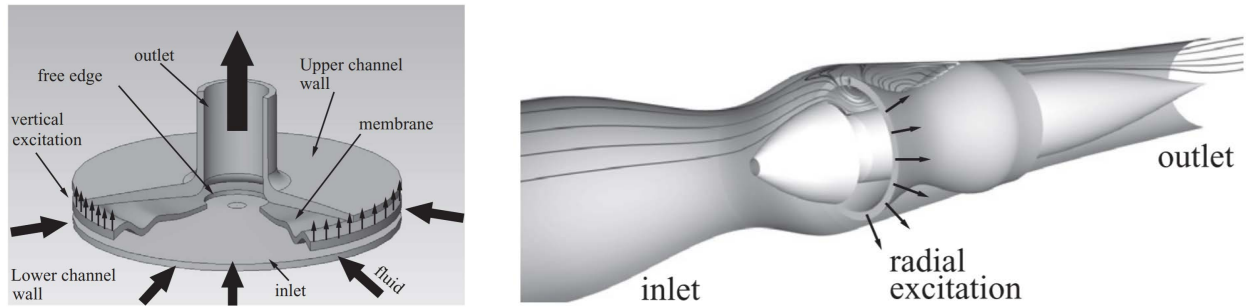


Figure 6.5: Discoidal (left) and tubular (right) design of progressive wave pumps. Illustrations taken from Perschall et al, in the Journal of Artificial Organs [103].

6.2.2. Computational Simulations as Support for LVAD Development

In order to reduce the risks underneath the usage of blood pumps, computational simulations are frequently used to reproduce the inner dynamics and investigate the causes of blood trauma [104, 105, 106]. In particular, such simulations are used to predict critical flow patterns within the pump - that may be difficult to detect experimentally -, where the blood flow develops turbulent dynamics and recirculation vortices with high inertia and stagnation time of the blood cells. In fact, these are typical factors that cause energy losses and favor adverse events, like hemolysis and thrombosis. Thus, the LVAD development team can take advantage of the valuable insights coming from simulation results to predict undesired dynamics and prevent them by properly adjusting the design of the pump.

In CorWave, they use commercial software packages like Comsol, ANSYS Fluent and ADINA, to simulate the fluid-structure interaction inside the progressive wave pump and test the effect of geometrical features (e.g. flange angle, membrane diameter, inflow area, etc.) on the global dynamics. Taking advantage of the cylindrical symmetry of the device, they perform 2D axis-symmetric simulations, in order to save computational time. However, experimental evidences highlighted that the vibrational modes of the elastic membrane do not always show a cylindrical symmetric behavior, but that there are not neglectable strain variations along the angular coordinate. Thus, in the benchmark discussed in section 6.4, the simulations will be carried out in the complete three-dimensional space, to capture the full membrane displacement.

6.3. Mathematical Modeling of the FSI problem

The dynamics inside a progressive wave pump are driven by the interaction between the blood flow and the elastic membrane. This mutual interaction can be mathematically described in the context of the Fluid-Structure Interaction (FSI) modelling, providing proper coupling conditions at the fluid-structure interface.

6.3.1. The Computational Domain

Before detailing to the mathematical formulation of the FSI problem, we need to properly define the geometry of the pump considered for the simulations.

The structure of the pump chamber is essentially divided in two parts (Figure 6.6):

1. a magnetic or mechanic actuator (red rectangle), which converts sinusoidal input currents into mechanical oscillations of the membrane disc. The transmission of the displacement to the membrane is done via a system of pins and supports of titanium - from now on this structure is called titanium holder - which ensures that the motion is uniquely in the normal direction to the membrane plan. Thus, it transforms electric power into mechanical power.
2. the pump head (green rectangle), where the blood flow interacts with the oscillating membrane before



being ejected into the aorta. Consequently, in this passage the mechanical power previously provided by the actuator is transformed into hydraulic power.

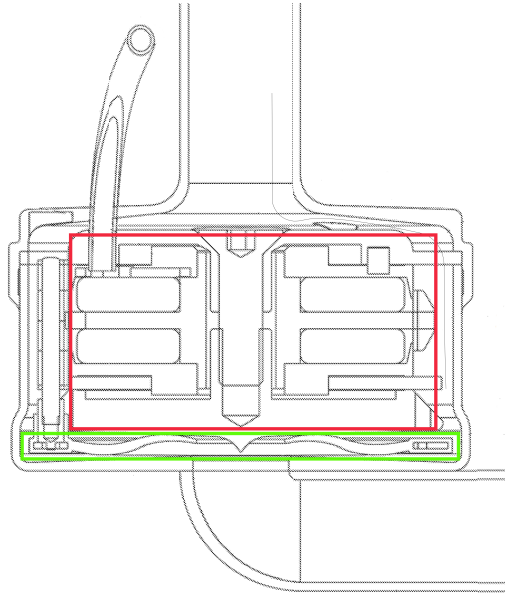


Figure 6.6: Structure of a prototype of progressive wave pump developed in CorWave. The actuator (red rectangle) imposes oscillating motion to the membrane, that interacts with the blood flow in the pump head (green rectangle). Modified version of a figure taken from CorWave licence No. WO/2017/178959, *Implantable pump system having an undulating membrane*, 19.10.2017.

For our simulations we are mainly interested in the dynamics occurring inside the pump head, where the fluid-structure interaction between the blood and the membrane leads to a pulsatile output blood flow. As a result, in this benchmark we restrict the computational domain to the sole pump head and, as we will see in the next sections, we model the mechanical effect of the actuator using proper boundary conditions applied on the membrane disc.

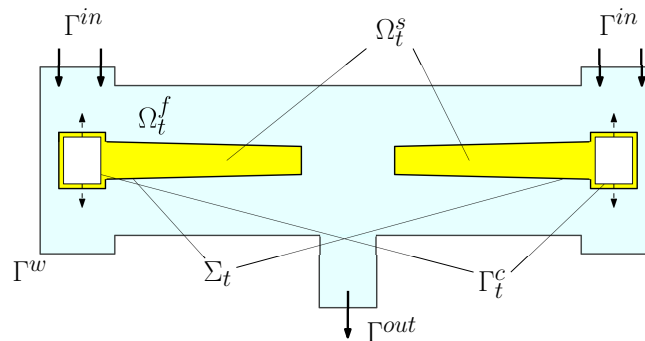


Figure 6.7: Sketch of the pump head domain.

The geometry of the pump head is sketched in Figure 6.7. The domain Ω of the pump head is the union of the fluid domain $\Omega_t^f = \Omega^f(t)$ and the structure domain $\Omega_t^s = \Omega^s(t)$, which are time-dependent because they both change in time due to the motion imposed by the actuator and the mutual interaction between the blood

fluid and the membrane structure. As a consequence, the fluid-structure interface $\Sigma_t = \Sigma(t)$ changes in time accordingly. Thus, we have $\Omega = \Omega_t^f \cup \Omega_t^s$ and $\Sigma_t = \Omega_t^f \cap \Omega_t^s$, $\forall t \geq 0$.

The boundary of the pump housing $\partial\Omega$ is composed by the following subportions:

- the inlet boundary Γ^{in} , where the blood fluid enters in the computational domain;
- the output boundary Γ^{out} , where the blood is ejected from the pump chamber into the outflow cannula;
- the boundary of the inner titanium cavity Γ_t^c , that corresponds to the border of the space occupied by the titanium holder inside the membrane and that transmits to the former the oscillating motion prescribed by the actuator;
- the wall boundary Γ^w , which consists of all the remaining parts of the pump housing, including flanges and steps; i.e. we have $\Gamma^w = \partial\Omega \setminus (\Gamma^{in} \cup \Gamma^{out} \cup \Gamma_t^c)$.

The position of the boundary of titanium cavity Γ_t^c changes in time, oscillating along the vertical direction z together with the membrane, whereas the frontier of the domain $\partial\Omega$ is fixed in time.

Notice that, with respect to the description of the pump geometry in the previous paragraph, we omit the titanium holder structure in the computational domain. This is justified by observing that its movement is purely rigid. Thus, since the movement is determined by the actuator, its effect on the membrane can be modeled by means of a Dirichlet boundary condition directly on the boundary Γ_t^c .

6.3.2. Formulation of the FSI Problem

In the context of Fluid-Structure Interaction problems, the dynamics are represented by a system of Partial Differential Equations (PDEs) which describe separately the behaviour of the fluid and of the structure in the respective domains, while coupling conditions define their interaction at the interface.

Thus, FSI problems are instances of hierarchical or multilevel model, which have two basic components: the fluid dynamics model and the structure model (Figure 6.8). On one side, the blood fluid is modeled using Navier-Stokes Equations (NS), which correspond to the conservation laws of mass and momentum for an incompressible viscous newtonian fluid. On the other side the membrane motion is mathematically represented through the elasto-dynamics equations. Finally, the two subproblems are coupled at the interface between blood and membrane to impose the continuity of velocity and of traction forces. This is indicated in the literature as physical coupling of the system. Furthermore, the problem presents an additional coupling condition, due to the mutual dependancy of the domains. In fact, the structure displacement does not only determine the position of the structure domain Ω_t^s , but it determines also the configuration of the fluid domain Ω_t^f by means of a perfect adherence condition between the two subdomains holding at the interface (geometrical coupling).

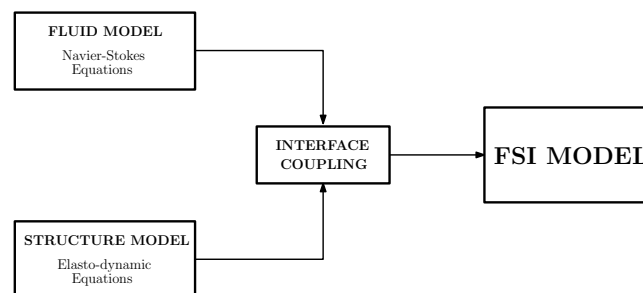


Figure 6.8: Multi-level representation of the Fluid-Structure Interaction building blocks.

Specifically, the FSI problem reads as follows: for each time $t > 0$, find fluid velocity and pressure $(\mathbf{u}(t), p(t))$:

$\Omega_t^f \times \Omega_t^f \rightarrow \mathbf{R}^3 \times \mathbf{R}$ and membrane displacement $\hat{\mathbf{d}}(t) : \hat{\Omega}^s \rightarrow \mathbf{R}^3$, such that:

$$\begin{cases} \rho_f (\partial_t \mathbf{u} + \mathbf{u} \cdot \nabla \mathbf{u}) - \nabla \cdot \mathbf{T}^f(\mathbf{u}, p) = \mathbf{0} & \text{in } \Omega_t^f, & (6.1a) \\ \nabla \cdot \mathbf{u} = 0 & \text{in } \Omega_t^f, & (6.1b) \\ \rho_s \partial_{tt} \hat{\mathbf{d}} - \nabla \cdot \hat{\mathbf{T}}^s(\hat{\mathbf{d}}) = \mathbf{0} & \text{in } \hat{\Omega}^s, & (6.1c) \\ \mathbf{u} = \partial_t \hat{\mathbf{d}} & \text{on } \Sigma_t, & (6.1d) \\ \mathbf{T}^f(\mathbf{u}, p) \mathbf{n}^f = -\mathbf{T}^s(\hat{\mathbf{d}}) \mathbf{n}^s & \text{on } \Sigma_t & (6.1e) \end{cases}$$

where Ω_t^f depends through the geometrical coupling on the displacement \mathbf{d} , i.e. $\Omega_t^f = \Omega_t^f(\mathbf{d})$. Here, ρ_f and ρ_s are the mass densities of fluid and structure, \mathbf{n}^f and \mathbf{n}^s are the external normal vectors from fluid and structure domains, satisfying $\mathbf{n}^f = -\mathbf{n}^s = \mathbf{n}$, $\mathbf{T}^f(\mathbf{u}, p) = -p\mathbf{I} + 2\mu_f \mathbf{D}(\mathbf{u})$ is the Cauchy stress tensor for a viscous newtonian fluid with viscosity μ_f and symmetric operator $\mathbf{D}(\mathbf{w}) = \frac{1}{2}(\nabla \mathbf{w} + \nabla \mathbf{w}^T)$, and $\hat{\mathbf{T}}^s(\hat{\mathbf{d}})$ is the first Piola-Kirchhoff tensor of the structure, such that $\hat{\mathbf{T}}^s(\hat{\mathbf{d}}) = J \mathbf{T}^s(\mathbf{d}) \mathbf{F}^{-T}$ with \mathbf{T}^s being the solid Cauchy stress tensor, $\mathbf{F} = \nabla \mathbf{x}$ the gradient of deformation and $J = \det \mathbf{F}$ its determinant.

In line with standard continuum mechanics theory, the fluid problem has been posed in an Eulerian framework, whereas the structure problem has been formulated in a Lagrangian framework, indicating with superscript $\hat{\cdot}$ the quantities in the reference configuration at time 0, i.e. in $\hat{\Omega}^s = \Omega_0^s$. In case we assume that the material is linearly elastic and isotropic the solid stress tensor $\mathbf{T}^s(\mathbf{d})$ can be explicitly written using the Hooke's law as $\mathbf{T}^s(\mathbf{d}) = \lambda_s (\nabla \cdot \mathbf{d}) \mathbf{I} + 2\mu_s \mathbf{D}(\mathbf{d})$ where $\lambda_s, \mu_s > 0$ are the Lamé parameters of the elastic material.

Finally, the problem is closed with proper initial conditions, e.g. imposing null fluid and structure velocity and membrane displacement, and the following boundary conditions:

$$\begin{cases} \mathbf{u} = \mathbf{u}_{in} & \text{on } \Gamma^{in}, & (6.2a) \\ \mathbf{T}^f(\mathbf{u}, p) \mathbf{n}^f = \mathbf{0} & \text{on } \Gamma^{out}, & (6.2b) \\ \mathbf{u} = \mathbf{0} & \text{on } \Gamma^w, & (6.2c) \\ \mathbf{d}(t) = \Phi \sin(2\pi f t) \mathbf{e}_z & \text{on } \Gamma_t^c & (6.2d) \end{cases}$$

Notice that the forcing terms in the dynamics of the coupled problem are given by the inlet velocity \mathbf{u}_{in} and by the vibrations induced by the actuator, with predefined frequency f and amplitude (or stroke) Φ .

6.4. Benchmark Plan

The FSI modeling approach illustrated in Section 6.3 describes the mutual interaction between the blood fluid and the oscillating membrane that arise inside the progressive wave pump developed in CorWave. Therefore, such model has to be validated against real data provided by the company, in order to understand whether the simulation results can be actually used to predict the inner dynamics and optimize the design of the pump geometry accordingly. Thus, the benchmark consists of an experimental-based validation of the FSI model, with a similar approach to the one used in [103].

6.4.1. Description of Real Data

The experimental data that can be used for model validation come from measurements of physical quantities related to the blood flow, pressure, membrane displacement and force. Specifically, CorWave can provide the following experimental data:



- measurements of the volume flow rate Q , made with an ultrasonic flowmeter clamped at the inlet of the testing pipes, with a sampling rate of 10 Hz;
- pressure data P , obtained with pressure sensors placed at the inlet and the outlet in order to measure the pressure rise ΔP inside the pump;
- based on the fact that CorWave developed a mechanical actuator that mimics the implantable pump, a strain gauge force sensor placed below the membrane can measure the force necessary to impose a sinusoidal displacement on the membrane holder;
- displacement values are available for both the active part of the membrane as well as the membrane holder. In particular the motion of the active part of the membrane is acquired with a high speed camera, while the displacement of the membrane holder is recorded through a laser.

In addition, cross data can be derived from the raw measurements described above. These include hydraulic power and efficiency, PQ and HQ curves, oscillation frequency, membrane position in time and membrane cross section versus time.

In particular, one of the main goals in CorWave is to maximize the hydraulic efficiency η_h of the pump. In fact, this parameter measures the efficiency of the device to transform the mechanical power W coming from the actuator into hydraulic power H :

$$\eta_h = \frac{H}{W} = \frac{\Delta P Q}{\frac{\int_a^b F dx}{\Delta T}} \quad (6.3)$$

where the hydraulic power H of the pump is computed as the product of the pressure difference ΔP between inlet and outlet and the ejected volume flow rate Q and the integral of F corresponds to the mechanical work of the actuator to move the membrane from position a to position b in a time interval ΔT .

Furthermore, PQ or HQ curves are standard data representations used to study the performance of the pump and to validate the FSI model. In these relationships, the pressure rise (here denoted simply as P) or the hydraulic power (H) are related with each output volume flow rate (Q). In CorWave, such curves are obtained for different frequencies f of mechanical excitation of the elastic membrane, varying in a range between 60 Hz until up to 120 Hz.

Notice that testing in CorWave is performed on a mix of water and glycerin (39% in weight) at 37 °C in order to mimic the blood density and viscosity.

6.4.2. Validation of the FSI Model

The goal of the benchmark is to validate the FSI model against the real experimental data detailed in the previous paragraph.

A first point of our validation analysis is to compare the PQ (or HQ) curves obtained by the numerical results with the experimental pump characteristic curves. In Figure 6.9, there are the results of this type of comparative study for model validation, performed by Perschall et al. [103]. In the left panel of Figure 6.9, we see the comparison between the numerical results (circles) and the experimental findings (dots) for different input frequencies of membrane oscillation (80, 90, 100 and 110 Hz). Since there is a systematic discrepancy between the curves, the authors propose a linear correction function for the numerical values in order to compute modified values of the pressure (squares) that are in a better agreement with the data. In the right panel of Figure 6.9, the model is validated also across different geometries of the pump. In fact, the numerical simulations are carried out for two different geometries, the reference one (dashed line) and a slightly modified version of it (solid line), and two different input frequencies (80 and 100 Hz).

In our benchmark we want to adopt a similar validation strategy: compare the pump characteristic PQ (or HQ) curves obtained from simulations and from experiments to validate the FSI model, so that it can be used to test pump geometries with different domain and model parameters. Specifically, example of feature parameters that we are interested to vary in our simulations are:



- the angle of the pump flanges,
- the length of the vertical separation between the flanges (said gap),
- the stroke of the membrane oscillations,
- the membrane diameter,
- the inflow area,
- the outflow area.

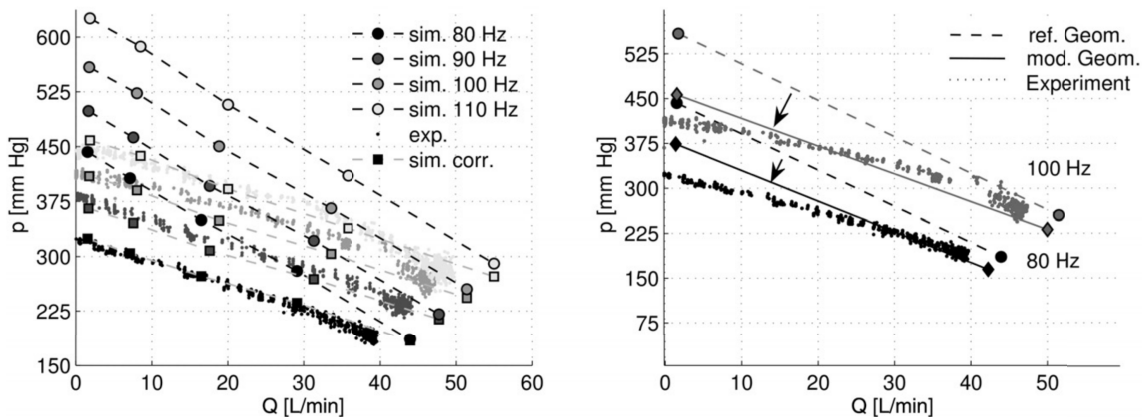


Figure 6.9: Example of validation of FSI model inside a progressive wave blood pump with discoidal structure, taken from Perschall et al. [103]. Left: Comparison of simulation results for different frequencies (sim: circles) with experimental PQ curves (exp: dots). Square symbols correspond to modified simulation results (sim. cor.), obtained by the application of the linear correction function $p_{corr} = a p + b Q$ in order to mimic better the experimental data. $a = 0.73$, $b = 1.5 \cdot 10^{-5}$ bar/(L/min). Right: Similar comparative study performed for two oscillation frequencies on two different geometries of the pump, the reference one (ref. Geom.: dashed line) and a similar one where the angle and the height of the channel are slightly changed (mod. Geom.: solid line).

A second important point of our model validation of the progressive wave pump is based on the information coming from the membrane displacement. In particular, the spatial coordinates of the membrane position in time obtained by the recordings will be compared with the simulated displacement predicted by the FSI model. Moreover, since the implemented simulations are going to be carried out in the full three-dimensional space, the validation will specifically address the three-dimensional modes of deformation, comparing the recordings with simulation results.

Finally, the benchmark will also include a comparison of the performance of our implementation with the bi-dimensional axis-symmetric simulations performed in COMSOL currently employed in CorWave, in terms of both accuracy and computational efficiency.

The FSI simulations for the benchmark will be performed using an advanced numerical approach, named Extended Finite Element Method (X-FEM) [107, 108], that is briefly explained in the Appendix A.1. The implementation will be carried out in the LIBRARY of Finite Elements V (LIFEV) [109], an academic library that is particularly suitable for cardiovascular applications and has been developed by MOX-PoliMi (Milan), CMCS-EPFL (Lausanne), ESTIME-INRIA (Paris) and E(CM)2-Emory University (Atlanta).



Part VII.

Benchmark case in thermo-hydro-mechanical phenomena arising in blast furnaces

Nirav Shah, Gianluigi Rozza, Peregrina Quintela, Patricia Barral, Michele Girfoglio

Abstract

The high temperature process occurring inside blast furnace hearth and correspondingly high thermal stresses induced in blast furnace walls pose significant challenge for mechanical design. We present here steady state thermo-mechanical coupled model to numerically compute thermal stresses. The model involves classical equations of energy conservation and momentum conservation from continuum mechanics. In the present report, axisymmetric formulation consisting of conduction heat transfer and momentum conservation is considered. Further, the domain considered is isotropic and homogeneous. Subsequently, separate benchmark cases for each individual model complexity ensure step by step error resolution. At the end of the report, envisioned roadmap for reduced basis method and computation is presented. These methods are aimed at quick and reliable transfer of numerical results to real industrial problem. Additionally, model hierarchy for full order model, taking into account practical complexities, gives future extensions from the current simplified model.

Keywords: Blast furnace hearth, thermo-mechanical coupled model, finite element method, reduced basis method, multiphysics problem, benchmark verification.

7.1. Conceptual model

Blast furnace is a metallurgical furnace used to produce iron from "charge". The "charge" contains iron ore, limestone and coke. The process requires high temperature to increase rate of oxidation of carbon, an exothermic reaction. In the hearth the hot air, supplied through Tuyere, acts as source of oxygen and is used for oxidation of carbon. The temperature in the hearth is as high as 1500°C. The general layout of blast furnace is shown in Figure 7.1.



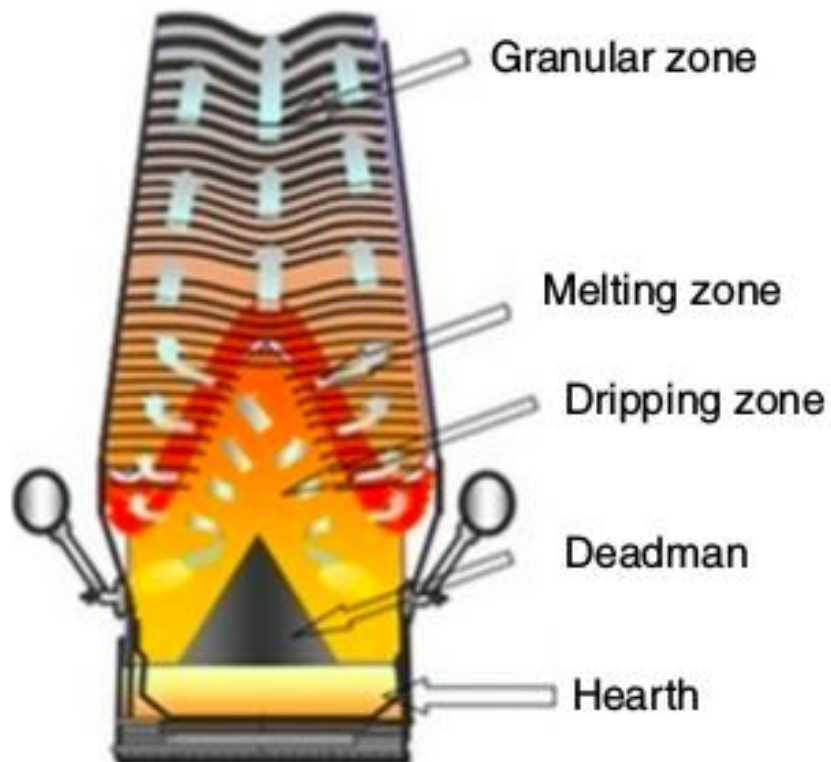


Figure 7.1: Blast furnace divided in zones [110]

As mentioned by Swartling M. et. al. [111] the hearth is made up of several refractory zones (Figure 7.2), with each zone having specific function and accordingly, design requirements. The outside of the hearth is covered with a steel shell (Figure 7.2). The wall and bottom are constructed by five types of refractory materials, each with its specific properties depending on type of environment the region is exposed to. The wall is made up of carbon material having relatively high heat conductivity to keep the inner wall at a low temperature. The upper layer of the bottom is a ceramic plate with the composition 23.5 % SiO_2 , 73.5 % Al_2O_3 and some additives. It has high resistance to mechanical wear, which helps to keep the bottom layer intact and avoid cracks. That is important to avoid penetration and solidification of liquid iron in the lower bottom layers, since this would have impact on the heat flow. Between the steel shell and the bottom refractory is a layer of ramming paste. The taphole region is made up of carbon refractory. It has very high heat conductivity to transport heat from the taphole during tapping and reduce the thermal stresses in the region.

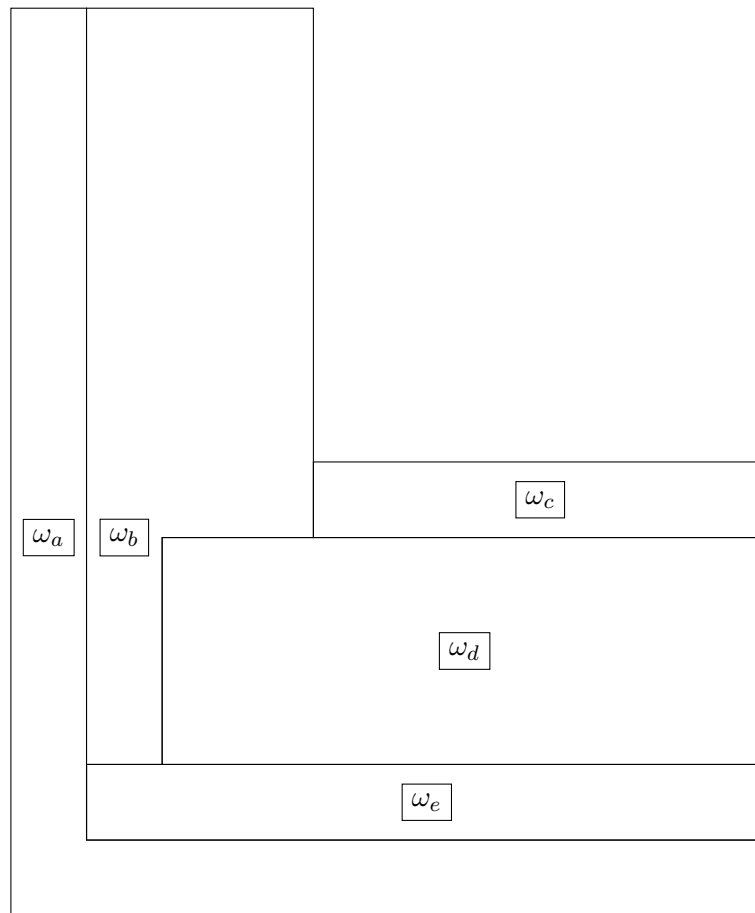


Figure 7.2: Scheme of Hearth axisymmetric geometry ω : ω_a) Steel shell, ω_b) Carbon wall, ω_c) Ceramic plate, ω_d) Lower bottom layer, ω_e) Ramming paster [111]

The proper materials selection ensures less heat loss and also less thermal stresses. Minimising the thermal stresses and the mechanical effects of the hot metal flow constitute a design challenge. The wall of the hearth is subjected also to abrasive wear due to oxidation, abrasion/deterioration due to chemical attack and erosion due to hot liquid flow. The heat transfer through the furnace wall is due to conduction process, and through the region of fluid flow is due to convection process.

7.2. Practical significance of the project

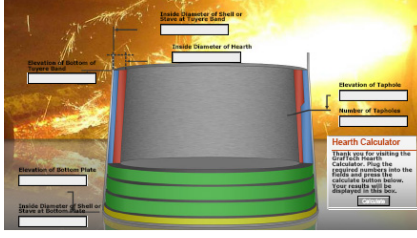
Wear of carbon refractory limits the hearth lifetime, which in turn restricts lifetime of blast furnace. An optimum design enlarges the hearth lifetime and consequently, the blast furnace campaign. Among different families of design, the most commonly used is considered in this work.

The design parameters which affect the hearth design are material properties, operating conditions and geometric dimensions. If carbon blocks are used, frictional contact could occur between block surfaces. Other materials used are ceramic cup bricks or castable material for ramming mix. The parameters related to geometry of hearth such as thickness of hearth material are of interest for geometric parametrization (Figure 7.4).

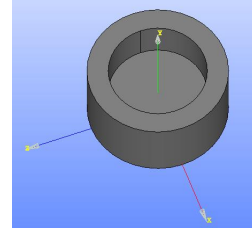
The benchmark cases introduced in this document correspond to some thermo-mechanical models arising in the blast furnace hearth, and are based on the extensive experience of Global Research and Development Center of ArcelorMittal in Asturias, Spain. The project is carried out under able supervision from ITMATI and SISSA.

7.3. Mathematical model

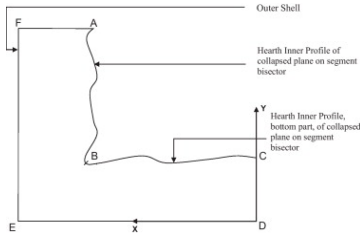
The governing equations for thermo-mechanical modelling are linear momentum conservation and energy conservation from continuum mechanics.



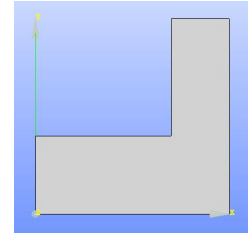
(a) 3 Dimensional hearth geometry [112]



(b) Hearth 3 dimensional computational domain



(c) Axisymmetric hearth geometry [113]



(d) Hearth axisymmetric computational domain

Figure 7.3: Hearth geometry and computational domain

The mathematical model is based on the following assumptions which lead to reasonable simplifications :

1. The model is assumed to be axisymmetric. Taphole operation is not part of this study, i.e. only normal operating conditions are considered.
2. We only focus on the steady state operations.
3. At first iteration hearth is made up of single material and is isotropic. After successful benchmark tests anisotropy and inhomogeneity will be considered.
4. Initially linear elasticity, heat transfer only by conduction within hearth walls and by convection with surrounding and no contact between bricks are considered. After successful benchmark tests of simplified models, the following non linearities will be considered : Contact between refractory blocks, radiation heat transfer and material property dependence on temperature.

We describe the circular cross section of blast furnace by r, θ and vertical axis of blast furnace by y (cylindrical coordinate system). We introduce now simplified 3-dimensional domain Ω , corresponding to the solid part of the hearth, in cylindrical coordinates as $\omega \times [0, 2\pi)$. Ω refers to 3-dimensional computational domain and its vertical section ω , refers to axisymmetric computational domain (Figure 7.3). We denote the boundary of Ω as $\partial\Omega$ and the boundary of ω as $\partial\omega$. Let r_0 be the outer radius of Ω and y_{min}, y_{max} are its minimum and maximum y -coordinates respectively. We represent \vec{e}_y, \vec{e}_r and \vec{e}_θ , the unit vectors corresponding to y -, r - and θ - directions respectively. \vec{n} is the unit normal vector pointing outwards. We use the following notations for boundaries of Ω (Figure 7.4).

$$\begin{aligned} \Gamma_{out} &= \partial\Omega \cap (r \equiv r_0) , \\ \Gamma_+ &= \partial\Omega \cap (y \equiv y_{max}) , \\ \Gamma_- &= \partial\Omega \cap (y \equiv y_{min}) , \\ \Gamma_{sf} &= \partial\Omega \setminus (\Gamma_{out} \cup \Gamma_+ \cup \Gamma_-) . \end{aligned}$$

The corresponding two dimensional boundaries of ω are denoted using γ instead of Γ (Figure 7.4). Notice that a new boundary appears on the axi-symmetric domain:



$$\gamma_s = \partial\omega \cap (r \equiv 0) .$$

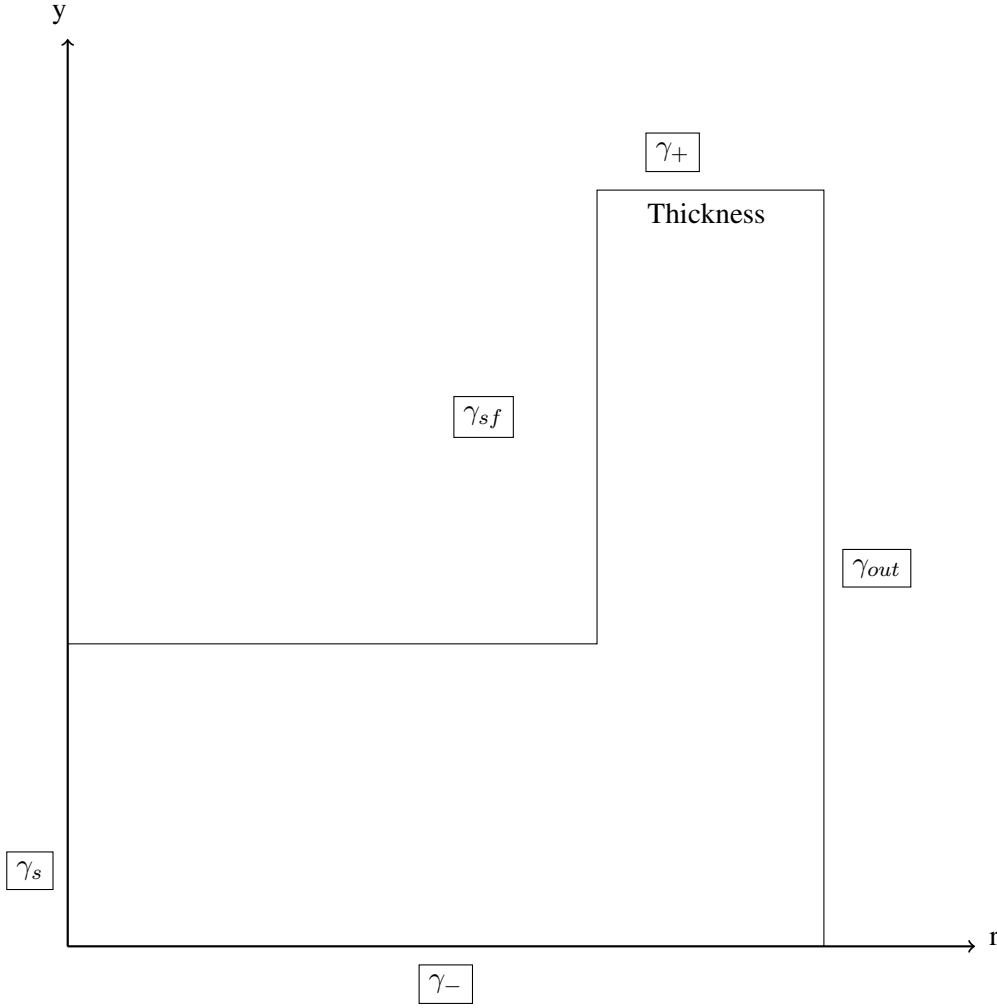


Figure 7.4: Boundaries of axis-symmetric computational domain

Based on the assumptions listed above, the momentum conservation (for small displacements) and energy conservation can be written as,

$$-Div(\boldsymbol{\sigma}) = \vec{0} \text{ in } \Omega , \quad (7.1)$$

$$-Div(\mathbf{K}\nabla T) = 0 \text{ in } \Omega . \quad (7.2)$$

Here \mathbf{K} refers to thermal conductivity tensor, $\boldsymbol{\sigma}$ refers to stress tensor, and $T = T(r, \theta, y)$ refers to temperature. The stress tensor $\boldsymbol{\sigma}$ is related to strain tensor through Hooke's law:

$$\boldsymbol{\sigma}(\vec{u}) = \lambda \text{Tr}(\boldsymbol{\epsilon}(\vec{u}))\mathbf{I} + 2\mu\boldsymbol{\epsilon}(\vec{u}) - (2\mu + 3\lambda)\alpha(T - T_0)\mathbf{I} , \quad (7.3)$$

where \mathbf{I} refers to the identity tensor, strain tensor $\boldsymbol{\epsilon}(\vec{u})$ is defined as,

$$\boldsymbol{\epsilon}(\vec{u}) = \frac{1}{2}(\nabla\vec{u} + \nabla\vec{u}^T) , \quad (7.4)$$



\vec{u} being the displacement vector,

$$\vec{u} = u_r(r, \theta, y)\vec{e}_r + u_\theta(r, \theta, y)\vec{e}_\theta + u_y(r, \theta, y)\vec{e}_y, \quad (7.5)$$

T_0 is the reference temperature, α is the thermal expansion coefficient, and λ and μ are the Lamé parameters of the material. The latter can be expressed in terms of Young modulus, E , and the Poisson ratio, ν as:

$$\mu = \frac{E}{2(1+\nu)}, \quad \lambda = \frac{E\nu}{(1-2\nu)(1+\nu)}. \quad (7.6)$$

On the upper boundary (Γ_+), the weight of other blast furnace components is acting and no conduction heat transfer are considered :

$$\begin{aligned} (-\mathbf{K}\nabla T) \cdot \vec{n} &= 0, \\ \vec{\sigma}_t &= \vec{0}, \sigma_n = |\vec{W}_s|, \end{aligned} \quad (7.7)$$

where \vec{W}_s is the weight from other furnace components supported by hearth walls, $\vec{\sigma}_t$ and σ_n are tangential and normal forces :

$$\begin{aligned} \sigma_n &= (\boldsymbol{\sigma} \vec{n}) \cdot \vec{n}, \\ \vec{\sigma}_t &= \boldsymbol{\sigma} \vec{n} - \sigma_n \vec{n}. \end{aligned}$$

On the bottom boundary (Γ_-), the temperature is assumed to be known, the normal displacement is null and shear force is assumed to be zero, therefore on this boundary,

$$\begin{aligned} T &= T_D, \\ \vec{u} \cdot \vec{n} &= 0, \vec{\sigma}_t = \vec{0}. \end{aligned} \quad (7.8)$$

On inner boundary (Γ_{sf}), a convection heat transfer with the liquid phase occurs and hydrostatic pressure is acting :

$$\begin{aligned} (-\mathbf{K}\nabla T) \cdot \vec{n} &= \alpha_f(T_f - T), \\ \boldsymbol{\sigma} \vec{n} &= -p_h \vec{n}, \end{aligned} \quad (7.9)$$

where T_f is the fluid temperature assumed to be constant at the steady state, α_f the convective heat transfer coefficient, and p_h is the hydrostatic pressure computed as:

$$p_h = \rho_f g h, \quad (7.10)$$

being ρ_f the mass density of the fluid, g the gravitational acceleration, and h height of fluid column.

On outer boundary (Γ_{out}), convective heat flux and no deformation in radial direction are assumed :

$$\begin{aligned} (-\mathbf{K}\nabla T) \cdot \vec{n} &= \alpha_{out}(T_{out} - T), \\ \vec{u} \cdot \vec{n} &= 0, \vec{\sigma}_t = \vec{0}, \end{aligned} \quad (7.11)$$

α_{out} being the heat transfer coefficient, and T_{out} the ambient temperature.

It can be observed that the introduced model (boundary conditions, body forces and heat source term) is independent of θ and hence an axisymmetric model hypothesis is applicable. The axisymmetric model leads to significant computational savings as the 3-Dimensional model in (r, y, θ) can now be described by only



2-coordinates (r, y) . In this axisymmetric system, we represent the displacement \vec{u} and temperature T , both independent of θ as,

$$\begin{aligned}\vec{u} &= u_r(r, y)\vec{e}_r + u_y(r, y)\vec{e}_y, \\ T &= T(r, y).\end{aligned}\tag{7.12}$$

The associated axisymmetric model is reduced to consider conservation equations (7.1), (7.2) and boundary conditions (7.7), (7.8), (7.9) and (7.11) replacing the Ω domain by its vertical section ω , and the Γ boundaries by γ such that $\Gamma = (\gamma \setminus \gamma_s) \times [0, 2\pi)$, adding the usual condition of symmetry over γ_s :

$$(-\mathbf{K}\nabla T) \cdot \vec{n} = 0, \vec{u} \cdot \vec{n} = 0, \vec{\sigma}_t = \vec{0} \text{ over } \gamma_s.\tag{7.13}$$

7.4. Numerical model

The finite element based simulation of coupled thermo mechanical system arising in blast furnace is well known in various scientific literatures such as [114]. It solves energy and momentum conservation equation. The model is considered steady and the bricks as isotropic and homogeneous.

The thermo mechanical behavior for blast furnace hearth lining was also investigated by Brulin et. al. [115] based on the modified Cam-Clay material model using Finite Element Method. This approach takes into account non linear elastic and plastic behavior. It introduces a yield function and plastic state based on an assumed yield function.

Kaymak [116] introduced a fast and simplified contact model for blast furnace hearth thermo-mechanical behavior simulation. This model uses the fact that contact occurs under compression whilst during tension there is no contact. This eliminates tensile stresses between contacts.

Different softwares packages are available for the simulation such as ANSYS (<https://www.ansys.com/>), Code_Aster [117] or FEniCS [23]. We plan to use Code_Aster [117] which is an open access software developed for analysis of structures and thermomechanics for studies and research. During benchmark tests we compare the solutions provided by Code_Aster against solution provided by FEniCS [23].

The basic workflow for solving coupled thermo mechanical problem involves solving the energy equation first to get the values of temperature at the degrees of freedom. Their temperature values are then inserted into the momentum conservation equation to compute the effects related to thermal stresses (Figure 7.5).



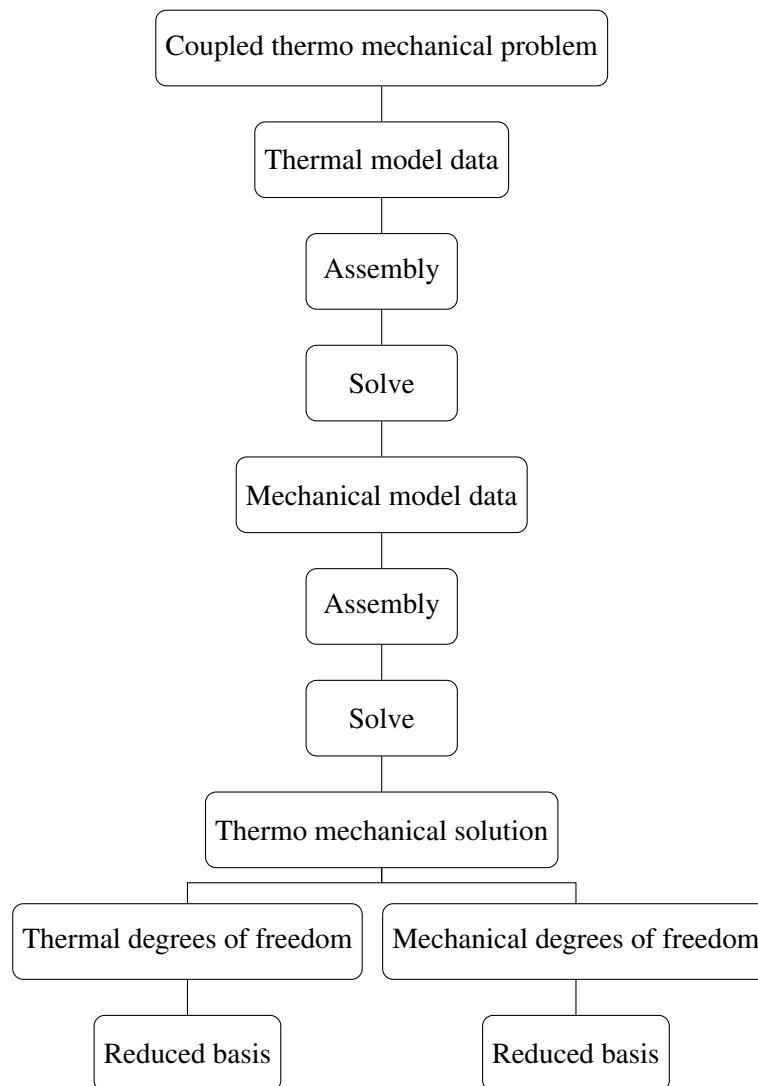


Figure 7.5: Workflow for numerical simulation of thermo-mechanical coupled system

7.5. Parametrization

The parameters of interest are thermal and mechanical properties of the material and geometric variations i.e. geometric parameters.

The relevant material properties for mechanical design are Lamé parameters or equivalently, Young's modulus and Poisson's ratio or shear modulus. From thermal design point of view thermal conductivity and convective heat transfer coefficients are relevant.

The geometric parameters for the current problem are thickness of hearth lining. Depending on the design adopted the geometry and accordingly geometric parameters could considerably change.

7.6. Model order reduction

Model order reduction (MOR), also known as reduced basis methods, for multiphysics problems have recently gained attention within model order reduction community. The projection based methods are well established for many problems, however, preservation of block structure and/or preservation of passivity of original system has given rise to different approaches. The challenge is to transfer these favorable properties from full order model to reduced order model. We discuss below several methods for model order reduction. A careful assess-



ment will be made after implementation and verification of the simulation using a finite element method for the present problem. If required, comparison will be made between different approaches. It should be noted that reduced order solution is calibrated against full order solution, which in turn is compared against benchmark solution. Therefore, separate benchmark problem for reduced basis solution is not necessary. As discussed in section 7.7, established reduced basis library RBniCS (<http://mathlab.sissa.it/rbnics>, [118]) is foreseen to be used.

We discuss now some multiphysics reduced basis methods. For further details, we refer to [119].

7.6.1. Standard Krylov subspace method

A system of the form $Ax = b$ with $A \in \mathbb{R}^{m \times m}$, $x \in \mathbb{R}^m$, $b \in \mathbb{R}^m$, and $r_k = Ax - b$, with $r_k \in \mathbb{R}^m$ and k being the number of iteration of solver, the n -dimensional standard Krylov subspace \tilde{V} is created by,

$$\tilde{V} = \mathcal{K}_n(A, r_0) = \text{colspan}\{r_0, Ar_0, A^2r_0, \dots, A^{n-1}r_0\}. \quad (7.14)$$

The standard Krylov subspace method, however, is not structure preserving and hence one loses the original matrix structure in reduced basis space [119]. In some structure preserving methods the Krylov subspace method is modified in order to preserve the block matrix structure of the original system. The moment matching property is realized by projecting the original system matrices onto the appropriate input and output based Krylov subspaces [119].

7.6.2. Order reduction by projection

In this method the original matrix A is reduced by projecting onto its subspace with matrix V ,

$$\tilde{A} = V^T A V. \quad (7.15)$$

As pointed out by Freund [120], the projection approach preserves the passivity of the original system.

7.6.3. Structure-Preserving Reduced-order Interconnect Macromodelling (SPRIM)

The main computational step in SPRIM is identical to PRIMA : Passive reduced-order interconnect macromodelling algorithm [121]. This step aims at creating n -dimensional Krylov subspace $\mathcal{K}_n(A, r)$. The PRIMA method creates the reduced basis space using matrix \tilde{V} (equation (7.14)) containing orthonormal basis for the Krylov space. The strong advantage of this method is preservation of stability and passivity of the original system [122]. In SPRIM, the vectors in matrix \tilde{V} are placed diagonally in matrix \tilde{V}_{sprim} and matrix \tilde{V}_{sprim} is used in place of \tilde{V} .

7.7. Problem characteristics and Benchmark cases

Based on the description in conceptual and mathematical model, the following characteristics problems need to be tested with benchmark cases. Full order simulation is performed by Code_Aster [117] (www.code-aster.org). Additionally, for benchmark comparison, full order simulation will also be performed by FEniCS [23] (<https://fenicsproject.org/>) and/or ANSYS (www.ansys.com). For reduced basis simulation routines from RBniCS [118] (www.mathlab.sissa.it/rbnics) will be used. The assembled matrices from Code_Aster will be used in compatibility with individual RBniCS modules.

We propose separate benchmark cases for each individual characteristic for step by step error resolution. After successful analytical numerical tests, a benchmark problem will be verified with experimental data from industrial partner. The data here refers to temperature measurement by thermocouples, strain gauge measurements and / or stress gauge measurements based on practice followed by industrial partner such as [123].



7.7.1. Energy equation

As mentioned in solution workflow (Figure 7.5), first energy equation is solved. A known analytical temperature function and source term function will be applied. Temperature at each degree of freedom computed with Code_Aster will be compared with Temperature computed with FEniCS and/or ANSYS for the same problem.

7.7.2. Momentum equation

We apply analytical stress function, such as known spherical stress tensor or known shear stress on the domain and compare results provided by FEniCS and ANSYS with Code_Aster simulations.

7.7.3. Coupling

We apply known spherical stress test in the domain. In another test, we subject the domain to only thermal stress. When the domain is subjected to combined effect of known spherical stress test and thermal stress, the principal stresses should be the sum of spherical stress and thermal stress.

7.7.4. Condition number

Due to large difference between order of magnitude of thermal conductivity and that of material parameters such as Young's modulus, the coupled stiffness matrix might have bad condition number. However, as the equations are solved sequentially, the coupled stiffness matrix is not required to be assembled and hence, condition number is not expected to be a major problem.

7.8. Future work

The simplified model introduced here will be modified to consider practical complexities. Specifically, radiation heat transfer and non linear material behavior will be simulated and tested. After simulating this non linear model, the contact between refractory blocks will be simulated and verified with benchmark tests. The model will include necessary complexities and verified with experimental data. Accordingly, benchmark tests will be modified for the verification of simulations with benchmark problems.



Part VIII.

Benchmark Case for Optimal Shape Design of Air Ducts in Combustion Engines

Naomi Auer, Michael Hintermüller, Karl Knall

Abstract

In order to optimize the shape design of air ducts in combustion engines, we consider a free form shape optimization problem subject to the Navier-Stokes equations. The associated numerical solution requires an efficient computation and yet accurate approximation of an adjoint-based shape gradient and also elements of higher order in a shape-gradient-related descent method for high Reynolds number flows. Moreover, geometric constraints need to be taken care of. As a benchmark case for the described problem, we propose a curved duct geometry with one inlet and one outlet which is inscribed in a restrictive design space. The geometry has been developed together with engineers from the automotive industry.

Keywords: Shape optimization, Navier-Stokes equations.

8.1. Introduction

Many optimal design problems in engineering or biomedical sciences require to determine an optimal shape of a region of interest in order to minimize a number of suitable objectives subject to fluid flow. For performance optimization of combustion engines, in particular in the automobile industry, the optimal shape design of several components of the engine, such as air ducts, is crucial. Often additional geometric constraints impose further restrictions on the possible design. Mathematically, this problem results in a constrained multi-objective free form shape optimization problem subject to the Navier-Stokes system. In this context, for computer based rapid prototyping, constrained free form shape optimization techniques are typically superior to parameterization based techniques due to their geometric flexibility.

The goal of this project is the derivation of adjoint-based representations of shape gradient-related descent directions and the numerical realization of associated minimization schemes. For this purpose and for reasons of efficiency, reduced order models (e.g. based on shape-aware adaptive discretization) need to be developed. Furthermore, a finite volume or finite element based optimization tool which involves appropriate primal and dual turbulence models for high Reynolds numbers flows needs to be implemented and analyzed and proper preconditioning of saddle point problems has to be developed. The newly developed solver has to be tested for industry relevant use cases in a parallel computing environment.

In this context, applications in the automotive industry and quantitative biomedicine will be addressed.

8.2. The industrial partner

Math.Tec, a Vienna based mathematical consulting company, pursues the strategic goal of providing mathematics-based solutions to real-world challenges in the areas of warehouse logistics optimization, production logistics optimization, transport logistics optimization and industry optimization. Based on the development of mathematical models, Math.Tec provides innovative impulses and customer-centric approaches in order to identify the customer's challenges which are then solved by developing and employing custom-tailored software technology. Math.Tec's core competencies are in the use of modern, up-to-date mathematical techniques, optimization algorithms and software realizations.

Many tasks in the area of industry optimization have a technical and mathematical (physical, electromagnetic, fluid-mechanical or mechanical) background. The numerical simulation of fluids (CFD Computational Fluid Dynamics) is a methodical focus in this area of industry optimization. This is a technique which has increasingly complemented the traditional mainstays of fluid mechanics in recent years. The use of these techniques



to solve engineering problems has, along with the further development of simulation techniques and optimising algorithms, come increasingly to the fore. Math.Tec supports many customers, for example in the area of engine building, in realising innovative new mathematical processes in the area of numerical fluid mechanics. The most widely used solution methods in fluid mechanics (which Math.Tec runs on high performance computers) are finite difference methods (FDM), finite volume methods (FVM) and the finite element method (FEM).

8.3. Previous scientific literature

Shape optimization problems governed by the Navier-Stokes equations have already been considered in the literature. We mention the articles [124], [125] and [126], which will be relevant for our project.

In [124], Boisgérault and Zolésio propose regularity assumptions which guarantee the shape differentiability of certain cost functionals. For this purpose, they use the so-called speed method which allows to do the computations in the reference domain instead of a perturbed domain, without losing the divergence-free property.

In [125], Laurain and Sturm opt for a domain representation of the shape derivative, the so-called distributed shape derivative, as it is more general than a boundary expression and easy to compute. They propose a Lagrangian approach to compute the distributed shape derivative and they show how the level set method can be used in this context.

The authors of [126] consider the shape analysis of the unsteady Navier-Stokes equations. They discuss the Fréchet-differentiability of the flow with respect to the transformation of the problem to a reference domain, in an abstract setting as well as for the case of the unsteady Navier-Stokes equations. With these results, the Fréchet differentiability of certain objective functions is proved.

8.4. Mathematical description

Navier-Stokes equations

In order to model the flow in the considered shape, we use the stationary regime of the Navier-Stokes equations for the velocity \mathbf{u} and the kinematic pressure p

$$\begin{aligned}(\mathbf{u} \cdot \nabla)\mathbf{u} - \nu \Delta \mathbf{u} + \nabla p &= 0 \text{ in } \Omega, \\ \nabla \cdot \mathbf{u} &= 0 \text{ in } \Omega, \\ \mathbf{u} &= \mathbf{g} \text{ on } \Gamma_i, \\ \mathbf{u} &= \mathbf{0} \text{ on } \Gamma_w, \\ -\nu \partial_n \mathbf{u} + p \mathbf{n} &= \mathbf{0} \text{ on } \Gamma_o,\end{aligned}$$

where \mathbf{g} is the inflow profile, ν is the kinematic viscosity and \mathbf{n} is the outer normal vector. Figure 8.1 shows a schematic geometry and its boundary (left) and the solution \mathbf{u} of the Navier-Stokes equations (right).

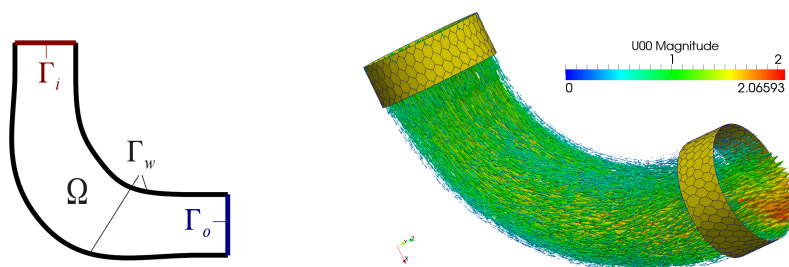


Figure 8.1: Left: sketch of a geometry and its boundary. Right: solution \mathbf{u} of the Navier-Stokes equations.

Cost functional

The cost functional depends on the geometry Ω . In order to achieve **uniform outflow** at the outlet, the cost functional

$$\mathcal{J}_1(\mathbf{u}(\Omega)) = \frac{1}{2} \int_{\Gamma_o} (\mathbf{u} \cdot \mathbf{n} - \bar{u})^2 \quad \text{with } \bar{u} = \frac{1}{|\Gamma_o|} \int_{\Gamma_i} -\mathbf{g} \cdot \mathbf{n}$$

is used. To minimize the **total pressure loss**, we use

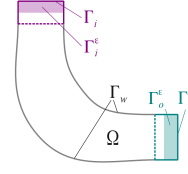
$$\mathcal{J}_2(\mathbf{u}(\Omega)) = -\frac{|\Gamma_i|}{|\Gamma_i^\epsilon|} \int_{\Gamma_i^\epsilon} \left(p + \frac{1}{2} |\mathbf{u}|^2 \right) \mathbf{u} \cdot \mathbf{n} - \frac{|\Gamma_o|}{|\Gamma_o^\epsilon|} \int_{\Gamma_o^\epsilon} \left(p + \frac{1}{2} |\mathbf{u}|^2 \right) \mathbf{u} \cdot \mathbf{n}.$$

The mixed cost functional then has the form

$$\mathcal{J}_{12}(\mathbf{u}(\Omega)) = (1 - \gamma) \mathcal{J}_1(\mathbf{u}(\Omega)) + \gamma \rho \mathcal{J}_2(\mathbf{u}(\Omega)),$$

with weighting parameter $\gamma \in [0, 1]$ and

$$\rho = \begin{cases} \frac{\|\partial \mathcal{J}_1(\mathbf{u}(\Omega^0))\|_{L^2(\Gamma_w^0)}}{\|\partial \mathcal{J}_2(\mathbf{u}(\Omega^0))\|_{L^2(\Gamma_w^0)}} & \text{if } \gamma \in (0, 1), \\ 1 & \text{if } \gamma \in \{0, 1\}. \end{cases}$$



Adjoint equation

The adjoint method allows us to obtain the shape derivative without computing the material derivative of the state. The adjoint state and pressure (\mathbf{v}, q) are calculated as the solution of the adjoint equations

$$\begin{aligned} -\nu \Delta \mathbf{v} - (\nabla \mathbf{v})^T \cdot \mathbf{u} - \nabla \mathbf{v} \cdot \mathbf{u} + \nabla q &= \gamma \nu k_\epsilon \left[(\mathbf{u} \cdot \mathbf{n}) \mathbf{u} + \left(p + \frac{1}{2} |\mathbf{u}|^2 \right) \mathbf{n} \right] \text{ in } \Omega, \\ \nabla \cdot \mathbf{v} &= -\gamma \nu k_\epsilon \mathbf{u} \cdot \mathbf{n} \quad \text{in } \Omega, \\ \mathbf{v} &= 0 \quad \text{on } \Gamma_i \cup \Gamma_w, \\ -\nu \partial_n \mathbf{v} - \mathbf{n} (\mathbf{u} \cdot \mathbf{v}) - (\mathbf{u} \cdot \mathbf{n}) \mathbf{v} + q \mathbf{n} &= -(1 - \gamma) \nu (\mathbf{u} \cdot \mathbf{n} - \bar{u}) \mathbf{n} \quad \text{on } \Gamma_o \end{aligned}$$

$$\text{with } k_\epsilon(x) = \begin{cases} -\frac{|\Gamma_i|}{|\Gamma_i^\epsilon|} & \text{if } x \in \Gamma_i^\epsilon, \\ -\frac{|\Gamma_o|}{|\Gamma_o^\epsilon|} & \text{if } x \in \Gamma_o^\epsilon, \\ 0 & \text{else.} \end{cases}$$

The Euler-semiderivative is then obtained by

$$\partial \mathcal{J}_{12}^\gamma(\Omega; V) = \int_{\Gamma_w} [\partial_n \mathbf{v} \cdot \partial_n \mathbf{u}] V \cdot \mathbf{n}$$

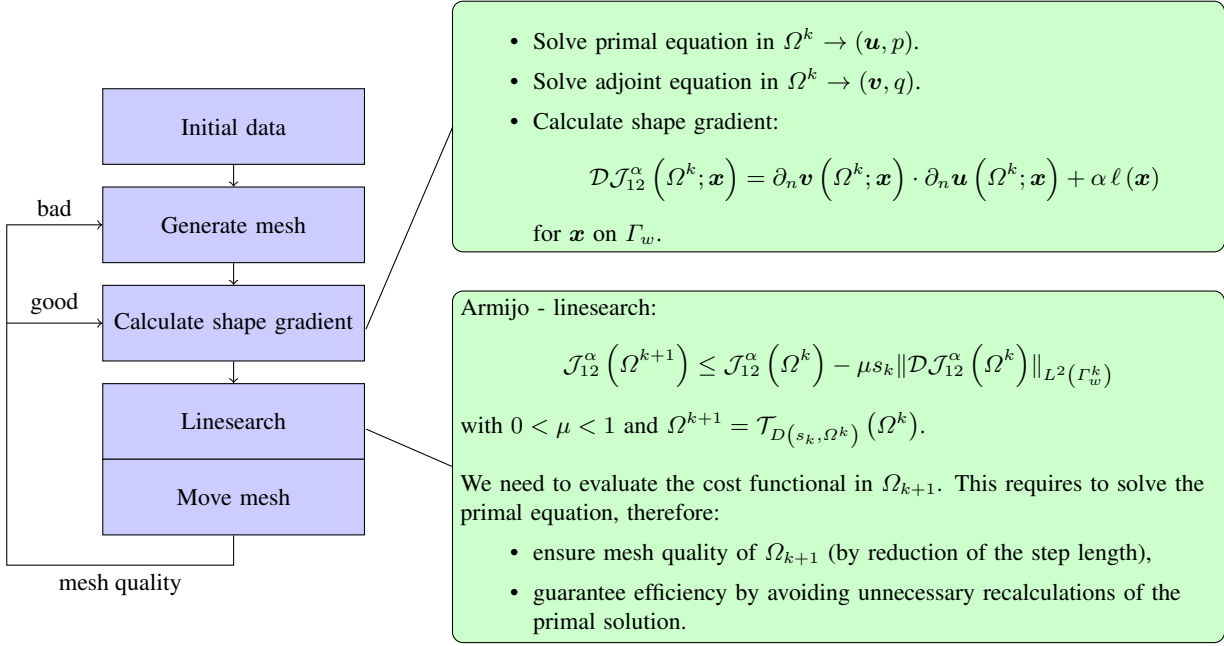
and the shape gradient by

$$D \mathcal{J}_{12}^\gamma(\Omega) = (\partial_n \mathbf{v} \cdot \partial_n \mathbf{u}) |_{\Gamma_w}.$$

Descent algorithm

The optimization is done with a gradient descent algorithm which uses an Armijo linesearch. This algorithm is illustrated in the following diagram.





Geometrical constraints

Further restrictions on the possible design are imposed by geometrical constraints which are included via a barrier or a penalty method. Figure 8.2 illustrates the constraint imposed by the design space.

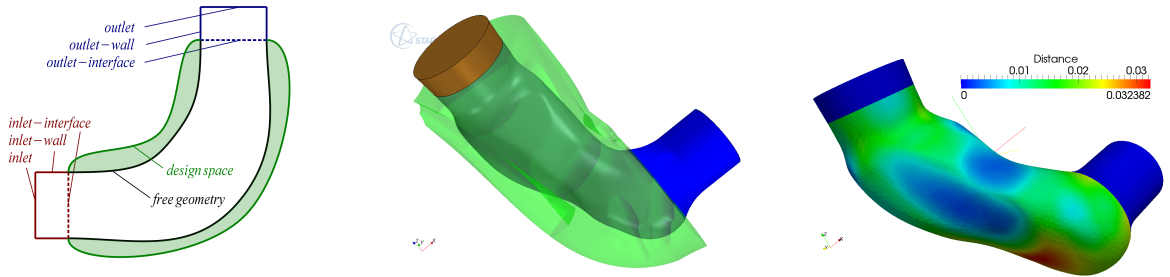


Figure 8.2: Left: sketch of geometry and design space. Middle: geometry with transparent design space. Right: geometry with distance values to the design space.

The minimization problem with geometrical constraint

$$\text{minimize } \mathcal{J}_{12}(\mathbf{u}(\Omega)) \quad \text{s.t. } \Omega \subset K$$

can be reformulated as

$$\text{minimize } \mathcal{J}_{12}(\mathbf{u}(\Omega)) + \alpha \mathcal{L}(\Omega)$$

with $\alpha > 0$ and $\mathcal{L}(\Omega) = \int_{\Omega} \ell(\Omega)$. In the case of the barrier method, we are using

$$\ell(\Omega) = |\ln d(x, K^c)|,$$

and in the case of the penalty method

$$\ell(\Omega) = (d(x, K))^\beta,$$

with $\beta \geq 1$, $K^c = \mathbb{R}^n \setminus K$ and the distance function $d(x, K) = \min_{y \in K} |x - y|$.



The sensitivity is calculated by

$$\partial \mathcal{L}(\Omega, V) = \int_{\Omega} \ell'(\Omega, V) dx + \int_{\Gamma} \ell(\Omega) \langle V(0), \mathbf{n} \rangle = \int_{\Gamma} \ell(\Omega) \langle V(0), \mathbf{n} \rangle.$$

To avoid kinks between the fixed geometry and the geometry which needs to be optimized (see Figure 8.3), we add a penalty functional (green) to the cost functional

$$\mathcal{J}_{12}^{\alpha, \varphi}(\mathbf{u}(\Omega)) = \mathcal{J}_{12}(\mathbf{u}(\Omega)) + \alpha \mathcal{L}(\Omega) + \varphi \mathcal{L}_F(\Omega)$$

with $\mathcal{L}_F(\Omega) = \int_{\Omega} (d(x, K_F))^2$, weight φ , distance function d and valid domain K_F .

The sensitivity is then calculated by

$$\partial \mathcal{L}_F(\Omega, V) = \int_{\Gamma} \ell_F(\Omega) \langle V(0), \mathbf{n} \rangle \quad \text{with } \ell_F = (d(x, K_F))^2.$$

The displacement of the mesh is based on the negative shape gradient, which is shown in the left of Figure 8.4. It consists of the part which is related to the achievement of a uniform outflow and the minimization of the total pressure loss (Figure 8.4, middle) and the part which belongs to the penalty function of the geometrical constraints (Figure 8.4, right).

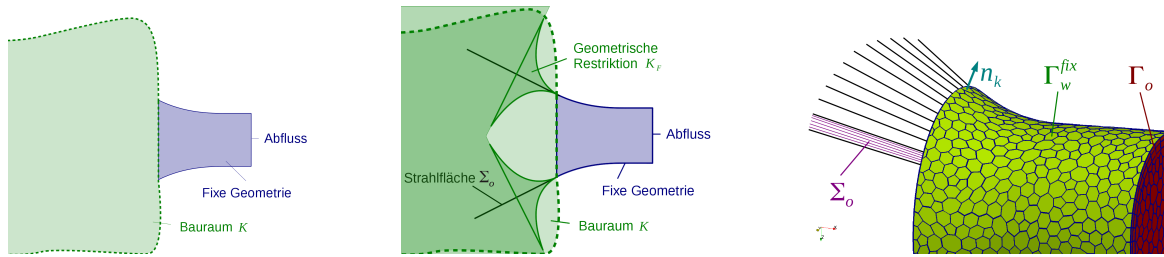


Figure 8.3: Left: fixed geometry (blue) and design space (green). Middle: additional valid domain. Right: continuation of the fixed geometry.

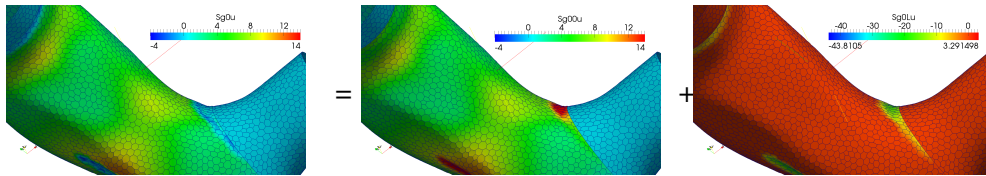


Figure 8.4: Left: negative shape gradient after 20 iterations. Middle: part of the shape gradient related to uniform outflow and minimization of total pressure loss. Right: part of the shape gradient related to geometrical constraints.

Turbulence modeling for high Reynolds numbers

The turbulent flow in applications with high Reynolds numbers ($Re = 200,000$) is modeled with a Reynolds-averaged Navier–Stokes (RANS) approach. We use a $k-\epsilon$ turbulence model which describes the evolution of the turbulent kinetic energy k and the rate of dissipation of the turbulent energy ϵ .

The kinematic viscosity ν in the Navier–Stokes equations is replaced by the effective viscosity, which is the sum of kinematic and turbulent viscosity:

$$\nu_{eff} = \nu + \nu_t.$$

Instead of the convection equation

$$\mathbf{u}_t + \nabla \cdot (\mathbf{u}\mathbf{u}^T) - \nu \Delta \mathbf{u} + \nabla p = \mathbf{z},$$

the equation

$$\mathbf{u}_t + \nabla \cdot (\mathbf{u}\mathbf{u}^T) - \nabla \cdot ((\nu + \nu_t) \nabla \mathbf{u}) + \nabla \left(p + \frac{2}{3}k \right) = \mathbf{z}$$

is solved with $\nu_t = C_\nu \frac{k^2}{\varepsilon}$. The kinetic energy k and the dissipation ε are solutions of

$$\begin{aligned} \partial_t k &= -(\mathbf{u} \cdot \nabla) k + \nabla \cdot ((\nu + \nu_t) \nabla k) + \nu_t |\nabla \mathbf{u} + \nabla \mathbf{u}^T|^2 - \varepsilon \\ \partial_t \varepsilon &= -(\mathbf{u} \cdot \nabla) \varepsilon + \nabla \cdot \left(\left(\nu + \frac{\nu_t}{\sigma_\varepsilon} \right) \nabla \varepsilon \right) + C_1 \frac{\varepsilon}{k} \nu_t |\nabla \mathbf{u} + \nabla \mathbf{u}^T|^2 - C_2 \frac{\varepsilon^2}{k} \end{aligned}$$

with standard model constants $C_\nu = 0.09$, $C_1 = 1.44$, $C_2 = 1.92$, $\sigma_\varepsilon = 1.3$.

Figure 8.5 illustrates the change of geometry during the shape optimization for a turbulent flow with Reynolds number $\text{Re} = 200,000$.

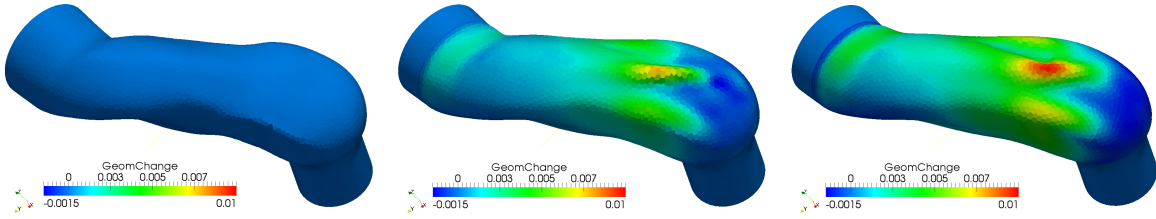


Figure 8.5: Change of geometry in the beginning (left), after 20 (middle) and after 70 iterations (right).

Laplace-Beltrami smoothing

A Laplace-Beltrami smoothing is applied by using the following equation on the surface Γ :

$$\begin{aligned} -\varepsilon \Delta_\Gamma w + w &= -g_{\mathcal{J}_{12}} & \text{on } \Gamma, \\ w &= 0 & \text{on } \partial\Gamma. \end{aligned}$$

The Laplace-Beltrami smoothing realizes a preconditioning of the gradient method. It permits a higher regularity of each grid movement while keeping the property of a descent direction. Figure 8.6 shows results without and with the Laplace-Beltrami smoothing for two different geometries.

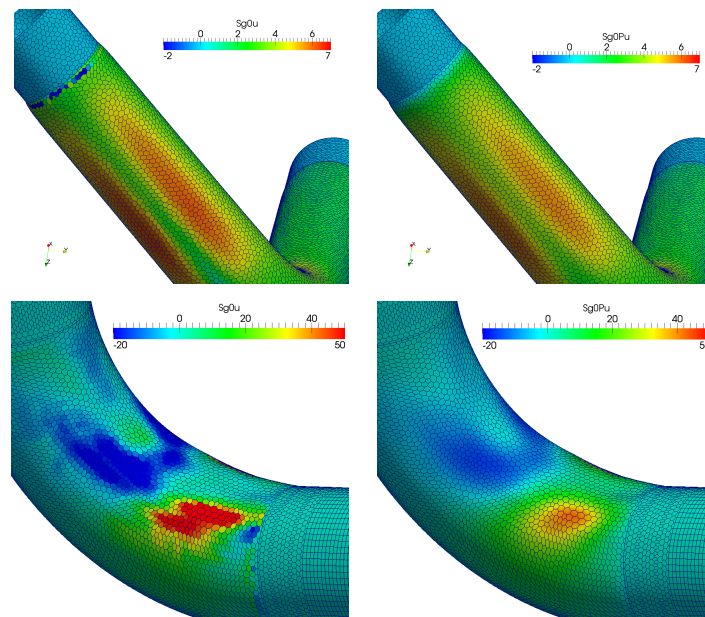


Figure 8.6: Left: Shape gradient without LB-smoothing. Right: Shape gradient with LB-smoothing.

Shape optimization tested on various geometries

Figure 8.7 shows the change of geometry after the shape optimization for four different examples.

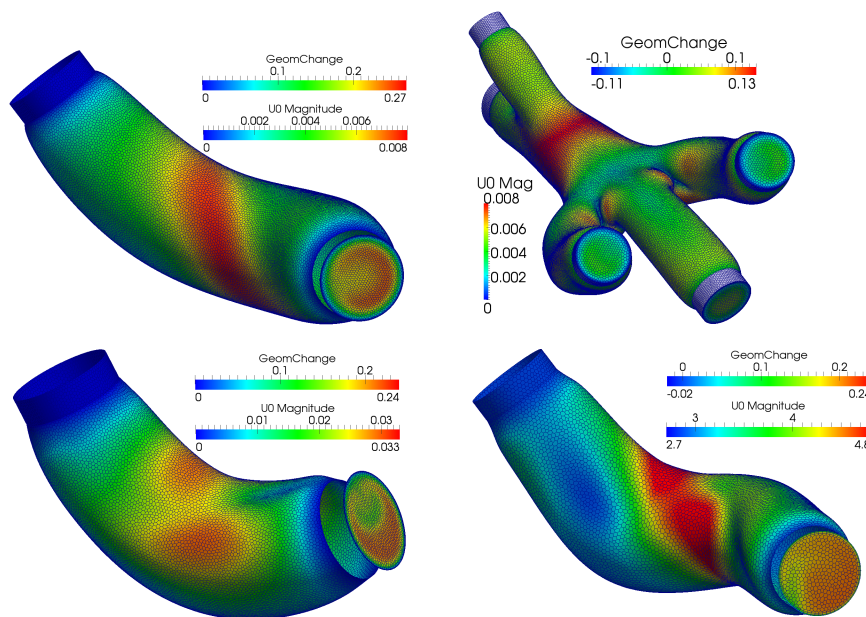


Figure 8.7: Final geometries: Upper: $Re = 200$, $Re = 400$; Lower: $Re = 1000$, $Re = 200\,000$

8.5. Description of the publicly available data

The developed shape optimization tool should be tested on the benchmark geometry which will be introduced in the following. The proposed geometry has been developed together with engineers from the automotive industry and presents an example which is relevant for real-life applications in this field.

The geometry describes an air duct in a combustion engine and is shown from different perspectives in Figure 8.8. It consists of one inlet Γ_i and one outlet Γ_o . The parts next to the inlet and to the outlet, which are called



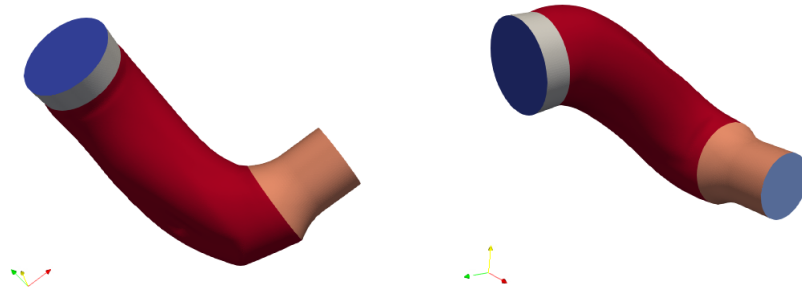


Figure 8.8: The proposed benchmark geometry (from two different perspectives) consists of an inlet (dark blue), a fixed inlet-wall (gray), an outlet (light blue), a fixed outlet-wall (orange) and a wall whose shape shall be optimized (red).

inlet-wall and outlet-wall, are fixed. These parts are connected with the free geometry that shall be optimized. The caption of Figure 8.8 identifies the constituent parts of the geometry.

The whole geometry is inscribed in a design space which should be respected as an outer limit of the shape variation. The design space is illustrated in Figure 8.9. Figure 8.10 shows the geometry with transparent design space.

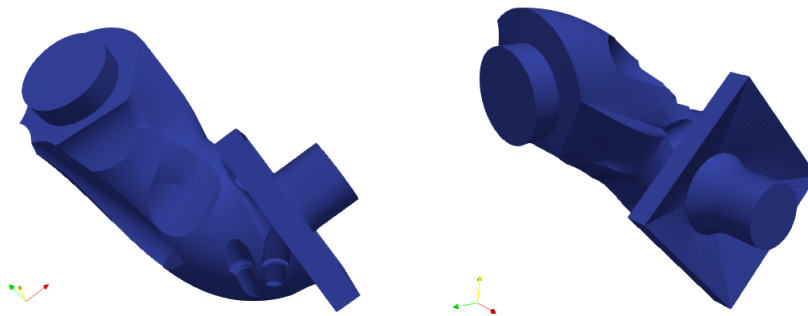


Figure 8.9: The design space which constrains the possible shape of the air duct (from two different perspectives).

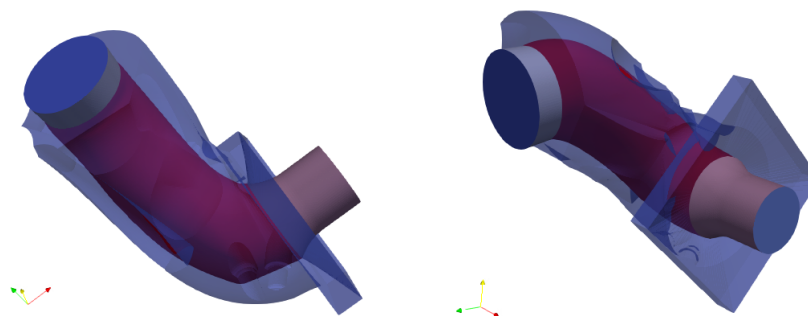


Figure 8.10: The geometry of the air duct inscribed in the design space (from two different perspectives).

References

- [1] Microgate, “Description of industrial partner,” Online Description. [Online]. Available: <http://www.microgate.it>
- [2] F. Roddier, “Adaptive optics in astronomy,” Cambridge, U.K. ; New York :Cambridge University Press, 1999.
- [3] A. Tokovinin, “Adaptive optics tutorial at ctio,” Cambridge University Press, 1999.
- [4] J. Primot, “Theoretical description of shack–hartmann wave-front sensor,” *Optics Communications* 222(1):81–92, 2003.
- [5] C. Verinaud, “On the nature of the measurements provided by a pyramid wave-front sensor,” *Optics Communications* 233:27–38, 2004.
- [6] E. Vernet, M. Cayrel, N. Hubin, R. Biasi, G. Angerer, M. Andrighettoni, D. Pescoller, D. Gallieni, M. Tintori, M. Mantegazza, and et. al., “The adaptive mirror for the e-elt,” In Proceedings of the Third AO4ELT Conference, 2013.
- [7] E. S. Observatory, “Eso,” Online Description. [Online]. Available: <http://www.eso.org>
- [8] A. N. Kolmogorov, “The local structure of turbulence in incompressible viscous fluid for very large reynolds numbers,” In *Dokl. Akad. Nauk SSSR* volume 30, pages 299–303, 1941.
- [9] T. von Karman, “Mechanische Ähnlichkeit und turbulenz,” rd International Congress of Applied Mechanics, 1930.
- [10] N. F. Law and R. G. Lane, “Wavefront estimation at low light levels,” *Optics Communications* 126:19–24, 1996.
- [11] M. Rosensteiner, “Wavefront reconstruction for extremely large telescopes via cure with domain decomposition,” *J. Opt. Soc. Am. A* 29(11):2328–2336, 2012.
- [12] I. Shatokhina, A. Obereder, M. Rosensteiner, and R. Ramlau, “Preprocessed cumulative reconstructor with domain decomposition: a fast wavefront reconstruction method for pyramid wavefront sensor,” *Applied Optics* 52(12):2640–2652, 2013.
- [13] T. Fusco, J.-M. Conan, G. Rousset, L. Mugnier, and V. Michau, “Optimal wavefront reconstruction strategies for multi conjugate adaptive optics,” *J. Opt. Soc. Am. A* 18(10):2527–2538, 2001.
- [14] T. Helin and M. Yudytskiy, “Wavelet methods in multi-conjugate adaptive optics,” *Inverse Problems* 29(8):085003, 2013.
- [15] ESO, “Online description of octopus,” Online description. [Online]. Available: <http://www.eso.org/sci/facilities/develop/ao/tecn/octopus.html>
- [16] V. Svetovoy and I. Winter, “Model of the μ -flown microphone,” *Sensors and Actuators A: Physical*, vol. 86, no. 3, pp. 171–181, Nov 2000. [Online]. Available: <https://www.sciencedirect.com/science/article/pii/S0924424700004544>
- [17] J. W. van Honschoten, G. J. M. Krijnen, V. B. Svetovoy, H.-E. de Bree, and M. C. Elwenspoek, “Analytic model of a two-wire thermal sensor for flow and sound measurements,” *Journal of Micromechanics and Microengineering*, vol. 14, no. 11, p. 1468, 2004. [Online]. Available: <http://stacks.iop.org/0960-1317/14/i=11/a=006>
- [18] R. Raangs, “Exploring the use of the microflown,” Ph.D. dissertation, University of Twente, 12 2005.
- [19] H.-E. de Bree, *The Microflown E-Book*. Microflown Technologies, Arnhem, 2007. [Online]. Available: <http://www.microflown.com/library/books/the-microflown-e-book.htm>
- [20] A. Pierce, *Acoustics: An Introduction to Its Physical Principles and Applications*. Acoustical Society of America, 1989.
- [21] F. Ihlenburg, *Finite element analysis of acoustic scattering*. Springer-Verlag New York, 1998, vol. 132. [Online]. Available: <http://dx.doi.org/10.1007/b98828>



- [22] “SALOME: An Open-source Integration Platform for Simulation.” [Online]. Available: <http://salome-platform.org/>
- [23] M. S. Alnæs, J. Blechta, J. Hake, A. Johansson, B. Kehlet, A. Logg, C. Richardson, J. Ring, M. E. Rognes, and G. N. Wells, “The fenics project version 1.5,” *Archive of Numerical Software*, vol. 3, no. 100, 2015.
- [24] H. P. Langtangen and A. Logg, *Solving PDEs in Python*. Springer International Publishing, 2016. [Online]. Available: <http://link.springer.com/10.1007/978-3-319-52462-7>
- [25] C. R. Llamas, “Optimization of an acoustic intensity P-U probe design using numerical methods,” Master’s thesis, University of A Coruña, 2018.
- [26] X.-J. Wang, “On the design of a reflector antenna ii,” *Calculus of Variations and Partial Differential Equations*, vol. 20, no. 3, pp. 329–341, Jul 2004. [Online]. Available: <https://doi.org/10.1007/s00526-003-0239-4>
- [27] G. Peyré and M. Cuturi, “Computational Optimal Transport,” *ArXiv e-prints*, Mar. 2018.
- [28] C. Villani, *Optimal Transport: Old and New*, ser. Grundlehren der mathematischen Wissenschaften. Springer Berlin Heidelberg, 2008. [Online]. Available: <https://books.google.fr/books?id=NZXiNAEACAAJ>
- [29] F. Santambrogio, *Optimal Transport for Applied Mathematicians: Calculus of Variations, PDEs, and Modeling*, ser. Progress in Nonlinear Differential Equations and Their Applications. Springer International Publishing, 2015. [Online]. Available: <https://books.google.fr/books?id=UOHHCgAAQBAJ>
- [30] P. Machado Manhães De Castro, Q. Mérigot, and B. Thibert, “Far-field reflector problem and intersection of paraboloids,” *Numerische Mathematik*, vol. 134, no. 2, pp. 389–411, Oct. 2016. [Online]. Available: <https://hal.archives-ouvertes.fr/hal-00952720>
- [31] K. Brix, Y. Hafizogullari, and A. Platen, “Solving the Monge-Ampère Equations for the Inverse Reflector Problem,” *ArXiv e-prints*, Apr. 2014.
- [32] R. J. Berman, “The Sinkhorn algorithm, parabolic optimal transport and geometric Monge-Ampère equations,” *ArXiv e-prints*, Dec. 2017.
- [33] R. S. Womersley, “Efficient Spherical Designs with Good Geometric Properties,” *ArXiv e-prints*, Sep. 2017.
- [34] J. Weizenecker, B. Gleich, J. Rahmer, H. Dahnke, and J. Borgert, “Three-dimensional real-time in vivo magnetic particle imaging,” *Physics in Medicine and Biology*, vol. 54, no. 5, p. L1, 2009.
- [35] A. Khandhar, P. Keselman, S. Kemp, R. Ferguson, P. Goodwill, S. Conolly, and K. Krishnan, “Evaluation of peg-coated iron oxide nanoparticles as blood pool tracers for preclinical magnetic particle imaging,” *Nanoscale*, vol. 9, no. 3, pp. 1299–1306, 2017.
- [36] J. Franke, R. Lacroix, H. Lehr, M. Heidenreich, U. Heinen, and V. Schulz, “Mpi flow analysis toolbox exploiting pulsed tracer information – an aneurysm phantom proof,” *International Journal on Magnetic Particle Imaging*, vol. 3, no. 1, 2017. [Online]. Available: <https://journal.iwmpi.org/index.php/iwmpi/article/view/36>
- [37] J. Haegele, J. Rahmer, B. Gleich, J. Borgert, H. Wojtczyk, N. Panagiotopoulos, T. Buzug, J. Barkhausen, and F. Vogt, “Magnetic particle imaging: visualization of instruments for cardiovascular intervention,” *Radiology*, vol. 265, no. 3, pp. 933–938, 2012.
- [38] J. Salamon, M. Hofmann, C. Jung, M. G. Kaul, F. Werner, K. Them, R. Reimer, P. Nielsen, A. vom Scheidt, G. Adam, T. Knopp, and H. Ittrich, “Magnetic particle/magnetic resonance imaging: In-vitro MPI-guided real time catheter tracking and 4D angioplasty using a road map and blood pool tracer approach,” *PLoS ONE*, vol. 11, no. 6, pp. e0156899–14, 2016.
- [39] E. Y. Yu, M. Bishop, B. Zheng, R. M. Ferguson, A. P. Khandhar, S. J. Kemp, K. M. Krishnan,



- P. W. Goodwill, and S. M. Conolly, "Magnetic particle imaging: A novel in vivo imaging platform for cancer detection," *Nano Letters*, vol. 17, no. 3, pp. 1648–1654, 2017. [Online]. Available: <http://dx.doi.org/10.1021/acs.nanolett.6b04865>
- [40] K. Murase, M. Aoki, N. Banura, K. Nishimoto, A. Mimura, T. Kuboyabu, and I. Yabata, "Usefulness of magnetic particle imaging for predicting the therapeutic effect of magnetic hyperthermia," *Open Journal of Medical Imaging*, vol. 5, no. 02, p. 85, 2015.
- [41] K. H. Jin, M. T. McCann, E. Froustey, and M. Unser, "Deep convolutional neural network for inverse problems in imaging," *IEEE Transactions on Image Processing*, vol. 26, no. 9, pp. 4509–4522, 2017.
- [42] S. Lunz, O. Öktem, and C.-B. Schönlieb, "Adversarial regularizers in inverse problems," *arXiv preprint arXiv:1805.11572*, 2018.
- [43] J. Behrmann, C. Etmann, T. Boskamp, R. Casadonte, J. Kriegsmann, and P. Maaß, "Deep learning for tumor classification in imaging mass spectrometry," *Bioinformatics*, vol. 34, no. 7, pp. 1215–1223, 2017.
- [44] S. Wang, Z. Su, L. Ying, X. Peng, S. Zhu, F. Liang, D. Feng, and D. Liang, "Accelerating magnetic resonance imaging via deep learning," in *Biomedical Imaging (ISBI), 2016 IEEE 13th International Symposium on*. IEEE, 2016, pp. 514–517.
- [45] J. Schlemper, J. Caballero, J. V. Hajnal, A. N. Price, and D. Rueckert, "A deep cascade of convolutional neural networks for dynamic mr image reconstruction," *IEEE transactions on Medical Imaging*, vol. 37, no. 2, pp. 491–503, 2018.
- [46] E. Kang, J. Min, and J. C. Ye, "A deep convolutional neural network using directional wavelets for low-dose x-ray ct reconstruction," *Medical physics*, vol. 44, no. 10, 2017.
- [47] K. Gong, J. Guan, K. Kim, X. Zhang, G. E. Fakhri, J. Qi, and Q. Li, "Iterative pet image reconstruction using convolutional neural network representation," *arXiv preprint arXiv:1710.03344*, 2017.
- [48] B. Gleich and J. Weizenecker, "Tomographic imaging using the nonlinear response of magnetic particles," *Nature*, vol. 435, no. 7046, pp. 1214–1217, June 2005.
- [49] J. Weizenecker, B. Gleich, and J. Borgert, "Magnetic particle imaging using a field free line," *Journal of Physics D: Applied Physics*, vol. 41, no. 10, p. 105009, 2008. [Online]. Available: <http://stacks.iop.org/0022-3727/41/i=10/a=105009>
- [50] T. Kluth, "Mathematical models for magnetic particle imaging," *Inverse Problems*, 2018, accepted manuscript online available at <http://iopscience.iop.org/article/10.1088/1361-6420/aac535>. [Online]. Available: <http://iopscience.iop.org/article/10.1088/1361-6420/aac535>
- [51] T. Knopp and T. M. Buzug, *Magnetic Particle Imaging: An Introduction to Imaging Principles and Scanner Instrumentation*. Berlin/Heidelberg: Springer, 2012.
- [52] S. Lunz, O. Öktem, and C.-B. Schönlieb, "Adversarial regularizers in inverse problems." [Online]. Available: <https://arxiv.org/abs/1805.11572>
- [53] H. Li, J. Schwab, S. Antholzer, and M. Haltmeier, "Nett: Solving inverse problems with deep neural networks," *arXiv preprint arXiv:1803.00092*, 2018.
- [54] S. V. Venkatakrishnan, C. A. Bouman, and B. Wohlberg, "Plug-and-play priors for model based reconstruction," in *Global Conference on Signal and Information Processing (GlobalSIP), 2013 IEEE*. IEEE, 2013, pp. 945–948.
- [55] J. R. Chang, C. Li, B. Póczos, B. V. K. V. Kumar, and A. C. Sankaranarayanan, "One network to solve them all - solving linear inverse problems using deep projection models," *CoRR*, vol. abs/1703.09912, 2017. [Online]. Available: <http://arxiv.org/abs/1703.09912>
- [56] T. Meinhardt, M. Möller, C. Hazirbas, and D. Cremers, "Learning proximal operators: Using denoising networks for regularizing inverse imaging problems," *CoRR*, vol. abs/1704.03488, 2017. [Online]. Available: <http://arxiv.org/abs/1704.03488>
- [57] K. Gregor and Y. LeCun, "Learning fast approximations of sparse coding," in *Proceedings of the 27th*

- International Conference on International Conference on Machine Learning*. Omnipress, 2010, pp. 399–406.
- [58] M. Andrychowicz, M. Denil, S. Gomez, M. W. Hoffman, D. Pfau, T. Schaul, B. Shillingford, and N. De Freitas, “Learning to learn by gradient descent by gradient descent,” in *Advances in Neural Information Processing Systems*, 2016, pp. 3981–3989.
- [59] P. Putzky and M. Welling, “Recurrent inference machines for solving inverse problems,” *arXiv preprint arXiv:1706.04008*, 2017.
- [60] J. Adler and O. Öktem, “Solving ill-posed inverse problems using iterative deep neural networks,” 2017. [Online]. Available: <https://arxiv.org/abs/1704.04058>
- [61] B. Kelly, T. P. Matthews, and M. A. Anastasio, “Deep learning-guided image reconstruction from incomplete data,” *arXiv preprint arXiv:1709.00584*, 2017.
- [62] J. Adler, A. Ringh, O. Öktem, and J. Karlsson, “Learning to solve inverse problems using wasserstein loss,” *CoRR*, vol. abs/1710.10898, 2017. [Online]. Available: <http://arxiv.org/abs/1710.10898>
- [63] J. Adler and O. Öktem, “Learned primal-dual reconstruction,” 2017. [Online]. Available: <https://arxiv.org/abs/1707.06474>
- [64] A. Hauptmann, F. Lucka, M. M. Betcke, N. Huynh, B. T. Cox, P. C. Beard, S. Ourselin, and S. R. Arridge, “Model based learning for accelerated, limited-view 3d photoacoustic tomography,” *CoRR*, vol. abs/1708.09832, 2017. [Online]. Available: <http://arxiv.org/abs/1708.09832>
- [65] K. Hammernik, T. Klatzer, E. Kobler, M. P. Recht, D. K. Sodickson, T. Pock, and F. Knoll, “Learning a variational network for reconstruction of accelerated mri data,” *Magnetic resonance in medicine*, vol. 79, no. 6, pp. 3055–3071, 2018.
- [66] D. Van Veen, A. Jalal, E. Price, S. Vishwanath, and A. G. Dimakis, “Compressed sensing with deep image prior and learned regularization,” *arXiv preprint arXiv:1806.06438*, 2018.
- [67] D. Ulyanov, A. Vedaldi, and V. Lempitsky, “Deep image prior,” *arXiv preprint arXiv:1711.10925*, 2017.
- [68] C. Dong, C. C. Loy, K. He, and X. Tang, “Learning a deep convolutional network for image super-resolution,” in *Computer Vision – ECCV 2014*, D. Fleet, T. Pajdla, B. Schiele, and T. Tuytelaars, Eds. Cham: Springer International Publishing, 2014, pp. 184–199.
- [69] L. Xu, J. S. Ren, C. Liu, and J. Jia, “Deep convolutional neural network for image deconvolution,” in *Advances in Neural Information Processing Systems*, 2014, pp. 1790–1798.
- [70] C. Dong, C. C. Loy, K. He, and X. Tang, “Image super-resolution using deep convolutional networks,” *IEEE transactions on pattern analysis and machine intelligence*, vol. 38, no. 2, pp. 295–307, 2016.
- [71] H. C. Burger, C. J. Schuler, and S. Harmeling, “Image denoising: Can plain neural networks compete with bm3d?” in *Computer Vision and Pattern Recognition (CVPR), 2012 IEEE Conference on*. IEEE, 2012, pp. 2392–2399.
- [72] J. Xie, L. Xu, and E. Chen, “Image denoising and inpainting with deep neural networks,” in *Advances in neural information processing systems*, 2012, pp. 341–349.
- [73] X. Tao, H. Gao, X. Shen, J. Wang, and J. Jia, “Scale-recurrent network for deep image deblurring,” in *Proceedings of the IEEE Conference on Computer Vision and Pattern Recognition*, 2018, pp. 8174–8182.
- [74] C. Chen, Q. Chen, J. Xu, and V. Koltun, “Learning to see in the dark,” *arXiv preprint arXiv:1805.01934*, 2018.
- [75] D. V. Veen, A. Jalal, E. Price, S. Vishwanath, and A. G. Dimakis, “Compressed sensing with deep image prior and learned regularization,” *CoRR*, vol. abs/1806.06438, 2018. [Online]. Available: <https://arxiv.org/abs/1806.06438>
- [76] World Steel Association, “World steel in figures 2018,” *World Steel Association: Brussels, Belgium*, 2018.

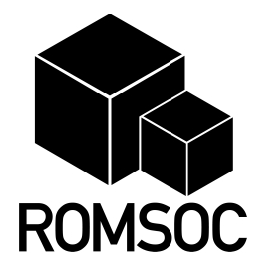


- [77] B. G. Thomas, “Review on modeling and simulation of continuous casting,” *Steel Research Int.*, vol. 89, no. 1, p. 1700312, 2018.
- [78] L. Klimeš and J. Štětina, “A rapid gpu-based heat transfer and solidification model for dynamic computer simulations of continuous steel casting,” *Journal of Materials Processing Technology*, vol. 226, pp. 1–14, 2015.
- [79] “Danieli & C. Officine Meccaniche S.p.A.” https://www.danieli.com/en/_1.htm, accessed: 2018-09-11.
- [80] B. G. Thomas and F. M. Najjar, “Finite element modelling of turbulent fluid flow and heat transfer in continuous casting,” *Applied Mathematical Modelling*, vol. 15, no. 5, pp. 226 – 243, 1991.
- [81] B. Thomas, G. Li, A. Moitra, and D. Habing, “Analysis of thermal and mechanical behavior of copper molds during continuous casting of steel slabs,” *Iron and Steelmaker(USA)*, vol. 25, no. 10, pp. 125–143, 1998.
- [82] A. Gupta, R. Singh, A. Paul, and S. Kumar, “Effect of mould geometry, coating, and plate thickness on the thermal profile of continuous casting moulds,” *Journal of the Southern African Institute of Mining and Metallurgy*, vol. 118, no. 5, pp. 505–513, 2018.
- [83] R. B. Mahapatra, J. K. Brimacombe, and I. V. Samarasekera, “Mold behavior and its influence on quality in the continuous casting of steel slabs: Part ii. mold heat transfer, mold flux behavior, formation of oscillation marks, longitudinal off-corner depressions, and subsurface cracks,” *Metallurgical and Materials Transactions B*, vol. 22, no. 6, pp. 875–888, Dec 1991.
- [84] J. Savage and W. Pritchard, “The problem of rupture of the billet in the continuous casting of steel,” *Journal of the Iron and Steel Institute*, vol. 178, no. 3, pp. 269–277, 1954.
- [85] D. Fengming, W. Xudong, L. Yu, W. Shanjiao, Z. Ze, and Y. Man, “Investigation on thermo-mechanical behavior of mold corner for continuous casting slab,” *ISIJ International*, vol. 55, no. 10, pp. 2150–2157, 2015.
- [86] J. Yang, Z. Cai, and M. Zhu, “Transient thermo-fluid and solidification behaviors in continuous casting mold: Evolution phenomena,” *ISIJ International*, vol. 58, no. 2, pp. 299–308, 2018.
- [87] C. Sleicher and M. Rouse, “A convenient correlation for heat transfer to constant and variable property fluids in turbulent pipe flow,” *International Journal of Heat and Mass Transfer*, vol. 18, no. 5, pp. 677 – 683, 1975.
- [88] I. Samarasekera and J. K. Brimacombe, “The thermal field in continuous-casting moulds,” *Canadian Metallurgical Quarterly*, vol. 18, no. 3, pp. 251–266, 1979.
- [89] Y. Meng and B. G. Thomas, “Heat-transfer and solidification model of continuous slab casting: Con1d,” *Metallurgical and Materials Transactions B*, vol. 34, no. 5, pp. 685–705, Oct 2003.
- [90] X. Xie, D. Chen, H. Long, M. Long, and K. Lv, “Mathematical modeling of heat transfer in mold copper coupled with cooling water during the slab continuous casting process,” *Metallurgical and Materials Transactions B*, vol. 45, no. 6, pp. 2442–2452, Dec 2014.
- [91] X. Wang and M. Yao, “Neural networks for solving the inverse heat transfer problem of continuous casting mould,” in *2011 Seventh International Conference on Natural Computation*, vol. 2, July 2011, pp. 791–794.
- [92] H. Zhang, W. Wang, F. Ma, and L. Zhou, “Mold simulator study of the initial solidification of molten steel in continuous casting mold. part i: Experiment process and measurement,” *Metallurgical and Materials Transactions B*, vol. 46, no. 5, pp. 2361–2373, Oct 2015.
- [93] F. ming DU, X. dong WANG, Y. LIU, T. yi LI, and M. YAO, “Analysis of non-uniform mechanical behavior for a continuous casting mold based on heat flux from inverse problem,” *Journal of Iron and Steel Research, International*, vol. 23, no. 2, pp. 83 – 91, 2016.
- [94] H. Zhang, W. Wang, and L. Zhou, “Calculation of heat flux across the hot surface of continuous casting



- mold through two-dimensional inverse heat conduction problem,” *Metallurgical and Materials Transactions B*, vol. 46, no. 5, pp. 2137–2152, Oct 2015.
- [95] Udayraj, S. Chakraborty, S. Ganguly, E. Chacko, S. Ajmani, and P. Talukdar, “Estimation of surface heat flux in continuous casting mould with limited measurement of temperature,” *International Journal of Thermal Sciences*, vol. 118, pp. 435 – 447, 2017.
- [96] Y. A. Cengel, *Heat transfer: a practical approach*. Boston, Mass: WBC McGraw-Hill, 2007.
- [97] A. Lehtinen and R. Karvinen, “Analytical solution for a class of flat plate conjugate convective heat transfer problems,” *Frontiers in Heat and Mass Transfer*, vol. 2, pp. 1–6, 2011.
- [98] F. Du, X. Wang, M. Yao, and X. Zhang, “Analysis of the non-uniform thermal behavior in slab continuous casting mold based on the inverse finite-element model,” *Journal of Materials Processing Technology*, vol. 214, no. 11, pp. 2676 – 2683, 2014.
- [99] A. C. Alba and D. H. Delgado, “The future is here: ventricular assist devices for the failing heart,” *Expert Review of Cardiovascular Therapy*, vol. 7, no. 9, pp. 1067–1077, 2009.
- [100] D. Mozaffarian, E. J. Benjamin, A. S. Go, D. K. Arnett, M. J. Blaha, M. Cushman, S. R. Das, S. de Ferranti, J. P. Després, H. J. Fullerton *et al.*, “Heart disease and stroke statistics-2016 update a report from the american heart association,” *Circulation*, vol. 133, no. 4, pp. e38–e48, 2016.
- [101] J. D. Christie, L. B. Edwards, A. Y. Kucheryavaya, C. Benden, F. Dobbels, R. Kirk, A. O. Rahmel, J. Stehlik, and M. I. Hertz, “The registry of the international society for heart and lung transplantation: twenty-eighth adult lung and heart-lung transplant report—2011,” *The Journal of Heart and Lung Transplantation*, vol. 30, no. 10, pp. 1104–1122, 2011.
- [102] J. G. Rogers, F. D. Pagani, A. J. Tatoes, G. Bhat, M. S. Slaughter, E. J. Birks, S. W. Boyce, S. S. Najjar, V. Jeevanandam, A. S. Anderson *et al.*, “Intrapericardial left ventricular assist device for advanced heart failure,” *New England Journal of Medicine*, vol. 376, no. 5, pp. 451–460, 2017.
- [103] M. Perschall, J. B. Drevet, T. Schenkel, and H. Oertel, “The progressive wave pump: numerical multiphysics investigation of a novel pump concept with potential to ventricular assist device application,” *Artificial organs*, vol. 36, no. 9, 2012.
- [104] A. Untaroiu, H. G. Wood, P. E. Allaire, A. L. Throckmorton, S. Day, S. M. Patel, P. Ellman, C. Tribble, and D. B. Olsen, “Computational design and experimental testing of a novel axial flow lvad,” *ASAIO journal*, vol. 51, no. 6, pp. 702–710, 2005.
- [105] S. Pirker, H. Schima, and M. Stoiber, “Numerical simulation of hemolysis: A comparison of lagrangian and eulerian modelling,” *WIT Transactions on Biomedicine and Health*, vol. 8, pp. 361–370, 2005.
- [106] D. Carswell, D. McBride, T. Croft, A. Slone, M. Cross, and G. Foster, “A cfd model for the prediction of haemolysis in micro axial left ventricular assist devices,” *Applied Mathematical Modelling*, vol. 37, no. 6, pp. 4199 – 4207, 2013.
- [107] E. Burman and M. A. Fernández, “An unfitted nitsche method for incompressible fluid–structure interaction using overlapping meshes,” *Computer Methods in Applied Mechanics and Engineering*, vol. 279, pp. 497–514, 2014.
- [108] S. Zonca, C. Vergara, and L. Formaggia, “An unfitted formulation for the interaction of an incompressible fluid with a thick structure via an xfem/dg approach,” *SIAM Journal on Scientific Computing*, vol. 40, no. 1, pp. B59–B84, 2018.
- [109] L. Bertagna, S. DeParis, L. Formaggia, D. Forti, and A. Veneziani, “The lifev library: engineering mathematics beyond the proof of concept,” *arXiv preprint arXiv:1710.06596*, 2017.
- [110] D. H. B. Andrade, R. P. Tavares, A. C. B. Quintas, V. E. de Souza Moreira, A. O. Viana, and V. M. Gasparini, “Evaluation of the permeability of the dripping zone and of flooding phenomena in a blast furnace,” *Journal of Materials Research and Technology*, 2017. [Online]. Available: <http://www.sciencedirect.com/science/article/pii/S2238785417303769>

- [111] M. Swartling, B. Sundelin, A. Tilliander, and P. G. Jönsson, “Heat transfer modelling of a blast furnace hearth,” *Steel research international*, vol. 81, no. 3, pp. 186–196, 2010. [Online]. Available: <https://onlinelibrary.wiley.com/doi/abs/10.1002/srin.200900145>
- [112] “Graftech international,” <http://archive.constantcontact.com/fs072/1101483160833/archive/1102208996928.html>, webpage.
- [113] A. Bhattacharya, A. Debjani, and S. Debjani, “Estimation of operating blast furnace reactor invisible interior surface using differential evolution,” *Applied Soft Computing*, vol. 13, no. 5, pp. 2767 – 2789, 2013. [Online]. Available: <http://www.sciencedirect.com/science/article/pii/S1568494612004619>
- [114] D. Gruber, K. Andreev, and H. Harmuth, “Fem simulation of the thermomechanical behaviour of the refractory lining of a blast furnace,” *Journal of Materials Processing Technology*, vol. 155-156, pp. 1539 – 1543, 2004, proceedings of the International Conference on Advances in Materials and Processing Technologies: Part 2. [Online]. Available: <http://www.sciencedirect.com/science/article/pii/S0924013604006715>
- [115] J. Brulin, F. Roulet, A. Rekik, E. Blond, A. Gasser, R. Mc Nally, and M. Micollier, “Latest Evolution in Blast Furnace Hearth thermo-Mechanical Stress Modelling,” in *4th International Conference on Modelling and Simulation of Metallurgical Processes in Steelmaking*, Dusseldorf, France, Jun. 2011, p. CD rom. [Online]. Available: <https://hal.archives-ouvertes.fr/hal-00611744>
- [116] Y. Kaymak, “A simplified approach to the contact in thermo-mechanical analysis of refractory linings,” *Sohnstr*, vol. 65, p. 40237, 2007.
- [117] Electricité de France, “Finite element Code_Aster, Analysis of Structures and Thermomechanics for Studies and Research,” 1989–2017.
- [118] J. S. Hesthaven, G. Rozza, and B. Stamm, *Certified Reduced Basis Methods for Parametrized Partial Differential Equations*, 1st ed., ser. Springer Briefs in Mathematics. Switzerland: Springer, 2015.
- [119] W. H. A. Schilders and A. Lutowska, *A Novel Approach to Model Order Reduction for Coupled Multiphysics Problems*. Cham: Springer International Publishing, 2014, pp. 1–49. [Online]. Available: https://doi.org/10.1007/978-3-319-02090-7_1
- [120] R. W. Freund, *The SPRIM Algorithm for Structure-Preserving Order Reduction of General RCL Circuits*. Dordrecht: Springer Netherlands, 2011, pp. 25–52. [Online]. Available: https://doi.org/10.1007/978-94-007-0089-5_2
- [121] A. Odabasioglu, M. Celik, and L. T. Pileggi, “Prima: passive reduced-order interconnect macromodeling algorithm,” *IEEE Transactions on Computer-Aided Design of Integrated Circuits and Systems*, vol. 17, no. 8, pp. 645–654, Aug 1998.
- [122] W. Schilders, *Introduction to Model Order Reduction*. Berlin, Heidelberg: Springer Berlin Heidelberg, 2008, pp. 3–32. [Online]. Available: https://doi.org/10.1007/978-3-540-78841-6_1
- [123] R. M. Duarte, I. Ruiz-Bustinza, D. Carrascal, L. F. Verdeja, J. Mochón, and A. Cores, “Monitoring and control of hearth refractory wear to improve blast furnace operation,” *Ironmaking & Steelmaking*, vol. 40, no. 5, pp. 350–359, 2013. [Online]. Available: <https://doi.org/10.1179/1743281212Y.0000000045>
- [124] S. Boisgérault and J.-P. Zolésio, “Shape derivative of sharp functionals governed by navier-stokes flow,” *Partial differential equations (Praha, 1998)*, vol. 406, pp. 49–63, 1999.
- [125] A. Laurain and K. Sturm, “Distributed shape derivative via averaged adjoint method and applications,” *ESAIM: Mathematical Modelling and Numerical Analysis*, vol. 50, no. 4, pp. 1241–1267, 2016.
- [126] M. Fischer, F. Lindemann, M. Ulbrich, and S. Ulbrich, “Fréchet differentiability of unsteady incompressible navier–stokes flow with respect to domain variations of low regularity by using a general analytical framework,” *SIAM Journal on Control and Optimization*, vol. 55, no. 5, pp. 3226–3257, 2017.



The ROMSOC project

September 28, 2018

ROMSOC-D5.1-0.1

Horizon 2020